The Synergistic Effects between Radiation Chemistry and Carbon Steel Corrosion in the Calandria Vault and End Shield Cooling System of a CANDU® Reactor

by

Jordan Lyons

Bachelor of Science in Chemical Engineering

University of New Brunswick

2015

A Thesis Submitted in Partial Fulfillment
of the Requirements for the Degree of

Master of Science in Engineering

in the Graduate Academic Unit of Chemical Engineering

Supervisors: W.G. Cook, PhD, P.Eng, Chemical Engineering

C.R. Stuart, PhD, MRSC, Senior Scientist, CNL

Examining Board: M.F. Couturier, Ph.D., P.Eng., Chemical Engineering

L.P.F. Chibante, Ph.D., Chemical Engineering

C.A. Dyker, Ph.D., Chemistry, External Examiner

This thesis is accepted by the

Dean of Graduate Studies

THE UNIVERSITY OF NEW BRUNSWICK

September, 2017

©Jordan Lyons, 2017

ABSTRACT

Water radiolysis (radiation induced breakdown of water into hydrogen, oxygen and hydrogen peroxide) can lead to operational and safety issues in the water filled systems of a CANDU® reactor. The calandria vault and end shield cooling system is one such location where significant water radiolysis occurs. The purpose of this system is to act as a biological shield to protect against the high levels of radiation produced in the reactor core. The calandria vault surrounds the body of the reactor, while two end shields, filled with carbon steel balls, cover each reactor face. The vault is filled with light water that is continuously circulated through each end shield to act as a coolant for the carbon steel balls within. A nitrogen cover gas is circulated above the water level in the vault to allow for expansion during reactor start-up. When net water radiolysis occurs in this system, the hydrogen and oxygen produced can readily diffuse into the cover gas and, if not properly managed, may reach flammability limits.

The calandria vault and end shield cooling system at the Point Lepreau Nuclear Generating Station had few issues with hydrogen production and migration into its cover gas until 1989 when purging of the cover gas began to be frequently required to keep the hydrogen concentration below the lower flammability limits. The root cause of the sudden excess production of hydrogen was traced to oxygenated make-up water, needed since plant start up in 1983 due to a small leak in the calandria vault. The use of hydrazine as an oxygen scavenger has been demonstrated to mitigate the problem by removing dissolved oxygen and returning the system to a net radiolytically suppressed state. Speculation on why it took

seven years to reach net radiolysis conditions was focused on hydrogen production and oxidant consumption from the corrosion of the carbon steel end shield balls. Keeping excess hydrogen in an irradiated system is known to suppress net water radiolysis and limit production of hydrogen, oxygen and hydrogen peroxide.

This study was implemented to better understand the synergies and interactions between carbon steel corrosion and water radiolysis. A test loop was built to simulate the conditions in the end shield cooling system, which contained a packed column of carbon steel ball bearings that was exposed to a gamma-radiation field in a Gammacell at the Chalk River Laboratories. Results demonstrated that oxygen consumption from corrosion processes can indeed place the system into net radiolytic suppression, subsequently, corrosion-generated hydrogen assists in maintaining this state. These corrosion processes minimize the production of radiolytically-generated hydrogen, oxygen and hydrogen peroxide. However, as the carbon steel passivates, the corrosion rate will slow, thereby diminishing the hydrogen production and oxygen consumption rates, after which net radiolysis can be re-established verifying the initial hypothesis. The study also explored methanol as an alternative oxygen scavenger to hydrazine and demonstrated that it could be effective in minimizing hydrogen production, but may increase carbonate loadings on ion-exchange resins in the system's purification system.

DEDICATION

I dedicate this thesis to my mother, Darlene Lyons. Without her love and support throughout my education I would have never been able to succeed to the lengths that I have.

ACKNOWLEDGEMENTS

I would like to extend a special thanks to both my supervisors and friends, Dr. William Cook and Dr. Craig Stuart. Their continual support and guidance throughout this project was paramount in my successful completion. An extra special thank-you is extended to Craig and his family for housing me during my term at Canadian Nuclear Laboratories.

Canadian Nuclear Laboratories and staff are thanked for their contributions to this work, and for access to their facilities to conduct my research. The experience I received during my time there was invaluable. I am also very grateful for all the guidance I received from my mentor and friend Randy Perron; his contributions were an asset to this project's success.

I am grateful for the contributions from NB Power, in particular from my friend, Eric Gardner. His continual involvement and correspondence were a large contributor to the overall success of this project.

I must also thank all of the technical staff at the University of New Brunswick, in particular Adon Briggs, Carl Murdock, and Keith Rollins, for all of their contributions to this project. Chester Morris is especially thanked for all his contributions to the design and construction of the flow system.

Support from my mother and father was always appreciated, particularly during the heavy work load of my undergrad, I wouldn't have made it this far without them. My mother and father in-law's support over the last few years is greatly appreciated, without it I wouldn't

have been able to complete this degree. Finally, to my wife Alissa, thank you for all of your love, continual support, and understanding, I couldn't have succeeded without you.

Table of Contents

ABSTRACT ii

DEDICATION iv

ACKNOWLEDGEMENTS v

Table of Contents vii

List of Tables xi

List of Figures xiii

List of Symbols, Nomenclature and Abbreviations xvii

1. Introduction 1

1.1 Overview of CANDU® Reactors 1

1.2 Calandria Vault and End Shield Cooling System 3

1.3 Hydrogen Generation in the ESC System at PLNGS 4

1.4 Operating Experience at PLNGS 5

1.5 Objectives of Study 7

2. Literature Review 9

2.1 Fundamentals of Radiation Chemistry 9

2.2 Carbon Steel Corrosion 15

2.3 The Calandria Vault and End Shield Cooling System 20

2.3.1 Hydrazine Additions 23

2.3.2 Methanol as an Oxygen Scavenger 25

3. Experimental Test Methods and System Design 27
3.1 Loop Overview 27
3.2 Loop Flow Configurations 28
3.3 Loop Components and Design 29
3.3.1 Loop Flow Components 29
3.3.2 Feed Tanks 30
3.3.3 Sparge Vessel 31
3.3.4 Temperature Control 33
3.3.5 Test Section 33
3.3.6 Orbisphere Analyzers – Dissolved Gas Measurement 36
3.4 Conductivity and pH Measurements 37
3.5 Preparation of Solutions 38
3.6 SEM and EDS 39
3.6.1 Scanning Electron Microscopes 39
3.6.2 Energy Dispersive X-ray Spectroscopy 41
3.7 Hydrogen Peroxide Assay 42
3.8 Pre-aging Carbon Steel Balls 45
3.9 Loop Commissioning 45
4. Results 47

4.1 Corrosion Experiments 47

4.1.1 Once-Through Corrosion-Only Tests 47

4.1.2 Recirculating Corrosion-Only Tests 48

4.2 Radiation Chemistry Tests 50

4.3 Radiation Chemistry and Corrosion Tests 51

4.3.1 Corrosion of Fresh Carbon Steel under Irradiated Conditions 51

4.3.2 Loop Contamination and Acid Washing 54

4.3.3 In-situ Aging Effects on Carbon Steel Corrosion under Irradiated Conditions 56

4.3.4 Corrosion of Autoclave Aged Carbon Steel 61

4.4 Oxygen Scavenging by Chemical Addition 64

4.4.1 Oxygen Scavenging by Hydrazine Injection 64

4.4.2 Oxygen Scavenging by Methanol Injection 67

5. Discussion 70

5.1 Kinetic Model of Radiation Chemistry and Corrosion 70

5.2 Relevance of Results to ESC System at PLNGS 74

5.2.1 Suppression of Net Radiolysis by Corrosion Processes in the ESC System . 74

5.2.2 Oxygen Scavenging in the ESC System at PLNGS 75

6. Conclusions and Recommendations 80

6.1 Conclusions 80

6.2 Recommendations for Future Work 81

7. References 83

Appendix A: Engineering Drawings 89

Appendix B: Sparge Vessel Air Ingress Model 94

Appendix C: Corrosion and Penetration Rates Sample Calculations 106

Appendix D: Methanol Equilibrium Model 108

Appendix E: Radiation Chemistry Model 121

Curriculum Vitae

List of Tables

Table 2-1: g-values for Water at Near Neutral pH at 25 ºC for Low LET Radiation [8] . 11

Table 3-1: Carbon Steel Test Section Balls' Composition 27

Table 4-1: Surface Composition Results from EDS Analysis 59

Table 4-2: EDS Analysis Results of Fresh Carbon Steel Balls 61

Table 4-3: Oxygen Consumption Rate Comparison between Fresh and Aged Balls 62

Table 4-4: Surface Composition Results from EDS Analysis 63

Table 4-5: Oxygen and Hydrogen Consumption from Hydrazine Injections 66

Table 4-6: Oxygen Consumption from Methanol Injections 69

Table 5-1: Rate Constants at High and Low Oxygen Concentrations 72

Table B-1: Values Used for Constants in Model……..…..102

Table D-1: Reactions and Corresponding Equilibrium Constants 108

Table D-2: Gibbs Free Energies of Formation 109

Table D-3: Equilibrium Constants and Gibbs Energies of Reaction 110

Table D-4: Ionic Molar Conductivities at Infinite Dilution [10] 112

Table E-1: g-Values for Water at Room Temperature for Low LET Radiation [33] 121

Table E-2: Radiation Chemistry Reactions Considered in Model 122

Table E-3: Equilibrium Reactions Incorporated into Radiolysis Model [8] 124

List of Figures

Figure 1-1: Typical Flow Schematic of a CANDU® Reactor [15] 2

Figure 1-2: Cut-away Schematic of Reactor Vault and End Shield Cooling System..... 4

Figure 2-1: Timescale from Ionization Event to Homogenous Reaction Kinetics [7] 9

Figure 2-2: Illustration of Chemical Events Produced from Low and High LET [6]..... 10

Figure 2-3: Animation of Processes Occurring at an Electro-chemical Interface 16

Figure 2-4: Pourbaix Diagram for Iron at 25°C and 10^{-3}M [16]..... 18

Figure 2-5: Equilibrium Potentials for Various Iron Oxidization Processes [26] 19

Figure 2-6: Simplified End Shield Cooling System PFD [1] 21

Figure 3-1: Simplified Process Flow Diagram of Test Loop..... 28

Figure 3-2: Sparge Vessel Design and Flow Configuration 32

Figure 3-3: Test Section Design and Flow Configuration 35

Figure 3-4: Orbisphere Electro-chemical Sensor Face 36

Figure 3-5: Characteristic X-ray Formation [23]..... 41

Figure 3-6: Hydrogen Peroxide Assay Calibration Curve..... 44

Figure 4-1: Once-through Corrosion-Only Test 47

Figure 4-2: Recirculating Corrosion-Only Experimental Results 49

Figure 4-3: Net Radiolysis Experimental Results..... 51

Figure 4-4: Synergistic Effects between the Radiation Chemistry of Water and Corrosion of Fresh Carbon Steel..... 52

Figure 4-5: Synergistic Effects between the Radiation Chemistry of Water and Corrosion of Fresh Carbon Steel with Hydrogen Evolution..... 53

Figure 4-6: Loop Contamination and Subsequent Acid Washes 55

Figure 4-7: Slowing Oxygen Consumption Rates Following H_2O_2 Injections 56

Figure 4-8: Varying Oxygen Consumption Rates Through Continual Oxidant Addition 57

Figure 4-9: Steady State Net Radiolysis Following Several Hydrogen Peroxide Additions 58

Figure 4-10: SEM Images of CS Balls Used in Irradiated Loop Experiments 59

Figure 4-11: SEM Secondary Electron Image of Fresh Carbon Steel Ball 60

Figure 4-12: Comparison of Fresh and Aged Balls 62

Figure 4-13: SEM Images of CS Balls Aged under De-aerated (a) and Aerated (b) Conditions 63

Figure 4-14: Irradiated Oxygen Scavenging by Hydrazine 65

Figure 4-15: Irradiated Oxygen Scavenging by Methanol 67

Figure 5-1: Net Radiolysis Experimental Results (PLOT (A)) vs. Model Simulation (PLOT (B))..... 70

Figure 5-2: Comparison of Modelled and Experimental Corrosion Effects..... 72

Figure 5-3: Radiation Chemistry and Corrosion Experimental Data (PLOT (A)) vs. Modelled Data (PLOT (B))..... 73

Figure 5-4: Comparison of Hydrazine and Methanol Oxygen Scavenging..... 76

Figure 5-5: Model Results Presenting Effects of MeOH Injections on System pH and Conductivity Following IX Break on Carbonates 78

Figure A-1: Loop Process Flow Diagram……..……90

Figure A-2: Test Section Design Drawing..... 91

Figure A-3: Mesh Support Basket for Autoclave Aging 92

Figure A-4: Autoclave Configuration in CS Aging..... 93

Figure B-1: Results of Corrosion Test # 1 94

Figure B-2: Oxygen Consumption Rate with Sparge Vessel Valved-out..... 96

Figure B-3: Increasing Oxygen Concentration due to Air Ingress 97

Figure B-4: Comparison of Experimental and Modelled Oxygen Ingress Behavior..... 102

Figure E-1: Applying the Integral Method to Experimental Data 126

Figure E-2: Comparison of Modelled and Experimental Corrosion Data 127

Figure E-3: Comparison of Modelled and Experimental Corrosion Data 128

List of Symbols, Nomenclature and Abbreviations

List of Abbreviations

AISI – American Iron and Steel Institute

BSP – British Standard Pipe

CANDU® – CANada Deuterium Uranium - Trademark of Atomic Energy of Canada Ltd.

CHC – Critical Hydrogen Concentration

CS – Carbon Steel

CSC – Carbon Steel Corrosion

DI Water – De-Ionized Water

EDS – Energy Dispersive x-ray Spectroscopy

ESC – End Shield Cooling

IX – Ion exchange

LET – Linear Energy Transfer

NPT – Nominal Pipe Thread

ppb – Parts Per Billion (μg/kg)

PFD – Process Flow Diagram

PID – Proportional Integral Derivative

ppm – Parts Per Million (mg/kg)

PLNGS – Point Lepreau Nuclear Generating Station

SATP – Standard Ambient Temperature and Pressure ($25^{o}C$ & 1 atm)

SCE – Saturated Calomel Electrode

SEM – Scanning Electron Microscope

UV-Vis – Ultra Violet Visible

List of Symbols

A – Absorbance

a – Order of reaction

b – Path length of light through medium

CR – Corrosion rate

D – Diameter

$D_{A/B}$ – Diffusivity of species "A" through "B"

g(X) – g-value of species “X”

G(X) – Net yield of species “X”

H – Height

H_A – Henry’s law constant for species “A”

K_L – Overall liquid mass transfer coefficient

K_{eq} – Equilibrium constant

k – Reaction rate constant

k’ – The product of “b” and “ε”

k_l – Liquid film mass transfer coefficient

m – mass

n – A quantity defining the ratio of radiolytically produced molecular species; dependent on temperature, energy deposition rate of the incident radiation and other chemistry conditions (e.g. pH) ($0<n<1$)

N_A – Molar flux of species “A”

PR – Penetration rate

R – Ideal gas constant (8.314 J/mol.k)

SA – Surface area

T – Temperature

t – time

V – Volume

ε – Molar Extinction Coefficient

ΔG_f^o – Gibbs free energy of formation at standard state conditions

ΔG_{rxn}^o – Gibbs free energy of reaction at standard state conditions

δ – Film thickness

Λ^∞ – Solution specific conductivity at infinite dilution

λ^∞ – Ionic molar conductivity at infinite dilution

ν_i – Stoichiometric reaction coefficient of species "i"

π – Pi (3.1452)

ρ – Density

$[X]$ – Concentration of species "X"

$[\dot{X}]$ – Concentration flow rate of species "X"

1. Introduction

1.1 Overview of CANDU® Reactors

Like thermal plants, CANDU® reactors boil water to produce steam, which is then fed to turbines. Energy from the steam drives the blades to produce electricity from the generator connected to the turbines. The underlying difference between nuclear and thermal plants is the mechanism of heat generation. Thermal plants burn wood, coal, gas or oil to generate heat, whereas the heat generated in a nuclear plant is provided by the fissioning of heavy fissile elements.

In CANDU® reactors, pressurized cooling water (heavy water) is transported through the reactor core to remove heat generated from the fission reactions. The heated heavy water is then sent to steam generators, which are essentially large U-tube type heat exchangers. Heat is transferred from the heavy water in the tube side to light water on the shell side of the steam generator. This causes the light water to boil, hence generating the steam required to drive the turbine. A typical flow schematic of a CANDU® reactor is displayed in Figure 1-1. The figure displays two distinct flow systems separated by the steam generators. The system carrying heavy water through the reactor and supplying heat to the steam generators is the primary heat transport system, while the system carrying light water from the steam generators to the turbines is known as the secondary heat transport system.

The system surrounding the fuel channels through which the primary heat transport system passes, is known as the moderator system, which is mostly contained in a horizontal,

cylindrical vessel known as the calandria. In order to induce fissioning of heavy fissile elements, a moderator is required to thermalize ("slow-down") neutrons. CANDU® reactors use natural uranium as a fuel source, and therefore require heavy water as a moderator. Natural uranium has a lower composition of fissile isotopes (0.7% U-235), as opposed to the enriched fuel required for light water reactors (3-4% U-235). Heavy water provides more efficient moderation than light water, and hence does not require the fuel to be enriched. The calandria is filled with heavy water that is continuously circulated through an external heat exchanger to remove excess heat, as shown in Figure 1-1.

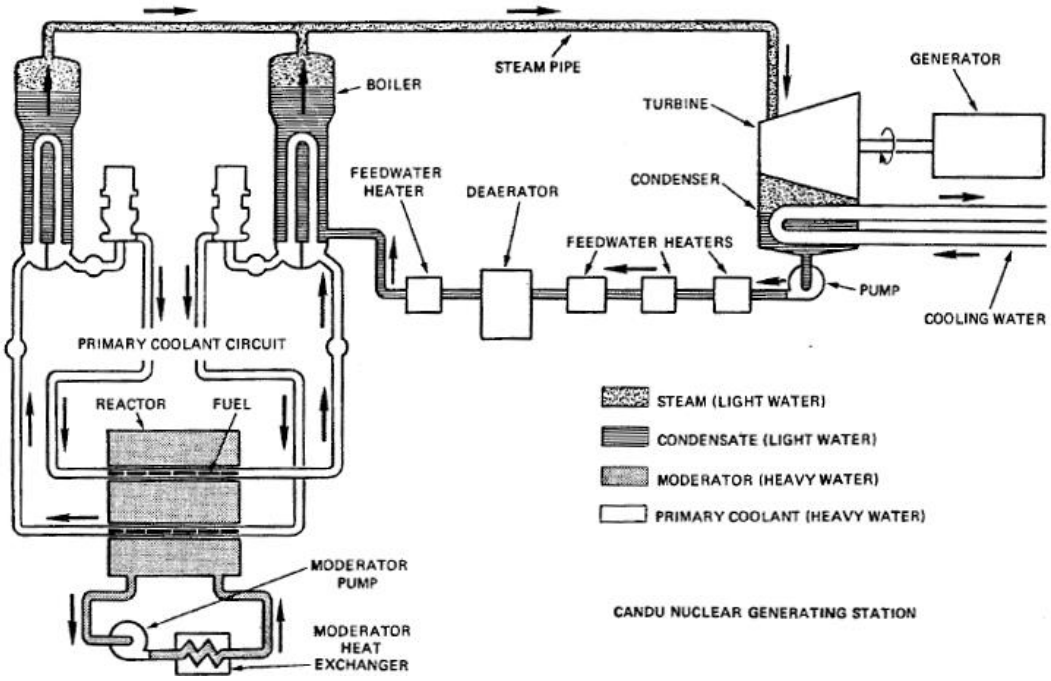


Figure 1-1: Typical Flow Schematic of a CANDU® Reactor [15]

Large quantities of ionizing radiation are produced as a result of the fission reactions occurring in the reactor core, therefore, shielding around the reactor is required. The

calandria is enclosed by the calandria vault and end shield cooling system, which acts to shield the surrounding environment from the high levels of ionizing radiation present in the reactor core.

1.2 Calandria Vault and End Shield Cooling System

The calandria vault and end-shield cooling (ESC) system consists of two end shields, through which the fuel channels pass, and a vault surrounding the calandria body. The vault is constructed of concrete, which is lined with carbon steel, and filled with light water. The body of the calandria is enclosed by the water-filled vault, while each face of the reactor is shielded by two end shields, which are filled with carbon steel ball bearings, approximately 3/8" to ½" in diameter. A cut-away schematic of the reactor system is displayed in Figure 1-2, with each component numbered and listed.

The ESC system contains approximately 567 m^3 of light water that is maintained at slightly alkaline pH (9.0-10.0 adjusted w/ LiOH) to minimize corrosion of its carbon steel components. Water is continuously circulated from the vault and through the end shields to act as a coolant for the carbon steel balls within. The primary purpose of this system is to shield the surrounding environment from the high levels of ionizing radiation produced in the reactor core. In order to allow for expansion upon reactor start-up there is also a nitrogen cover gas above the water level in the vault that operates slightly above atmospheric pressure.

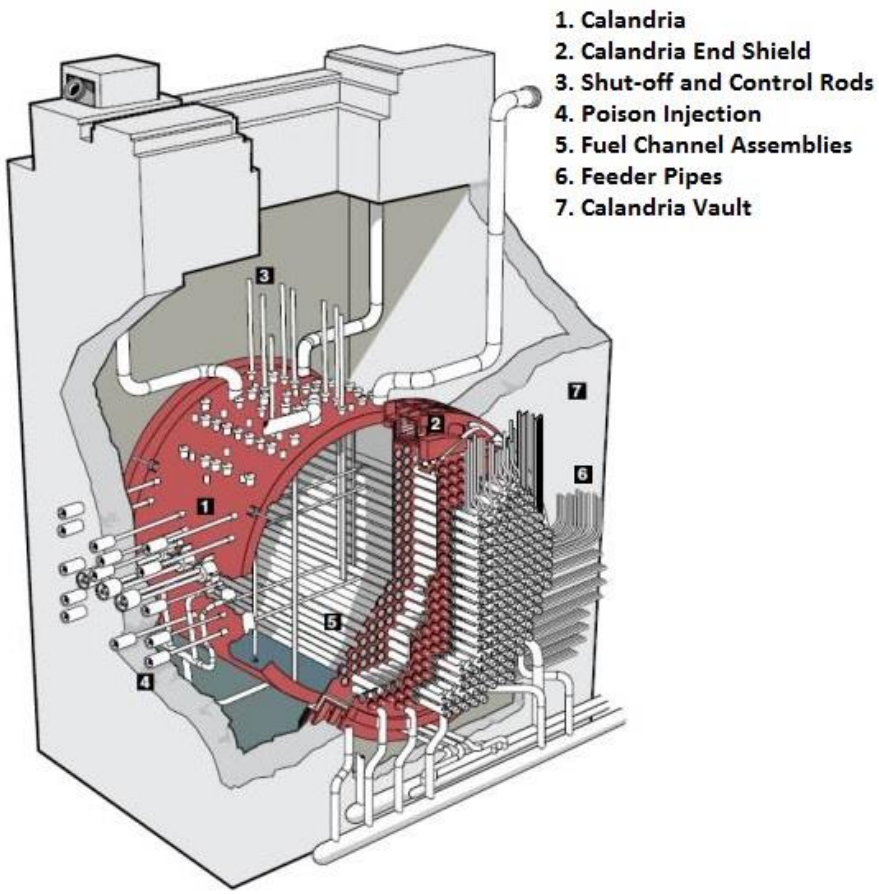


Figure 1-2: Cut-away Schematic of Reactor Vault and End Shield Cooling System

1.3 Hydrogen Generation in the ESC System at PLNGS

Point Lepreau Nuclear Generating Station (PLNGS) began operations in 1983 and has since initial commissioning required makeup water for the plant's end shield cooling (ESC) system. The makeup water fed to the system is air saturated (≈ 8 ppm O_2) and comes from the facilities' water treatment plant. In 1989 elevated hydrogen concentrations were detected in the calandria vault cover gas system. These elevated levels of hydrogen were ultimately attributed to the net radiolytic breakdown of water [1]. When water is in the

presence of ionizing radiation it will break down to form several highly reactive species which can, under certain conditions, result in the formation of significant quantities of hydrogen, oxygen, and hydrogen peroxide [3]. Because the system operates just slightly above atmospheric pressure, the radiolytically produced gases (H_2 & O_2) readily diffuse into the vault cover gas. If this process is not controlled in some manner, flammable concentrations of these gases will build up; regular purging of the cover gas system is required to maintain low hydrogen concentrations.

1.4 Operating Experience at PLNGS

As mentioned previously, hydrogen production in the ESC system was not an issue between 1983 and 1989. It is postulated that corrosion processes occurring on the carbon steel surfaces in the system were responsible for the mitigation of hydrogen production during that time frame.

If an irradiated water system is under a condition described as net radiolysis, there will be a presence of significant quantities of hydrogen, oxygen and hydrogen peroxide dissolved in the water. The concentrations of these radiolytically produced molecular species (H_2, O_2 and H_2O_2) are inter-dependent on one another due to the reaction mechanisms associated with radiation chemistry. If oxygen or hydrogen peroxide is removed from the system, or hydrogen is added, the concentrations of all three species will decrease [4]. If there is a sufficient hydrogen addition or oxidant (O_2 or H_2O_2) removal, the system can enter a state described as net radiolytic suppression, whereby the concentrations of radiolytically

produced oxidants (O_2 and H_2O_2) are negligible, and hydrogen concentrations can be quite low.

Since carbon steel corrosion is known to consume oxygen and/or produce hydrogen, it has been postulated that corrosion maintained net radiolytic suppression during the first six years of operation at PLNGS by keeping dissolved oxygen concentrations low and potentially adding a slight excess of dissolved hydrogen to help maintain net radiolytic suppression. It has been speculated that the shift to net radiolysis in 1989 was due to passivation of system's carbon steel components, thereby reducing their ability to produce hydrogen and/or remove oxidants. Following the system's shift to net radiolysis in 1989, elevated concentrations of hydrogen were managed by frequent purging of the cover gas, however, this method was labor intensive and time consuming. Hydrogen addition as a means of consuming oxidants in a radiation environment is employed in many other systems to maintain net radiolytic suppression; however, in the ESC system this is not a feasible option as any gases added to this low pressure system will readily diffuse into the cover gas and exacerbate the problem.

The plant currently maintains low hydrogen and oxygen concentrations by periodically injecting hydrazine to scavenge oxygen [2]. Hydrazine is widely used in steam cycles of thermal power plants as an oxygen scavenger to maintain reducing conditions [3]. There, it relies on the high temperature conditions of the system to react with oxygen, however, in the low temperature environment of the end shield cooling system the mechanism relies on radiation chemistry. Experience at PLNGS has shown that hydrazine additions remove

oxygen with an approximate stoichiometric ratio of 1:1, which readily places the system into net radiolytic suppression [2].

1.5 Objectives of Study

The objectives of this study were twofold; firstly to develop an understanding of the synergies between water radiolysis and carbon steel corrosion. Understanding the synergies between radiation chemistry and corrosion gives insight into the mechanisms that kept the system in net suppression from 1983 to 1989.

The second objective was to investigate a potential replacement for hydrazine as an oxygen scavenger in the ESC system. Although hydrazine is very effective in removing oxygen and limiting hydrogen production, strict handling restrictions have encouraged exploration into alternatives. Therefore, preliminary research into the use of methanol as a prospective replacement was performed.

The effects of carbon steel corrosion and radiation chemistry were studied separately and together in a low temperature, low pressure flow loop. Loop experiments were carried out at conditions approximating those in the ESC system. Water was circulated through an irradiated test section composed of a 1 liter PYREX® vessel for development of the radiation chemistry, and a packed bed of AISI 1010 carbon steel balls was used to simulate corrosion of end shield balls. The grade of carbon steel chosen falls within specification for the end shield cooling system in CANDU® 6 plants, which specifies any carbon steel

between AISI 1008 and 1026, excluding 1024, with a maximum cobalt and manganese content of 0.07%, and 1.0%, respectively.

Results from all tests were input into a corrosion and radiation chemistry model in an attempt to recreate conditions observed in the experiments, this is summarized in Section 5.1 and Appendix E. In addition, an equilibrium model was developed to predict the effects of carbon dioxide on system chemistry, which is produced by the oxygen scavenging mechanism of methanol [5]; this is outlined and discussed in Section 5.2.2 and Appendix D.

2. Literature Review

2.1 Fundamentals of Radiation Chemistry

The radiolytic breakdown of water (radiolysis) is initiated by the ionization or excitation of a water molecule by ionizing radiation (e.g. gamma, fast electrons, etc.) [3]. This is the physical stage of radiolysis whereby excited, unstable water molecules ($^{*}H_2O$) or ion pairs ($H_2O^{+}+e^{-}$) are formed. The ejected electron from the ion pair may contain sufficient energy to initiate further localized ionization events until it becomes thermalized. The excited and ionized water molecules will go on to form several radical and molecular species over a very short time scale [6]. A schematic of the progression of these reactions as a function of time following the initial ionization/excitation event is displayed in Figure 2-1.

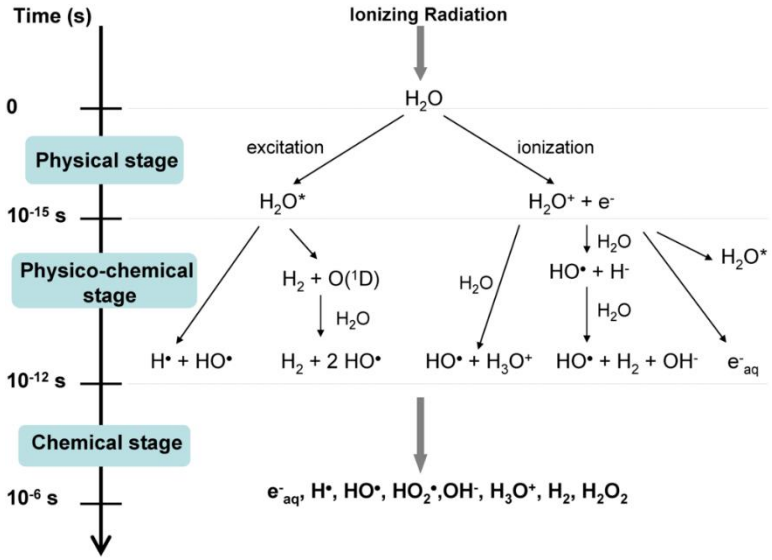


Figure 2-1: Timescale from Ionization Event to Homogenous Reaction Kinetics [7]

The nature of the ionization event distribution is dependent upon the Linear Energy Transfer (LET) of the incident radiation. In low LET radiation (e.g. fast electrons, gamma rays) energy deposition occurs in well separated points along the path of travel, which produces small groups of ionized species called spurs, as shown in Figure 2-2. High LET radiation (e.g. neutrons) will produce frequent ionization events resulting in coalescence of the spurs, which forms a continuous path of ionization events. Figure 2-2 illustrates the different energy deposition behaviors of high and low LET radiation. [6]

In either case, over the very short time scale displayed in Figure 2-1, the reaction kinetics are non-homogenous. Species formed through interactions with low LET radiation will have a limiting escape yield away from the spur as the system trends towards homogenous reaction kinetics.

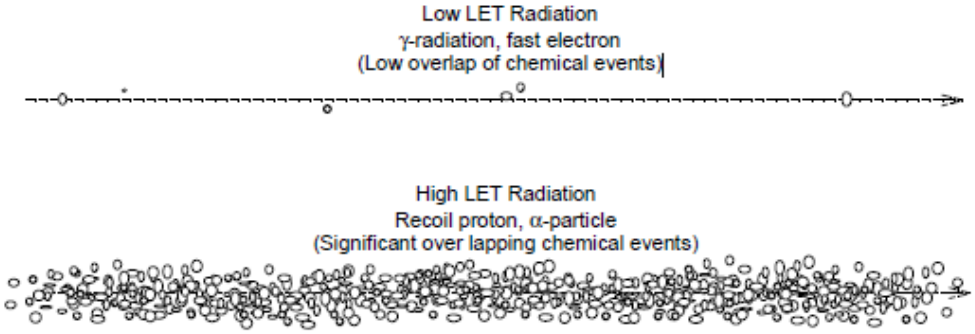


Figure 2-2: Illustration of Chemical Events Produced from Low and High LET [6]

The escape yield is based on the competition between diffusion of the species' away from the spur and their reaction within the spur. The species' that escape the spurs and contribute

to the bulk reaction kinetics of a system are called “primary products”. The escape yields of these “primary products” are expressed as g-values, shown in Table 2-1, which are given in units of species/100eV [8].

Table 2-1: g-values for Water at Near Neutral pH at 25 ºC for Low LET Radiation [8]

Primary Species	**$e_{(aq)}^-$**	**·H**	**·OH**	**H_2**	**H_2O_2**	**$HO_2\cdot/O_2\cdot^-$**	**H^+**
G-value (species/100eV)	2.63	0.55	2.72	0.45	0.68	0.008	2.63

The g-values for high LET radiation are also documented, and the primary species formed are the same, but generally speaking the yield of molecular species are higher and radical species are lower for high LET radiation. This is due to the overlapping nature of the high LET ionization events. Since the spurs are in such close proximity, the unstable radical species being formed have a higher chance of reacting to form stable molecular species prior to reaching homogenous distribution. In either case, the species that participate in bulk system reaction kinetics are shown by equation (2-1). Homogenous distribution of these species occurs about 100 ns after the ionization/excitation event [6]. This study has only considered the effects of low LET radiation. Though high LET radiation is present in the ESC system, the dose rates of low LET radiation are several orders of magnitude greater in the vast majority of the system [9].

$$H_2O + \gamma \rightarrow e_{(aq)}^-, H^+, HO_2, H_2, H_2O_2, \cdot H, \cdot OH \quad (2\text{-}1)$$

The species produced in reaction (2-1) can react through a series of elementary reactions that will result in the net formation of significant quantities of hydrogen, oxygen and hydrogen peroxide.

Some of the primary radiolysis products will react to re-form water, and create further hydrogen peroxide and hydrogen. These primary reactions are carried out as displayed in equations (2-2) – (2-4) [10].

$$\cdot H + \cdot OH \rightarrow H_2O \tag{2-2}$$

$$\cdot H + \cdot H \rightarrow H_2 \tag{2-3}$$

$$\cdot OH + \cdot OH \rightarrow H_2O_2 \tag{2-4}$$

Once enough hydrogen peroxide is formed, it will readily react with some of the radical species to form oxygen through a series of secondary reactions, as displayed in equations (2-5) – (2-7) [10].

$$\cdot OH + H_2O_2 \rightarrow \cdot HO_2 + H_2O \tag{2-5}$$

$$\cdot OH + \cdot HO_2 \rightarrow O_2 + H_2O \tag{2-6}$$

$$\cdot HO_2 + \cdot HO_2 \rightarrow O_2 + H_2O_2 \tag{2-7}$$

It should be noted that there are numerous reactions occurring simultaneously under irradiated conditions. The primary and secondary reaction sets shown above are the basic progressions that make-up the net production of hydrogen, oxygen and hydrogen peroxide,

for a full list of reactions see Tables E-2 and E-3 in the appendix. Reaction (2-8) describes the production of hydrogen, oxygen and hydrogen peroxide from the net radiolytic break down of water, assuming there is no initial oxidant present in the system. The term "n" holds a value between 0 and 1, and is dependent on system conditions such as temperature, energy deposition rate of the incident radiation, and chemistry (e.g. pH) [9].

$$H_2O \xrightarrow{Ionizing\ Radiation} \frac{1}{2}(1+n)\,H_2 + \frac{1}{2}nO_2 + \frac{1}{2}(1-n)H_2O_2 \qquad (2\text{-}8)$$

If these secondary reactions are not suppressed in some manner there is no method by which the concentration of hydrogen is managed. Thus, as these reactions proceed the hydrogen concentration will continue to rise, as will oxygen and hydrogen peroxide, until a steady state condition is achieved [4].

The net formation of hydrogen, oxygen, and hydrogen peroxide can be suppressed if a small excess of hydrogen is present within the system, as shown by reactions (2-9) - (2-11) [10].

$$\cdot OH + H_2 \rightarrow \cdot H + H_2O \qquad (2\text{-}9)$$

$$\cdot H + O_2 \rightarrow \cdot HO_2 \qquad (2\text{-}10)$$

$$\cdot H + H_2O_2 \rightarrow \cdot OH + H_2O \qquad (2\text{-}11)$$

The excess hydrogen in the system will react through reaction (2-9) and consume hydroxyl radicals (·OH) at a faster rate than reactions (2-5) and (2-6). This mechanism mitigates

oxygen generation, and allows hydrogen concentrations to remain at safe and manageable levels. Because reaction (2-5) is suppressed, this limits the amount of hydroperoxyl radicals ($\cdot HO_2$) produced, thereby suppressing reactions (2-6) and (2-7). Hydrogen atoms produced from reaction (2-9) can combine with hydrogen peroxide, as shown in equation (2-11). This generates further hydroxyl radicals which react with the excess hydrogen, keeping net suppression in a continual cycle. The overall result is displayed by equation (2-12). [10]

$$H_2O + H_{2,Excess} \rightsquigarrow H_2O + H_{2,Excess} \quad (2\text{-}12)$$

The fact that an excess of hydrogen can place the system into net radiolytic suppression suggests that there is a minimum hydrogen concentration that must be maintained in order to remain in such a state. This is known as the critical hydrogen concentration (CHC) and is slightly variable based on system conditions (e.g. impurity concentrations) [11]. The critical hydrogen concentration has been experimentally measured and is approximately 0.1 mL/kg and 0.5 mL/kg at neutral conditions and pH 10, respectively [4, 11].

There are many reactions associated with the radiolytic breakdown of water, those described here are the primary and basic progressions of the kinetics and chemistry. The mechanism described above by which a slight excess of hydrogen suppresses net radiolysis only applies if there is not an abundance of oxygen present in (or being introduced into) the system. For example, if oxygen is introduced into an irradiated water system in net radiolytic suppression, it will effectively promote recombination and consume the excess hydrogen, as displayed in equation (2-13) [4].

$$2H_2 + O_2 \xrightarrow{Ionizing\ Radiation} 2H_2O \quad (2\text{-}13)$$

If sufficient oxygen is added to lower the hydrogen concentration to the CHC, the system will revert to net radiolysis, and the concentrations of hydrogen, oxygen and hydrogen peroxide will all rapidly increase [4].

2.2 Carbon Steel Corrosion

When a metal is submerged in solution, it behaves as an electrode, whereby a potential difference is established between the metal surface and solution. As a result, anodic and cathodic sites form and there is a net flow of current from the anode to cathode. Oxygen reduction or proton reduction will occur at the cathodic sites, while iron oxidation will occur at the anodic sites, as shown in Figure 2-3. This mechanism is responsible for the aqueous corrosion of metallic materials. Metal corroding in solution is generally described as a mixed electrode because the cathodic and anodic reactions are simultaneously occurring on its surface [14]. The anodic and cathodic reaction rates must be equal as each process is required to drive the other (cathodic reactions are generally limiting) [15].

The current flow from the anode to cathode is called the corrosion current, which is effectively representative of the corrosion rate. This current is limited by the slowest step in the redox process. The limiting rate can be based on charge transfer at the metal surface or the rate of mass transfer of reactants to the metal surface from solution. When corrosion is limited by charge transfer it said to be controlled by activation polarization, whereas when limited by mass transfer it is said to be controlled by concentration polarization [15].

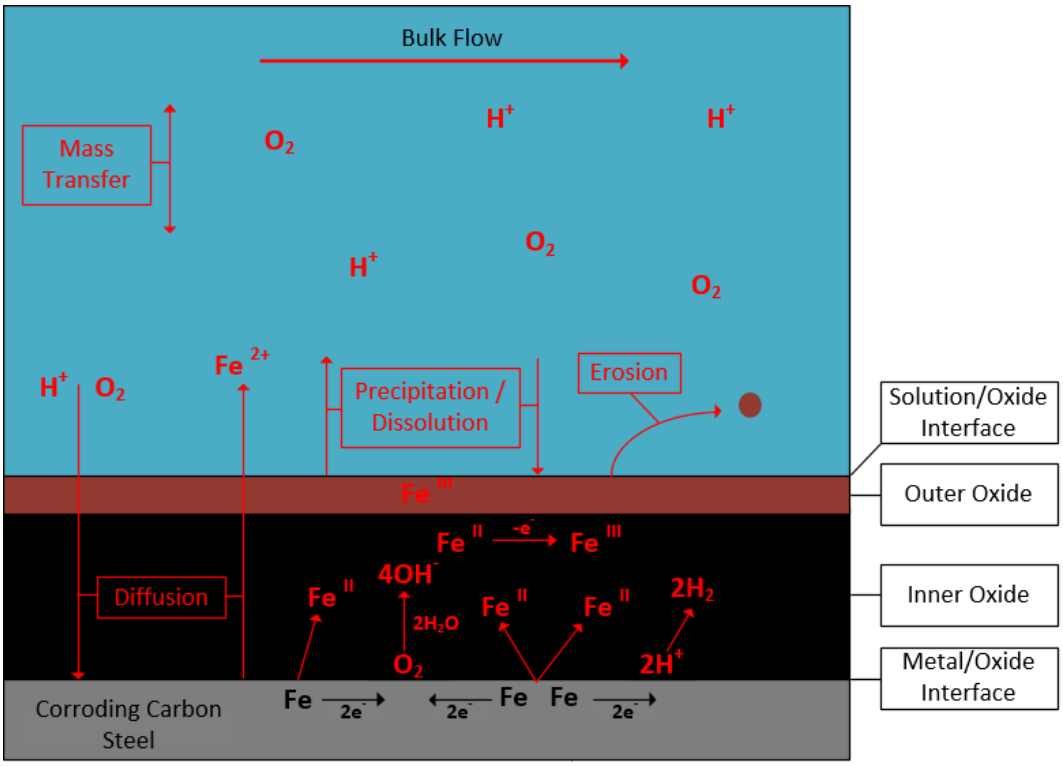


Figure 2-3: Animation of Processes Occurring at an Electro-chemical Interface

The redox processes occurring on freely corroding steel will generally consume oxygen and/or evolve hydrogen, as shown by the electro-chemical half reactions displayed in equations (2-14) - (2-16).

As corrosion proceeds, oxides will precipitate and form on the corroding steel surfaces. The oxidation state and type of oxides formed are dependent on the electro-chemical equilibrium potential and pH of the system; the rate at which they are formed is dependent upon the kinetics of the redox reactions.

Anodic Half Reaction:

$$Fe \rightarrow Fe^{2+} + 2e^{-} \quad (2\text{-}14)$$

Cathodic Half Reactions (Neutral or Alkaline Conditions):

$$\frac{1}{2}O_2 + H_2O + 2e^{-} \rightarrow 2OH^{-} \quad (2\text{-}15)$$

or

$$2H_2O + 2e^{-} \rightarrow H_2 + 2OH^{-} \quad (2\text{-}16)$$

Pourbaix Diagrams are generally used to gain insight as to what the passivity and nobility of a particular metal may be as a function of system pH and potential. They are effectively a thermodynamic map of the expected metal oxide states under a variety of pH and electro-chemical potential conditions. A Pourbaix Diagram for iron at 25^{o}C and 10^{-3}M is displayed in Figure 2-4 [16].

At slightly alkaline pH (9 – 10), the Pourbaix Diagram suggests that solid iron oxide states are formed at all values of potential. These iron oxides can promote passivation of the steel by acting as an insulator to current flow and/or limiting the rate of mass transfer of reactants to the metal surface, thereby slowing the corrosion rate. Therefore, the rates of oxygen consumption and/or hydrogen evolution will also slow.

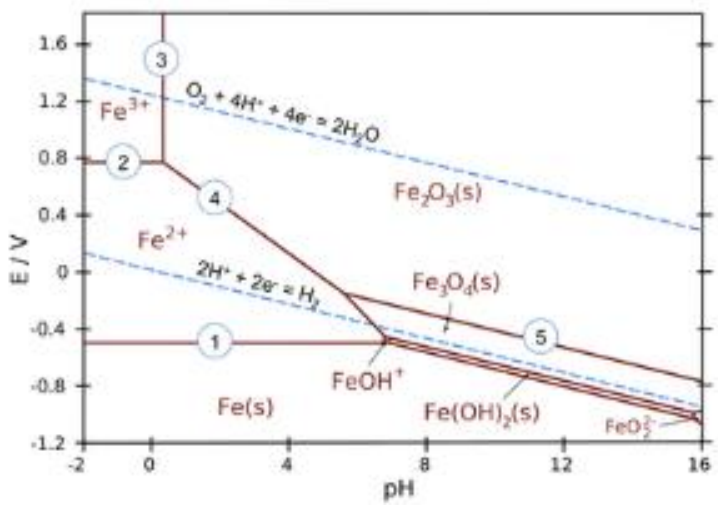


Figure 2-4: Pourbaix Diagram for Iron at 25ºC and 10^{-3}M [16]

Because radiation chemistry is strongly affected by the consumption of oxidants and/or production of hydrogen, corrosion processes could potentially control the radiolytic state an irradiated water system assumes. However, because oxidants are produced under net radiolysis, radiation chemistry can also have a strong influence on the corrosion rate and/or potential established in a freely corroding system.

Past studies have shown that at slightly alkaline conditions (~ pH 10) there are three regions of oxidation on carbon steel surfaces, which depend on the electrochemical potential (E) established, as shown in Figure 2-5 [17]. In region I ($E < -0.5V$ vs. SCE) steel actively corrodes to form a mixture of Fe (II) and Fe (III) oxides and hydroxides. Under these conditions the main oxide formed is Fe_3O_4 which is somewhat protective, but is also conductive allowing continuous oxidation and film growth. In region II ($0.5V < E < 0V$ vs. SCE), magnetite is quickly formed and then further oxidized to form a thin outer layer of

maghemite, above the magnetite layer. Maghemite is more insulating than magnetite and hence passivates the surface. Region III (E > 0 V vs. SCE) brings about the anodic conversion of magnetite and maghemite to lepidocrocite, inducing micro-fractures into the oxide film. This leads to reconstructing of the film with the result being the formation of a thick, but less protective, porous oxide layer of magnetite, maghemite and lepidocrocite.

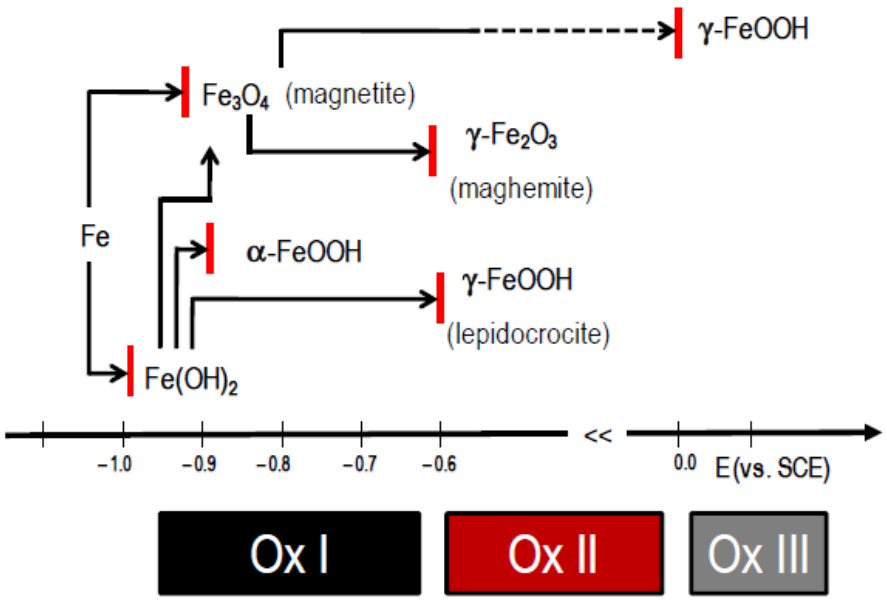


Figure 2-5: Equilibrium Potentials for Various Iron Oxidization Processes [26]

Therefore a system under more reducing conditions (i.e. low dissolved O_2) would most likely result in oxide formation occurring in region I, and hence, form magnetite via hydrogen evolution. However, corrosion processes would slow as the layer of magnetite thickened, thereby reducing hydrogen production. If oxygen was then introduced to the system, magnetite would likely exhibit some oxygen removal ability, as the potential shifted into region II. This would involve the conversion of magnetite to an even more

passive maghemite. Under a steady state condition in region II, it is likely that very little oxygen removal would occur, however, if the system then became irradiated, hydrogen peroxide would begin to form. Past works have shown that this would raise the corrosion potential, however, not necessarily enough to place the system into region III [18].

Studies have shown that under net radiolysis conditions, direct oxidation on steel surfaces is mostly dominated by the molecular species (i.e. H_2O_2 and O_2), not the radical species (e.g. OH) [18]. This is attributed to the low level steady state concentrations and high reactivity of the radicals. Rather than contributing to surface reactions, radical species are more likely to recombine or react with water impurities [18]. Therefore, the true corrosion rate would be proportional to the sum of the consumption rates of H_2O_2 and O_2 on the steel surfaces. These studies have further concluded that hydrogen peroxide is the key radiolysis product governing carbon steel corrosion processes, and less so oxygen [18].

2.3 The Calandria Vault and End Shield Cooling System

The calandria vault and end shield cooling system's primary function is to act as a biological shield, protecting the surrounding environment from the high levels of radiation produced in the reactor core. The system consists of two end shields through which the fuel channels pass, and a concrete, carbon steel walled vault that surrounds the body of the calandria. The system contains approximately 567 m^3 of light water which is circulated from the vault and through the end shields to cool the carbon steel shielding components. The vault contains a nitrogen cover gas to allow for expansion during reactor start-up. The system is operated slightly above atmospheric pressure (≈18 kPa_g), at alkaline pH (9.0-10.0

adjusted w/ LiOH), and with temperatures ranging from 40ºC – 65ºC. A simplified process flow diagram for the system is displayed in Figure 2-6.

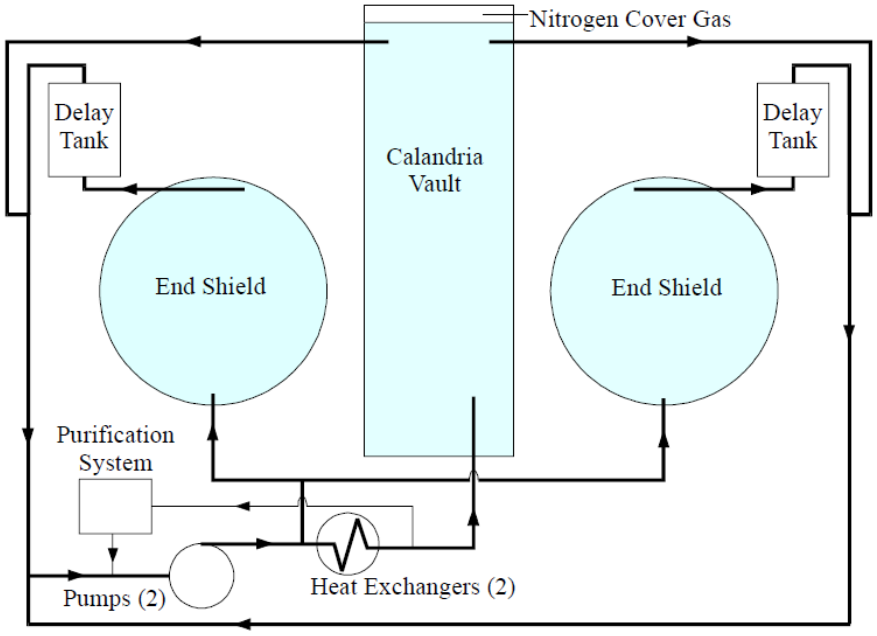


Figure 2-6: Simplified End Shield Cooling System PFD [1]

The Point Lepreau Nuclear Generating Station began operations in 1983, and has since required make-up water for the ESC system due to a small leak in the calandria vault. The make-up water is air saturated (≈ 8 mgO_2/kg) and comes from the facilities water treatment plant. For the first six years of operation hydrogen concentrations in the vault cover gas system were well below the action limit of 2 vol%, which is set to mitigate the buildup for flammable gas mixtures. In 1989 the hydrogen concentration began to regularly exceed this action limit, which resulted in the need for frequent purging of the cover gas system. The hydrogen production was attributed to the net radiolytic breakdown of water, whereby significant quantities of hydrogen, oxygen and hydrogen peroxide are formed [1].

However, the question still remains: What mechanism was responsible for the net radiolytic suppression that occurred from 1983 to 1989? It has been theorized that net suppression was maintained during this period due to oxygen removal and hydrogen production by corrosion of the carbon steel system components. The oxygen added to the system in the makeup water would be readily consumed on the steel surfaces. This would maintain net radiolytic suppression, while hydrogen evolution would add the excess hydrogen required to keep the system in suppression. It has been hypothesized that this suppression mechanism was ceased due to passivation of the steel. Corrosion processes occurring under the conditions present in the ESC system (pH 9.0-10.0) will result in the formation of oxide films on the steel surfaces, which will cause a slowing of the corrosion processes, and consequently, the consumption of oxygen and evolution of hydrogen. A better understanding of the synergies between radiation chemistry and corrosion will give insight into the mechanisms that maintained net radiolytic suppression from 1983 to 1989 in the ESC system at PLNGS.

As mentioned previously, hydrogen production was initially dealt with by periodically purging the cover gas system. However, this method did not address the issue of frequent IX resin saturation brought on by the uptake of nitrates and nitrites being produced from interactions between nitrogen and radiolytically produced oxygen. Furthermore, the method of cover gas purging was time consuming, labour intensive, and also increased the radiation dose uptake by personnel performing the procedure. Therefore, other means of mitigating flammable cover gas concentrations were explored [2]. Many other irradiated

reactor systems use hydrogen addition to achieve net radiolysis suppression, however, the ESC system operates only slightly above atmospheric pressure (≈18 kPa_g). Therefore, if hydrogen was added, it would readily diffuse into the nitrogen cover gas and only exacerbate the problem. Currently, PLNGS controls hydrogen production by periodically injecting hydrazine (N_2H_4) into the system at specified frequencies to act as an oxygen scavenger.

2.3.1 Hydrazine Additions

Hydrazine has been used as an oxygen scavenger in the steam cycles of thermal and nuclear plants for many years to minimize corrosion [10]. When used in a steam cycle, hydrazine depends on the high temperature conditions to promote its oxygen scavenging ability whereas, in the ESC system, it relies on a mechanism promoted by water radiolysis due to the low operating temperature.

Though oxygen removal via hydrazine injections is dependent on a radiation field it is very effective, even under low field intensities. This proves to be useful during shutdown conditions when radiation fields are at a minimum. The high efficiency of oxygen removal by means of hydrazine injections can be attributed to a chain reaction. The first stage in the chain reaction is the initiation step, whereby hydrazine reacts with hydroxyl radicals (reaction (2-17)) and oxygen with hydrated electrons (reaction (2-18)) [19].

Initiation

$$N_2H_4 + \cdot OH \rightarrow \cdot N_2H_3 + H_2O \quad (2\text{-}17)$$

$$e^-_{(aq)} + O_2 \rightarrow O_2^- \quad (2\text{-}18)$$

The second stage, propagation, is displayed in reactions (2-19) and (2-20). The hydrazyl radical reacts with oxygen forming N_2H_2, H^+ and O_2^-, after which O_2^- reacts with hydrazine forming a hydrazyl radical and HO_2^-. The formation of this secondary hydrazyl radical can propagate further oxygen consumption by feeding reaction (2-19) [19].

Propagation

$$\cdot N_2H_3 + O_2 \rightarrow \cdot N_2H_2 + O_2^- + H^+ \quad (2\text{-}19)$$

$$N_2H_4 + O_2^- \rightarrow \cdot N_2H_3 + HO_2^- \quad (2\text{-}20)$$

The termination stage, displayed below in reactions (2-21) – (2-23), is simply the disproportionation of O_2^- / HO_2 [19].

Termination

$$HO_2 + HO_2 \rightarrow H_2O_2 + O_2 \quad (2\text{-}21)$$

$$HO_2 + O_2^- \xrightarrow{H_2O} H_2O_2 + O_2 + OH^- \quad (2\text{-}22)$$

$$O_2^- + Reactants \rightarrow Products \quad (2\text{-}23)$$

Following the mechanism described above is series of reactions involving a range of N-O compounds that end in the formation of water and molecular nitrogen, the net effect of the entire process is shown by reaction (2-24) [19].

$$N_2H_4 + O_2 \xrightarrow{Ionizing\ Radiation} N_2 + 2H_2O \quad (2\text{-}24)$$

This process can quickly consume any oxygen present in the system which will result in the reversion back to net radiolytic suppression [9].

2.3.2 Methanol as an Oxygen Scavenger

Due to the strict handling procedures on hydrazine, interest has been expressed in investigating methanol as a potential alternative. Unlike hydrazine, methanol would not function as an oxygen scavenger in high temperature systems. Its scavenging mechanism is completely dependent on the presence of a radiation field, making it only a candidate for irradiated systems. Methanol in irradiated water systems will readily react with hydroxyl radicals and hydrogen atoms to produce the hydroxymethyl radical as shown in reactions (2-25) and (2-26) [5].

$$CH_3OH + \cdot H \rightarrow \cdot CH_2OH + H_2 \quad (2\text{-}25)$$

$$CH_3OH + \cdot OH \rightarrow \cdot CH_2OH + H_2O \quad (2\text{-}26)$$

The molecular hydrogen produced from reaction (2-25) will assist in the reversion to a net radiolytically suppressed state, however, oxygen is also readily consumed by the hydroxymethyl radical as shown by reaction (2-27) [20].

$$\cdot CH_2OH + O_2 \rightarrow Products \quad (2\text{-}27)$$

Several intermediate products can be formed such as ethylene glycol and formaldehyde, however, they will all undergo oxidation/reduction reactions until carbon dioxide and water are formed (the overall result is displayed in reaction (2-28)) [5].

$$2CH_3OH + 3O_2 \rightarrow 2CO_2 + 4H_2O \quad (2\text{-}28)$$

Because carbon dioxide is a by-product of methanol's oxygen scavenging mechanism, a depression of system pH may occur due to the formation of carbonic acid; reaction (2-29).

$$CO_2 + H_2O \leftrightarrow H_2CO_3 \quad (2\text{-}29)$$

Carbonic acid is a weak acid, so the effects of its dissociation may not be detrimental. From a large-scale perspective, if scaled up to plant application, more frequent exhaustion of the ESC system's IX resin may occur due to uptake of carbonates and bicarbonates. An investigation into the use of methanol as an oxygen scavenger under conditions comparable to the ESC system was performed; the results and potential downfalls are discussed in later sections.

3. Experimental Test Methods and System Design

3.1 Loop Overview

All experiments were carried out in a low temperature, low pressure flow-loop constructed of ¼ inch - 316 stainless steel tubing. Water with varying concentrations of oxygen, hydrogen and hydrogen peroxide were circulated through a test section composed of a 1 liter PYREX® vessel and a 2-inch long section of ½ inch - 316 stainless steel tubing. The tube section could be packed with up to approximately 22 grams of 0.8 mm AISI 1010 carbon steel ball bearings to simulate corrosion effects. AISI 1010 carbon steel falls within the specification for end shield cooling system ball bearings in CANDU 6 reactors, which specifies any carbon steel between AISI 1008 and 1026, excluding 1024, with a maximum cobalt and manganese content of 0.07%, and 1.0%, respectively. The composition of the test section balls used is displayed in Table 3-1.

Table 3-1: Carbon Steel Test Section Balls' Composition

Component	Content
Carbon	0.1% - 0.2%
Manganese	0.6% - 0.9%
Silicon	0.1% - 0.2%
Sulfur	<0.5%
Phosphorous	<0.040%
Iron	Balance

The vessel portion of the test section was used to maintain the majority of the system volume in the radiation field. This ensured sufficient residence time in the field for full development of the radiation chemistry prior to interactions with the carbon steel surfaces.

The radiation field was applied using a ^{60}Co Gammacell 220 irradiator, which provided an approximate dose rate of 500 Gy/hr. The test section was immersed and removed from the radiation field via an elevator chamber built into the Gammacell. A simplified process flow diagram is displayed in Figure 3-1, however, a detailed PFD can be found in Appendix A.

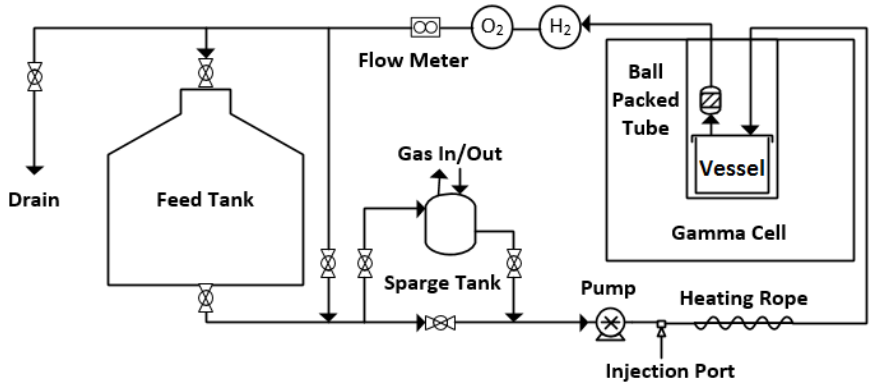


Figure 3-1: Simplified Process Flow Diagram of Test Loop

3.2 Loop Flow Configurations

The loop was designed such that it is able to operate in a complete re-circulation mode or in a once-through configuration. Once-through configuration required dissolved gas concentrations to be altered only in the feed tank. Water leaving the feed tank was heated to 30^{o}C, passed through the test section, analyzed for dissolved gas concentrations, and sent to drain. However, it was found that variations in dissolved gases from corrosion processes were not quantifiable from a single pass of the test section. Therefore, all experiments were carried out in a recirculation configuration (i.e. upon commencement of an experiment no water entered or left the system). At the beginning of a recirculation experiment water was circulated through the system from the feed tanks until dissolved gas

concentrations were brought within range of the desired starting conditions. Subsequently, the test section was valved in and the system placed in complete recirculation (i.e. the feed tank was valved out, and the system was placed in a state such that no water entered or left for the duration of the experiment). Dissolved gas concentrations were then fine-tuned using the sparge vessel. The system arrangement allowed for the flow to be rerouted around certain pieces of equipment such as the gas sensors, sparge vessel and test section. For example, prior to commencement of an experiment, once the desired dissolved gas concentrations were achieved, the sparge vessel was valved out for the duration of the test. The detailed set-up and valve turning procedures used in both flow configurations can be found in the loop's operating manual [47].

3.3 Loop Components and Design

3.3.1 Loop Flow Components

The majority of the system was constructed of ¼ inch - 316 stainless steel tubing. All system valves were Swagelok all–purpose, two and three way ball valves and had ¼ inch Swagelok tube fittings on each end, with the exception of the Swagelok check valve located on the recirculation line, and a relief valve positioned at the outlet of the pump. The check valve was a stainless steel poppet with Swagelok tube fittings at each end and served to ensure no back flow occurred as a result of the head from the feed tanks. The relief valve was a stainless steel, low pressure, proportional valve used to ensure no significant buildup of pressure occurred within the system to protect glass system components.

The system pump was a 316 stainless steel micro-gear pump which ran on an Instek High-Current, Single-Output DC Power Supply. This power supply was used to control the flowrate of the system by altering the power supplied to the pump. The pump port size was 0.125 inches with female NPT connections. Tubing was connected to the pump by two 316 stainless steel Swagelok reducing unions which had 1/4 inch Swagelok tube fittings on one end and 1/8 inch male NPT connections on the other. The upstream fitting reduced the diameter to 0.125 inches upon pump entry and the downstream fitting returned the diameter to 0.25 inches upon exit. The pump had a maximum allowable flow rate of 460 mL per minute (well above the experimental flow rate of 200 mL per minute), and a maximum differential pressure of 75 psi.

The system flowrate was monitored through the use of a Brooks Instrument Ar-Mite Low Flow Armored Flowmeter, which was connected to the system tubing by ¼ inch tube compression fittings. The flowmeter's maximum pressure rating was 1500 psig and could measure water flowrates up to approximately 400 mL per minute.

3.3.2 Feed Tanks

Two 50 L, sealed, low density polyethylene carboys served as water reservoirs (feed tanks) to store pH adjusted (9.5 w/ LiOH) and neutral water. The neutral water was used for system washes, and the pH adjusted water for experimental work. Each carboy was topped with a Thermo Scientific Nalgene cap that had been drilled out for the attachment of three Swagelok 316 stainless steel bulkhead unions. A seal was made between the bulkhead unions and the caps using neoprene gaskets. Two of the three channels created by this

modification were used for the inlet and outlet flow of purge gases, which adjusted the dissolved gas concentrations in the water. The gases were bubbled through the water using a fritted glass dispersion tube with an 8 mm (O.D.) tube and a 40 mm medium frit disk to maximize mass transfer. The dispersion tube was glass blown onto a stainless steel bellows to PYREX® adaptor which was attached to one of three bulkhead unions. The gas flow into the tank was controlled by a needle valve attached to the outside portion of the bulkhead union. Polyethylene tubing (1/4 inch) connected the gas cylinder's regulator to the needle valve. The second bulkhead union served to vent the gas being removed from the system. In order to ensure that there was no entry/re-entry of undesired gases into the feed tanks, the vent port was attached to a 1/4 inch polyethylene tube that was submerged into a reservoir of water to act as a gas trap.

The third channel was used as a water return line for the feed tank. At the beginning of every experiment dissolved gas concentrations were brought within the range of desired starting concentrations by circulation through the feed tank, making this return line a necessity. A 3/8 inch Swagelok to BSP thread adapter was attached to the bottom of each tank to serve as an outlet flow line. A 1/4 inch x 3/8 inch reducing union made the connection between the tank outline line and the ¼ inch system tubing.

3.3.3 Sparge Vessel

The sparge vessel, constructed of borosilicate glass, was used to alter dissolved gas concentrations upon entering recirculation configuration (Figure 3-2). Purge gases were bubbled through the water in the vessel by an 8 mm O.D. fritted gas dispersion tube, and

vented through the adjacent flow line. The water flow was directed in through the top of the vessel and out through the bottom in a counter current fashion against the gas flow to promote mass transfer. All flow lines though the sparge vessel were glass blown onto ¼ inch stainless steel bellows to PYREX® adaptors to allow for ease of connection to the ¼ inch tubing of the system.

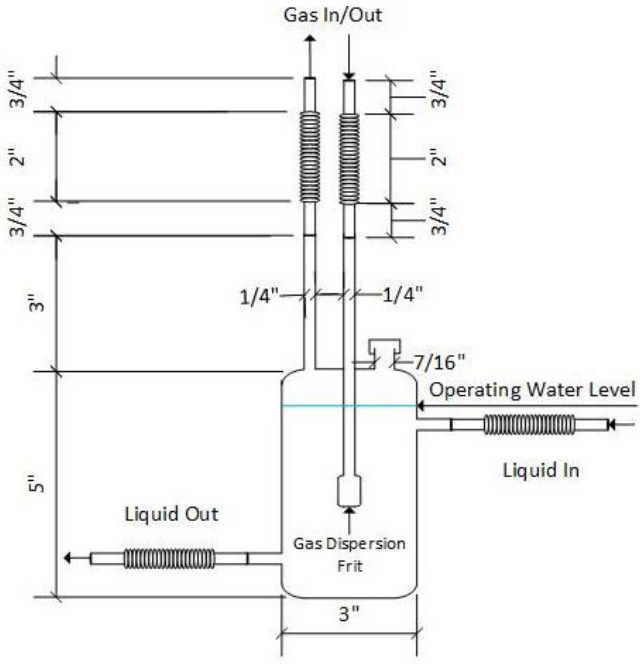


Figure 3-2: Sparge Vessel Design and Flow Configuration

Dissolved gas concentrations in the system were also altered by chemical additions (e.g. hydrazine, methanol, sodium nitrate), which were made through an injection port placed between the pump and test section. The port was a 1/8 inch Valco septum injector nut, swaged onto a Swagelok reducing union tee (1/4 in x 1/4 in x 1/8 in) directly in line with

the main system flow. Injections were made using a micro-liter syringe and amounts of pure or analytically diluted solutions of known composition.

3.3.4 Temperature Control

To maintain a constant system temperature, a heating rope was used in conjunction with a bench-top temperature controller and thermocouple. The rope heater was of the OMEGA FGR series, with a temperature rating of 482°C (operating temperatures did not exceed 30°C). Each end of the heating rope terminated with 610 mm, (24") long, fiberglass insulated leads that were wired to the temperature controller. The temperature controller was of the OMEGA CSi32 series with an operating range of -210°C to 760°C.

A J-Type, 6 inch long, sheathed thermocouple with a diameter of 1/8 inches was connected into the loop immediately downstream of the heating rope. It was connected perpendicular to the main flow using a teed-off tube and a Swagelok, stainless steel, bored-through, reducing union. The reducing union had a 1/4 inch tube adapter at one end (to attach the tee-fitting) and a 1/8 inch tube fitting at the other (to attach to the thermocouple). This thermocouple was wired to transmit temperature readings back to the controller, which adjusted the output of the heating rope to obtain the set point specified.

3.3.5 Test Section

The test section was composed of a 1 L PYREX® vessel and a 2 inch long portion of ½ inch – 316 Stainless Steel tubing, that could be packed with up to about 22 grams of 0.8mm carbon steel balls (Figure 3-3). The PYREX® to steel connections were made using ¼ inch

stainless steel bellows to PYREX® adaptors that had been glass blown onto the vessel. The bellows type fittings were chosen to minimize the amount of stress put on the PYREX®. The bellows were connected to the ¼ inch system tubing using ¼ inch Swagelok tube adapters. The inlet flow line protruded into the vessel and approached the bottom to propagate mixing, and avoid channeling or dead zones. The outlet line was placed at the top, center point of the vessel, with the vessel top gradually curved upwards towards the exit to avoid bubble retention.

The residence time for the test section was about 5 minutes, while the remainder of the loop was about 1-2 minutes, meaning the majority of the water in the system was constantly irradiated when the test section was in the Gammacell. The packed tube of carbon steel balls was placed on the outlet line of the PYREX® vessel to ensure that radiation chemistry would be fully developed prior to interactions with the carbon steel surfaces within. The carbon steel balls used within the test section were 0.8 mm AISI 1010 carbon steel balls, which as mentioned previously, fall within the specification for the shielding balls used in the ESC system at PLNGS. The small ball diameter was chosen to maximize the surface-to-volume ratio for corrosion effects. When the tube was fully packed, the surface area produced was about 2 dm^2. The ball-packed tube was 2 inches in length and ½ inches in diameter and was connected to the ¼ inch system tubing using two ½ inch x ¼ inch reducing unions with Swagelok tube adaptors at each end. To ensure that the carbon steel balls remained intact, stainless steel perforated plates and screens were placed at each end of the tube. The screens and plates were fabricated such that they had a diameter equivalent

to that of the tube (1/2 inches). The plate and screen were positioned into each end fitting after which the tubing was placed in and secured.

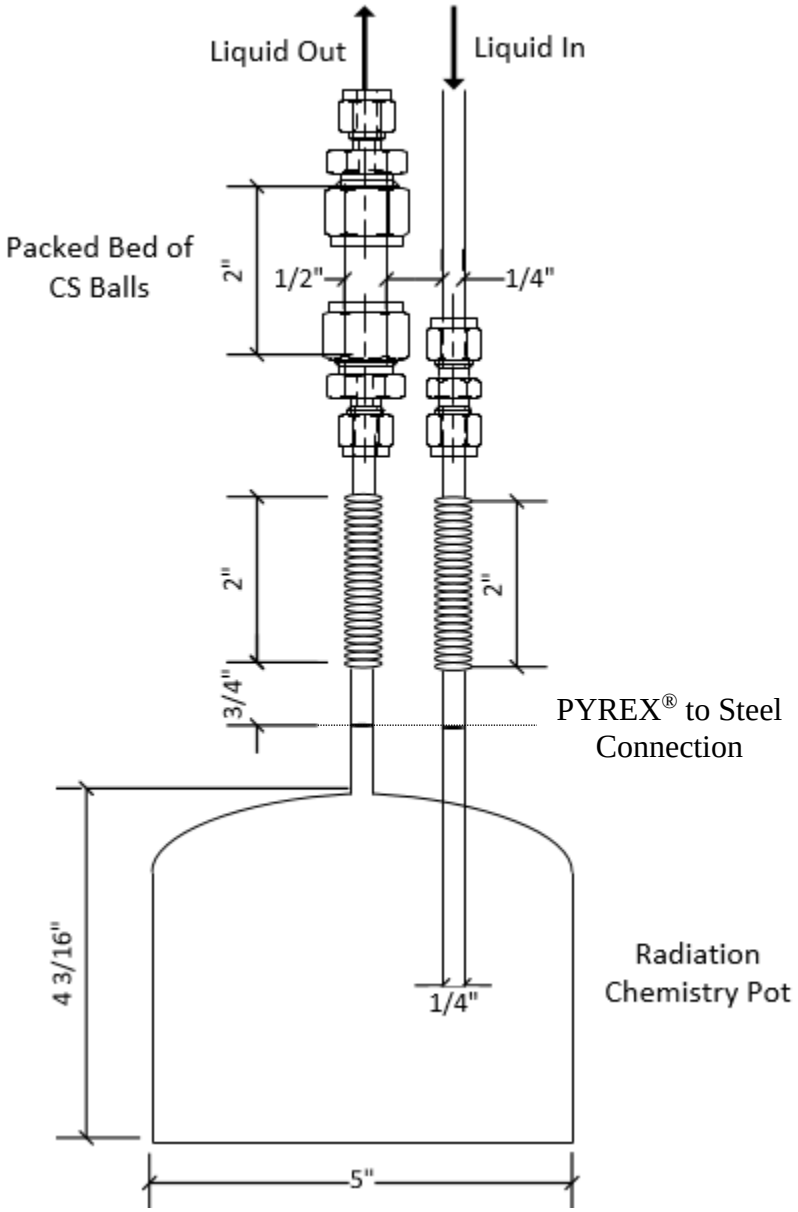


Figure 3-3: Test Section Design and Flow Configuration

3.3.6 Orbisphere Analyzers – Dissolved Gas Measurement

Water leaving the test section was analyzed downstream for dissolved hydrogen and oxygen concentrations by a two-channel table top model 510 Orbisphere analyzer. Oxygen and hydrogen measurements were taken by Models 31110.11 and 31210.11 electro-chemical sensor probes, respectively. An image of the electrochemical sensor face can be seen in Figure 3-4.



Figure 3-4: Orbisphere Electro-chemical Sensor Face

Within the Orbisphere sensor cells (shown in Figure 3-4) there is a center electrode (O_2: cathode, H_2: anode) and a counter electrode (O_2: anode, H_2: cathode), both of which are immersed in electrolyte, and covered with a membrane. The dissolved gas in the water diffuses into the electrolyte though the membrane and is consumed at the cathode (O_2) or anode (H_2). The reactions occurring on the electrodes generate a current which is proportional to the concentration of the gas entering the cell, which is proportional to the concentration of the gas in the liquid phase opposite the membrane. The device is capable of measuring hydrogen content to within +/- 0.03 ppb (range: 0 to 75 ppb) and oxygen content to within +/- 0.1 ppb (range: 0 ppb to 20 ppm).

The Orbisphere was connected into the system through a flow chamber. This chamber was connected to the system's ¼ inch tubing through two, ¼ inch NPT x ¼ inch Swagelok tube fittings. As per the recommended configuration, the inlet and outlet lines of the Orbisphere flow chamber each contained a one-piece, three-way ball valve, with ¼ inch tube fittings on each end. These valves allowed for measurements and calibrations to be done without having to disconnect a line manually. When calibrating the equipment, the sample flow was shutoff and the calibration gas was rerouted through each three-way ball valve; the probes were calibrated with each experiment.

3.4 Conductivity and pH Measurements

Conductivity and pH measurements were taken prior to and following each experiment. Samples were taken downstream of the test section through a system sample port, which consisted of a teed-off stainless steel tube section, a one-piece ¼ inch ball valve and a short section of 1/8 inch stainless steel tubing. Samples were taken into fresh centrifuge tubes, and immediately measured for conductivity and pH; the meters were calibrated with each use.

A pH meter measures the pH of a solution using an ion-selective, two-electrode system. The two electrodes, referred to as the internal and reference electrodes, are submerged in isolated buffered electrolyte solutions. The potential at the internal electrode can vary depending upon the hydrogen ion concentration of the sample solution in which the pH probe is submerged. The reference electrode is maintained at a constant, known, potential, and is used as a reference to changes in potential at the internal electrode. The internal

electrode and electrolyte solution are contained in a glass compartment, which protrudes into the sample solution. A specially designed glass bulb separates the internal electrode and electrolyte from the sample solution. The bulb acts as a membrane and has an affinity for hydrogen ions. When the hydrogen ion concentration varies between the internal electrolyte and the sample solution, a potential difference will form which is proportional to the pH of the sample solution.

Solution conductivity meters work by applying power to two even surface area electrodes, spaced at a specific distance. The electrodes are submerged into the sample solution, and the current flow between the electrodes is measured. The measured current is then directly proportional to the resistance or conductivity of the sample solution in question.

Conductivity and pH measurements of pre-experiment samples were tested against one another to verify readings. This was a simple analysis since the only ions significantly contributing to solution conductivity, at that point, were those added to adjust pH (i.e. LiOH).

3.5 Preparation of Solutions

Throughout the course of the project, solutions of methanol, hydrazine, and lithium hydroxide were used. Lithium hydroxide was used for pH adjustments, while methanol and hydrazine were used as oxygen scavengers in irradiated experiments.

When prepping a solution of lithium hydroxide for injection into the loop, a specific quantity of LiOH salt was weighed out in a weigh tray on an analytical balance. The salt

was emptied into a volumetric flask, and filled about half way to the mark with DI water. The flask was swirled until all salt appeared to have dissolved, and was diluted to the mark. The flask was then capped and mixed again by turning the flask up-side down, and right side up several times.

When prepping a hydrazine or methanol solution, an aliquot of concentrated methanol or hydrazine was poured into a beaker and pipetted into a volumetric flask. The flask was then filled about half way to the mark with DI water and swirled rigorously. The flask was then filled to the mark with DI water, capped, and again mixed by turning the flask upside down, and right-side up several times.

3.6 SEM and EDS

3.6.1 Scanning Electron Microscopes

A scanning electron microscope (SEM) was used for the surface characterization of the carbon steel balls used in the experiments. SEMs use a focused beam of high energy electrons to scan the surface of the specimen / sample. This generates numerous signals that speak to the specimen's chemical composition, physical characteristics, and morphology. The surface of the specimen can be mapped by the return intensity of certain signals relative to the beam position. [22]

An SEM uses an electron gun as source of electrons, which are accelerated though an anode and controlled using magnetic lenses and apertures. The beam of electrons bombard the

sample, and upon interaction generate various signals which can be processed to produce information about the sample (i.e. images, chemical composition, etc.). [22]

The elections incident on the sample can either partake in elastic or inelastic collisions with the specimen. Elastic collisions are a result of interactions between electrons and the nucleus of the atoms. The electron will effectively change its trajectory with very little change in kinetic energy and is elastically “back scattered”. These back scatter electrons can give insight into the composition of the specimen. The intensity of back scatter electrons produced can be directly related to the atomic weight of the sample for a given incident beam intensity / energy level. [23]

Inelastic collisions result in the formation of secondary electrons and x-rays, and cause more significant decline in the kinetic energy of the incident electron. Secondary electrons are produced from inelastic collisions that result in an electron losing its energy directly from the collision event or the ejection of an electron from an excited atom due to its interaction with another electron. Secondary electrons have significantly less energy than back scatter electrons, but the flux of secondary electrons produced is a function of the sample’s surface orientation. The image produced from their flux intensities at given x-y positions on the sample can mimic topography. Secondary electron signals are insensitive to atomic weight, but are very sensitive to surface tilt, which make secondary electron signals ideal for imaging topography and depth of field perception. [23]

3.6.2 Energy Dispersive X-ray Spectroscopy

Characteristic x-rays can also be produced from inelastic collisions between electrons. Characteristic x-rays are formed when an inner shell ionization occurs, leaving the atom in an excited state. To relax to ground state, an electron from an outer shell will drop into the inner shell of the atom. The inner shells of atoms are often referred to as the K, L, M, & N shells, as displayed in Figure 3-5. Upon the electron dropping into a lower energy shell, a characteristic amount of energy is released in the form of an x-ray. The energy levels of electrons in these orbitals are discrete, and characteristic to the element of which the atom makes up.

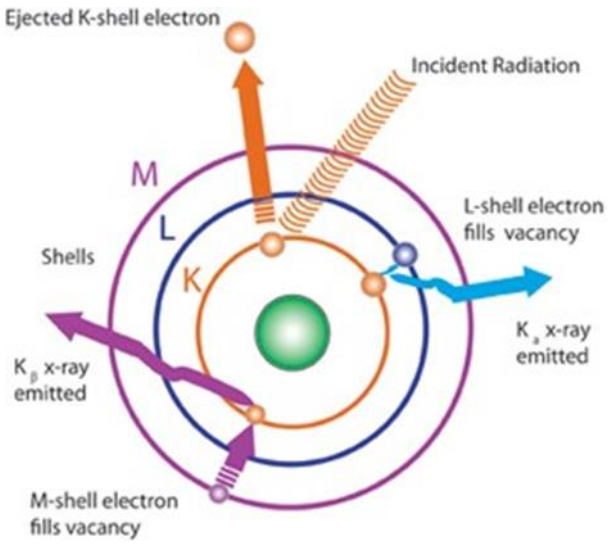


Figure 3-5: Characteristic X-ray Formation [23]

For example, the difference in energy of electrons between the K and L shell of an iron (Fe) atom are different than those between the K and L shell of an oxygen atom, therefore

the energy of the x-ray produced from the L to K transition in iron is specific to iron and likewise for oxygen. [23]

The characteristic x-ray produced is named for the vacant shell that the electron entered to produce said x-ray. For example, if the electron enters the K shell from the L shell the x-ray is referred to as “K-alpha”, alternatively, if the electron enters the K shell from the M shell the x-ray is referred to as “K-beta”. The same naming system holds true for electrons entering the L shell from the N or M shells (i.e. an electron from the M shell would be “L-alpha”).

These characteristic x-rays are quite valuable in determining not only what species are present in a sample, but also can give quantitative analysis. The more of a given element that is present, the higher its characteristic x-ray intensities will be. The energy level of the x-rays produced can be related to elemental composition, and the intensity of the x-rays at a given energy level is indicative of the quantity of the given element present. [23]

3.7 Hydrogen Peroxide Assay

Since hydrogen peroxide is a product of radiolysis, some measurements were taken following radiation experiments to gather insight as what its net radiolysis, steady state concentration may be. No online measurements of H_2O_2 were taken, and sampling during tests presented difficulties due to the closed-loop nature of the system. However, at the end of the tests, while the system was still under net radiolytic conditions, samples were taken in order to conduct hydrogen peroxide assays using the Ghormley tri-iodide method [24].

The absorbance (A) of a solution at a given wavelength is directly proportional to the concentration of the absorbing species, which in this case is the tri-iodide ion (I_3^-).

$$A = \varepsilon b[I_3^-] \tag{3-1}$$

The tri-iodide ion has a maximum absorbance (ε) at a 350 nm wavelength of approximately 25,500 L/mol.cm [25]. Since the same cuvette is used in every analysis the path length of the light (b) and the molar extinction coefficient (ε) can be lumped into a constant term k'.

$$A = k'[I_3^-] \tag{3-2}$$

In this method the tri-iodide ion concentration can be taken as representative of the concentration of hydrogen peroxide. Under acidic conditions, iodide ions are readily oxidized to tri-iodide by hydrogen peroxide in the presence of an ammonium molybdate catalyst, as shown in reaction (3-3) [24].

$$3I^- + H_2O_2 + 2H^+ \rightarrow I_3^- + 2H_2O \tag{3-3}$$

Therefore, the concentration of hydrogen peroxide in a given sample at these conditions can be easily determined by measuring the absorbance of the tri-iodide ion.

$$A = k'[H_2O_2] \tag{3-4}$$

The analysis is conducted by mixing two reagent solutions. The first contains 33 g of potassium iodide (KI), 1.0 g of sodium hydroxide (NaOH), and 0.1 g of ammonium molybdate ($(NH_4)_6Mo_7O_{24}$), diluted with DI water in a 500 mL volumetric flask. Sodium hydroxide is added to the solution to produce alkaline conditions as to mitigate pre-

oxidation of the iodide. The second solution contains 10 g of potassium hydrogen phthalate ($C_8H_5KO_4$), this reagent drops the pH of the solution to promote reaction (3-3). When conducting the analysis, 10 mL of the first solution, followed by 10 mL of the second solution, are pipetted into a 25 mL volumetric flask and swirled. An aliquot of the loop sample (2 mL) was added to the mixture in the volumetric flask, then filled to the mark with DI water, and mixed. The absorbance of the mixture was then measured as to determine the hydrogen peroxide content. A calibration curve was generated using samples with known quantities of peroxide, and is displayed in Figure 3-6.

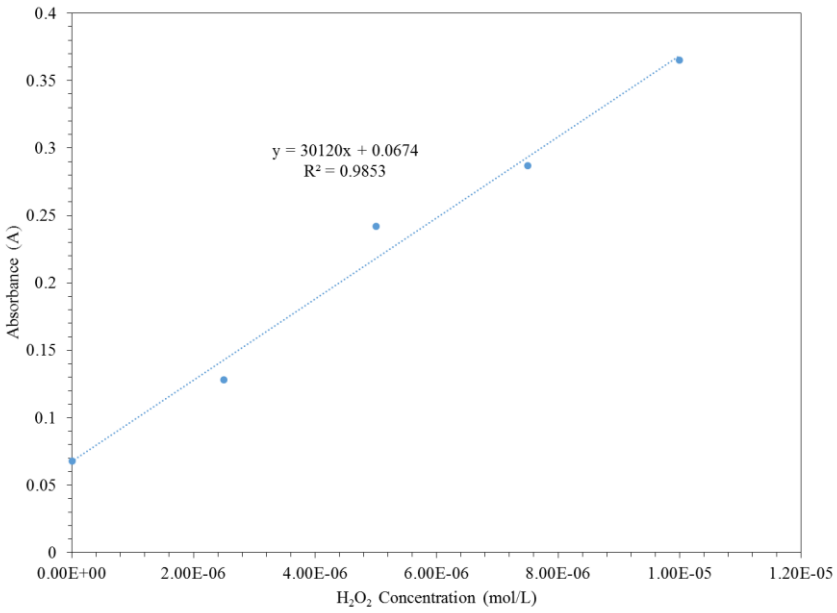


Figure 3-6: Hydrogen Peroxide Assay Calibration Curve

This renders a value for the constant "*k*" of 30120 L/mol, and can be used in determination of hydrogen peroxide concentrations at any value, although a blank absorbance measurement term should also be included. This accounts for absorbance of the DI water

with no hydrogen peroxide present (A_0), which was measured to be 0.068. By incorporating this term, equation (3-4) can be written as displayed in equation (3-5).

$$A = \left(30120 \frac{L}{mol}\right)[H_2O_2] + 0.068 \quad (3\text{-}5)$$

3.8 Pre-aging Carbon Steel Balls

In order to observe differences in behavior between fresh carbon steel balls, and carbon steel balls aged under reducing and oxidizing conditions, samples were aged in an autoclave prior to insertion into the test section. To produce a reducing environment, carbon steel balls were placed into an autoclave with 60 mL of DI water. The carbon steel balls were held above the water level using a specially designed mesh support basket (See Figures A-3 and A-4). The autoclave was capped, and an argon flow was applied through a stainless steel tube submerged into the water. The gas purged the system for a period of 4 hours to remove any oxygen present. All valves on the autoclave were then closed, and the autoclave was heated to 300 ^{o}C and approximately 1200 psig. The system was maintained at these conditions for a period of 4 days. Carbon steel balls aged under oxidizing conditions were processed using a similar procedure, whereby air replaced argon as the purge gas. A detailed drawing of the system configuration is displayed in Appendix A.

3.9 Loop Commissioning

Prior to undertaking any experimental work, the system underwent a series of commissioning tests to ensure dissolved gas concentrations and other system parameters

could be controlled and remained stable (e.g. temperature, pH, flowrate, etc.). Commissioning tests demonstrated that the loop was gas-tight, however, the temperature controller presented some issues.

The temperature controller that was initially installed into the system was an on-off type controller. A differential gap is generally applied to these types of controllers to inhibit rapid cycling, this causes the measured variable to oscillate above and below the set point over longer periods. Because the dissolved gas concentrations are temperature dependent, this caused large fluctuations in the gas concentration readings.

To better control the system parameters, a PID controller was installed into the loop. Following the installation of this controller the system parameters were easily controlled and maintained during loop operation.

4. Results

4.1 Corrosion Experiments

4.1.1 Once-Through Corrosion-Only Tests

Corrosion-only experiments were performed to determine the effects of carbon steel corrosion on dissolved gas concentrations in the absence of a radiation field. Preliminary tests were carried out in a once-through flow configuration, whereby water entering the test section was fresh from the carboy, and upon exiting the test section was sent to drain after passing through the dissolved gas analyzers. The results from a once-through, corrosion-only test are displayed in Figure 4-1.

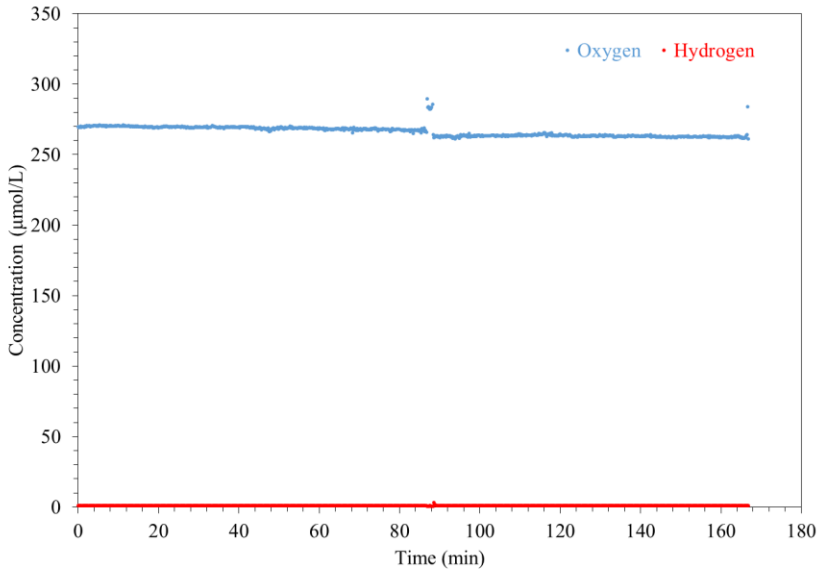


Figure 4-1: Once-through Corrosion-Only Test

Unfortunately, no measureable oxygen consumption or hydrogen evolution was observed from these experiments. Further testing was then carried out in a recirculating fashion, such that once the experiment began no water entered or left the system. Early recirculating, corrosion only experiments exhibited oxygen ingress behavior, which was traced to the system's sparge vessel. Therefore, all subsequent experiments were carried out with the sparge vessel valved-out. This effect was verified with a model and is described in Appendix B.

4.1.2 Recirculating Corrosion-Only Tests

The results produced from a recirculating corrosion-only test are displayed in Figure 4-2. Oxygen consumption began and was established at a rate of approximately 1100 μgO_2/L.day (33 $\mu molO_2$/L.day) in the linear portion of the plot. The oxygen consumption behavior was relatively linear and seemingly independent of oxygen concentration. However, when the oxygen concentration fell below approximately 2.5 $\mu molO_2$/L, the trend was no longer linear. The oxygen consumption that occurred in this test is completely attributed to corrosion of the carbon steel, as little to no oxygen consumption occurred during loop commissioning when no carbon steel was present.

No measurable hydrogen evolution from corrosion occurred until all oxygen was removed from the system, after which, there appears to be a transition period that lasts for approximately 1000 min. During this period, unmeasurable quantities of oxygen were likely removed and the dominating cathodic process underwent a transition from oxygen reduction to proton reduction (hydrogen evolution). Once established, proton reduction

resulted in an average hydrogen evolution rate of approximately 26 $\mu gH_2/L.day$ ($13\mu molH_2/L.day$).

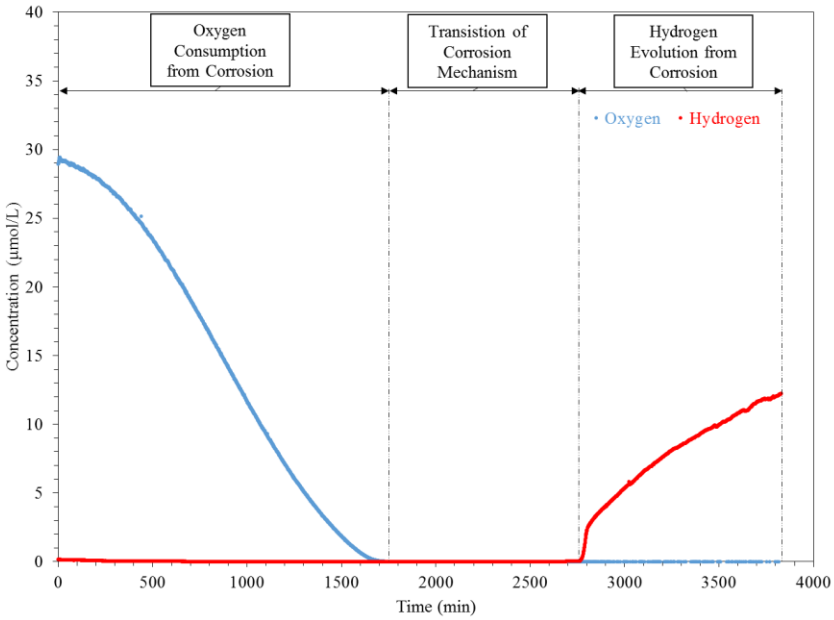


Figure 4-2: Recirculating Corrosion-Only Experimental Results

Corrosion and penetration rates were inferred from these oxygen consumption and hydrogen production rates simply through stoichiometry. It was assumed that all oxygen consumption and hydrogen production was due to the oxidation of Fe to Fe^{2+}, and the loop volume was approximately 1.2 L. The corrosion and penetration rates from oxygen consumption and hydrogen production were estimated as $2.20mg/dm^2/day$ (10.23µm/year) and $0.43mg/dm^2/day$ (2.0µm/year), respectively. Detailed calculations of the corrosion and penetration rates are displayed in Appendix C.

4.2 Radiation Chemistry Tests

Radiation chemistry tests were carried out without the insertion of carbon steel balls into the test section. These tests were targeted at forming base-line results for the effects of radiation chemistry on dissolved gas concentrations in the absence of carbon steel corrosion.

Results produced from a radiation chemistry test are displayed in Figure 4-3. The test section was irradiated from time 0 min through to the end of the experiment at approximately 1000 min. Upon irradiation oxygen was immediately consumed at a slowing rate until it reached a steady state concentration of approximately 20 μmol/L at around 100 min. Hydrogen was immediately produced at a slowing rate until, it too, reached a steady state concentration just above 10 μmol/L. This test well represents the conditions expected in net radiolysis, i.e. significant, steady state concentrations of dissolved hydrogen and oxygen [11]. Although oxygen is generally anticipated to increase in concentration under net radiolysis conditions, its consumption of approximately 5 μmol/L upon irradiation of the test section, was attributed to the formation of hydrogen peroxide.

It should be noted that oxygen was also consumed at a very slow rate under "steady state" net radiolysis conditions; this is attributed to the consumption of oxidants (i.e. H_2O_2) on the stainless steel surfaces of the loop. To analyze for hydrogen peroxide content, samples were taken following each experiment. Unfortunately, the sample assays rendered non-detectable concentrations of hydrogen peroxide. The reagent solutions used in the Ghormley method were down scaled in an attempt to raise the relative hydrogen peroxide

concentrations in the final assay solutions, however, non-detectable readings were still generated. The limit of detection for this method is approximately 10^{-6} mol/L in the final assay solution [24]. It is likely that the hydrogen peroxide concentration present in the system, under steady state, net radiolysis conditions, was lower than anticipated due to its consumption on the stainless steel surfaces within the loop.

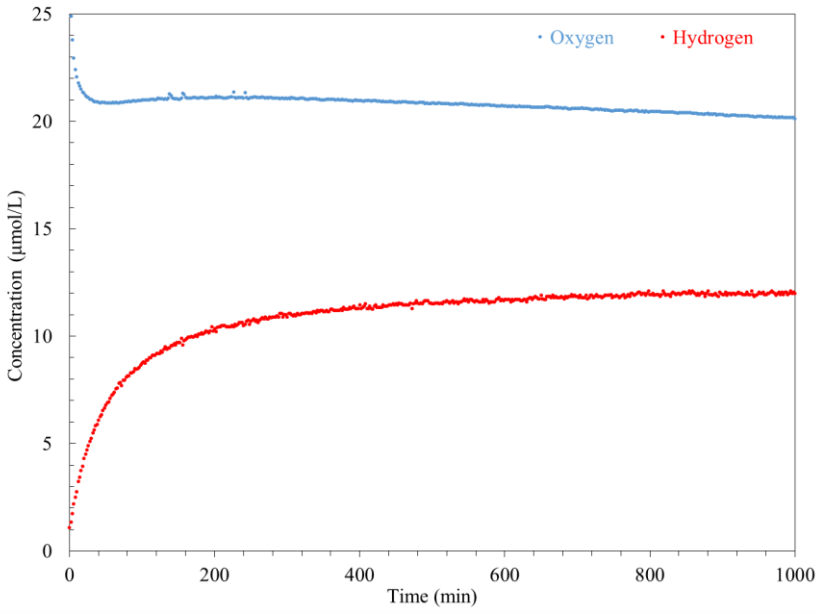


Figure 4-3: Net Radiolysis Experimental Results

4.3 Radiation Chemistry and Corrosion Tests

4.3.1 Corrosion of Fresh Carbon Steel under Irradiated Conditions

After forming a baseline for corrosion and radiation chemistry behavior separately (i.e. how corrosion would affect the dissolved gas concentrations in the absence of radiation chemistry and vice-versa), irradiation experiments were performed with carbon steel

present in the test section. The results acquired from the introduction of fresh carbon steel balls into the irradiated test section are displayed in Figure 4-4.

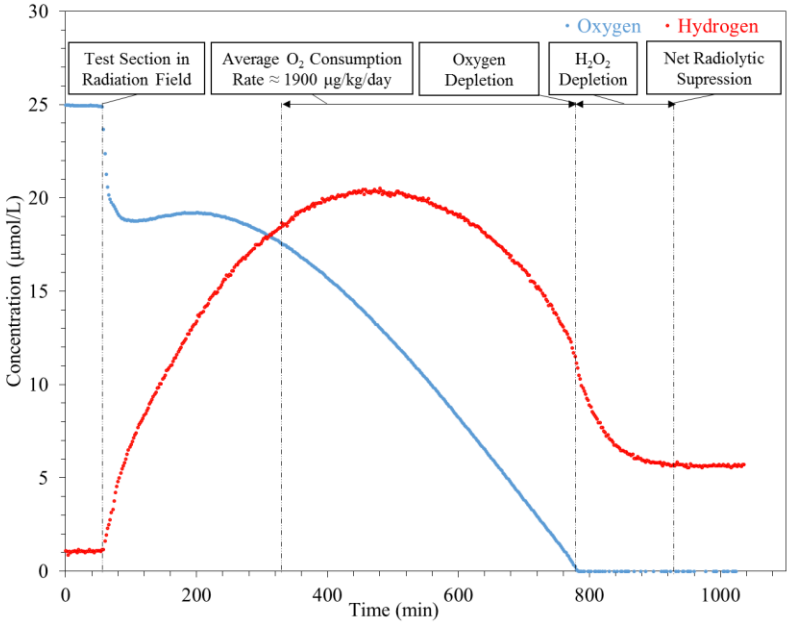


Figure 4-4: Synergistic Effects between the Radiation Chemistry of Water and Corrosion of Fresh Carbon Steel

Irradiation of the test section began at approximately 50 min, which resulted in an immediate, consumption of oxygen. This rapid consumption of oxygen, which ceased at around 100 min, was attributed to the formation of hydrogen peroxide. The oxygen concentration then slightly rebounded. A decrease in oxygen concentration began around 200 minutes. This was due to oxygen consumption by corrosion of the carbon steel overcoming the radiolytic oxidant production rate. Ultimately, the net oxygen consumption rate was nearly double that observed outside of the radiation field (Figure 4-2) until all the oxygen was consumed. At this point the hydrogen concentration continued to decrease as

the remaining hydrogen peroxide was consumed, after which, the system reached net radiolytic suppression.

A replicate experiment was conducted and left to run beyond the attainment of net radiolytic suppression; the results of this experiment are displayed in Figure 4-5.

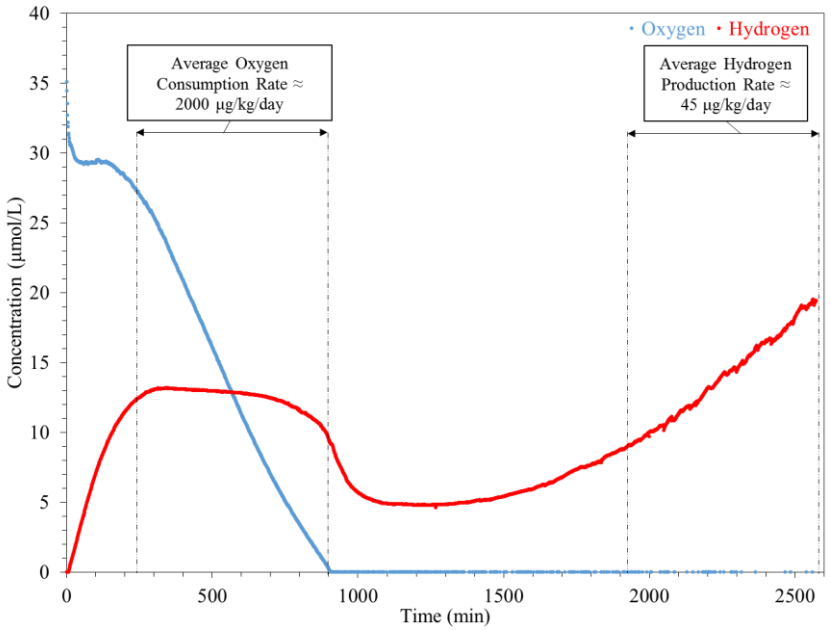


Figure 4-5: Synergistic Effects between the Radiation Chemistry of Water and Corrosion of Fresh Carbon Steel with Hydrogen Evolution

The test section was put into the radiation field at time zero (t = 0 min), after which the same behavior was observed. The average oxygen consumption rate was about 2000 µg/kg/day, which is slightly larger than the 1900 µg/kg/day rate observed in the results displayed in Figure 4-4. It is approximately double the net oxygen consumption rate observed in corrosion-only experiments. These tests suggest that oxidant consumption from corrosion processes on fresh carbon steel will dominate, and overcome the production

rate from the net radiolytic breakdown of water, placing the system into a net radiolytic suppression.

Once all oxygen was removed, hydrogen generation, as a result of corrosion, began at approximately 1400 min. The average hydrogen production rate was approximately 45 μg/kg/day (22.5 μmol/L/day), which is approximately double the rate observed outside of the radiation field. The hydrogen production outside of the radiation field appeared to occur at a slowing rate whereas in the radiation field it appeared to occur at a slightly increasing rate. This suggests that the radiation chemistry may also affect the hydrogen production mechanism from corrosion; though the radiolytically produced molecular species' concentrations are negligible under net suppression, radical species concentrations (e.g. ·H, ·OH) are at a maximum. These radical species could indirectly affect corrosion processes through reactions with dissolved iron species.

4.3.2 Loop Contamination and Acid Washing

In preliminary stages of the project it was found that experiments subsequent to irradiated-corrosion tests displayed a significant slowing of the oxygen consumption rate, as shown in Figure 4-6. Many magnetite deposits were found throughout the system and the slowing consumption rate was attributed to some form of iron contamination. Following several attempts at procedures targeted at remedial action, it was found that rinsing the system with acidic water at a pH of approximately 1 (adjusted w/ H_2SO_4), prior to each test, lead to a reversion to the initial behavior observed. The acidic rinsing process was always followed with several neutral DI water rinses, and an alkaline water rinse, to ensure no acid was

carried over to the subsequent experiments. The system pH and conductivity was regularly monitored through the process to ensure this.

The oxygen consumption rates at the beginning of the project in a fresh, new system were at the highest observed, however, the oxygen consumption rates following acid washes appeared to remain relatively consistent. Although the magnitude of consumption from initial experiments was not achieved again, the radiation-corrosion experiments consistently remained at approximately double the rate observed in corrosion-only tests following acid washes.

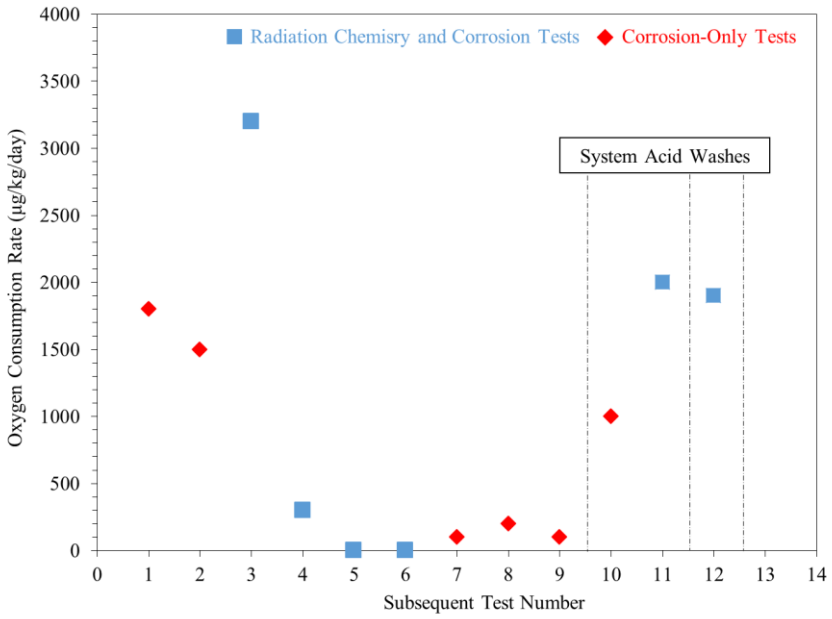


Figure 4-6: Loop Contamination and Subsequent Acid Washes

4.3.3 In-situ Aging Effects on Carbon Steel Corrosion under Irradiated Conditions

In an attempt to age fresh steel balls in the system, and simulate the effect of slowing oxygen consumption that occurred in the ESC systems of many CANDU reactors, an extended experiment was carried out over the course of several weeks. The experiment began with the insertion of fresh carbon steel balls in the irradiated test section, just as in the experiments previously discussed, however, for this experiment, the system was periodically dosed with hydrogen peroxide to maintain oxidizing conditions (i.e. net radiolysis). The goal was to oxidize the carbon steel surfaces to the point whereby oxidant production from radiolysis overcame consumption from corrosion.

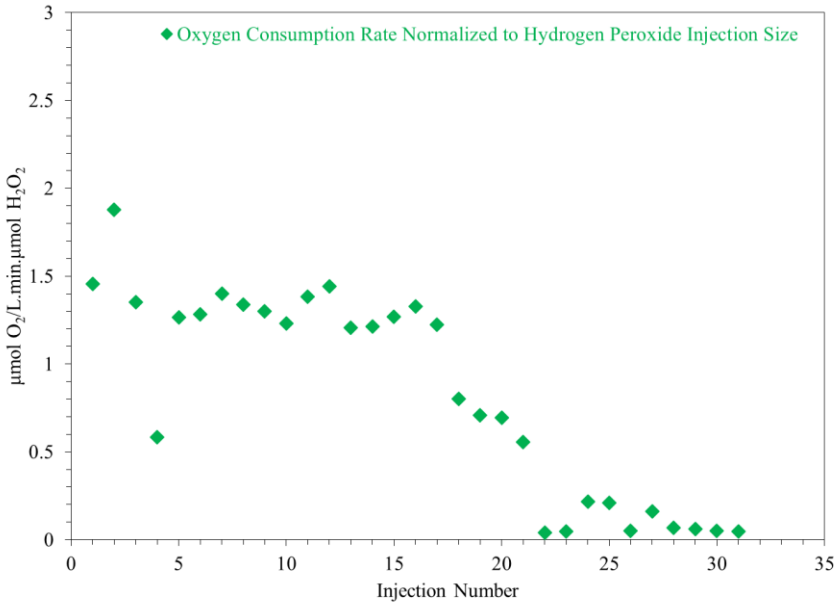


Figure 4-7: Slowing Oxygen Consumption Rates Following H_2O_2 Injections

Hydrogen peroxide was injected into the system several times at varying quantities before a slowing oxygen consumption rate was observed. Once the oxygen consumption rate

began to slow, each subsequent injection lead to a measurably slower rate, as shown in Figure 4-7. Figure 4-8 displays an excerpt from the test showing three consecutive 20 µL injections of 30 wt.% H_2O_2, each followed by sequentially slowing oxygen consumption rates. These are likely indicative of steel passivation due to the build-up of corrosion products on the surfaces.

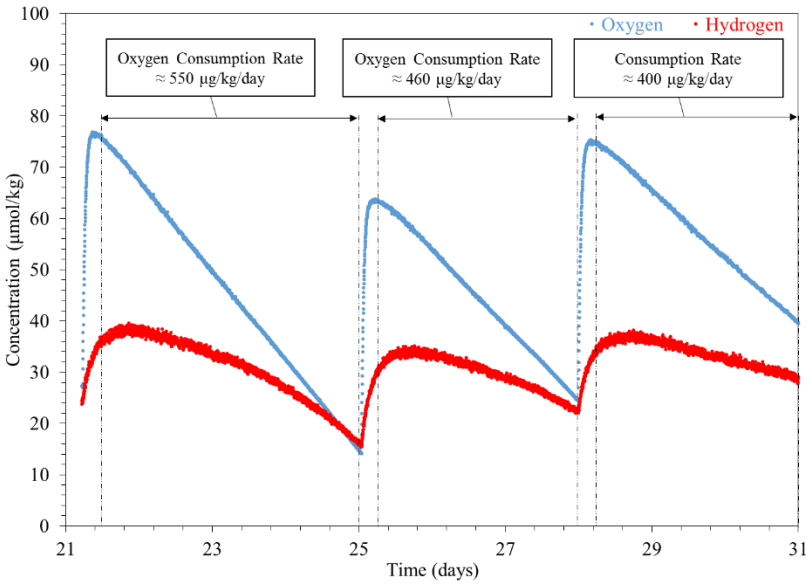


Figure 4-8: Varying Oxygen Consumption Rates Through Continual Oxidant Addition

Figure 4-9 displays a final 20 µL injection of 30 wt% H_2O_2, after which the kinetics associated with net radiolysis overcame those from corrosion. To reach this condition, a total of 9.31 mmol of H_2O_2 was injected into the system throughout the course of the experiment.

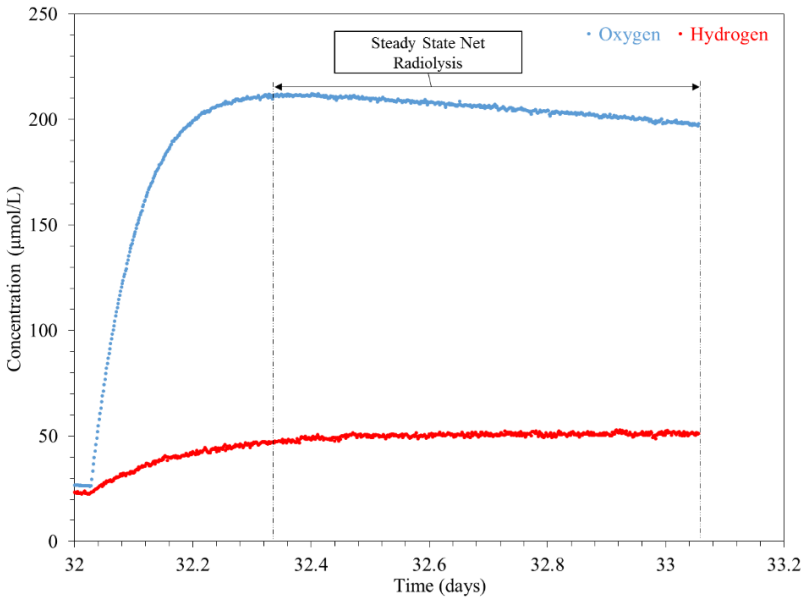


Figure 4-9: Steady State Net Radiolysis Following Several Hydrogen Peroxide Additions

Following the experiment, a sample of the carbon steel balls were analysed using Scanning Electron Microscopy (SEM) and Energy Dispersive X-ray Spectroscopy (EDS) in the Microscopy and Microanalysis Facility at the University of New Brunswick. The secondary electron images displayed in Figure 4-10 show an overview of a steel ball sample and a close-up of the oxide which has grown upon it. Though it is not completely uniform, there seems to be an oxide layer completely covering the surface of the balls at varying thicknesses. The ball surfaces in sample were analysed using EDS to gather information regarding the surface composition. Results from two randomly chosen locations on the ball surfaces are displayed in Table 4-1.

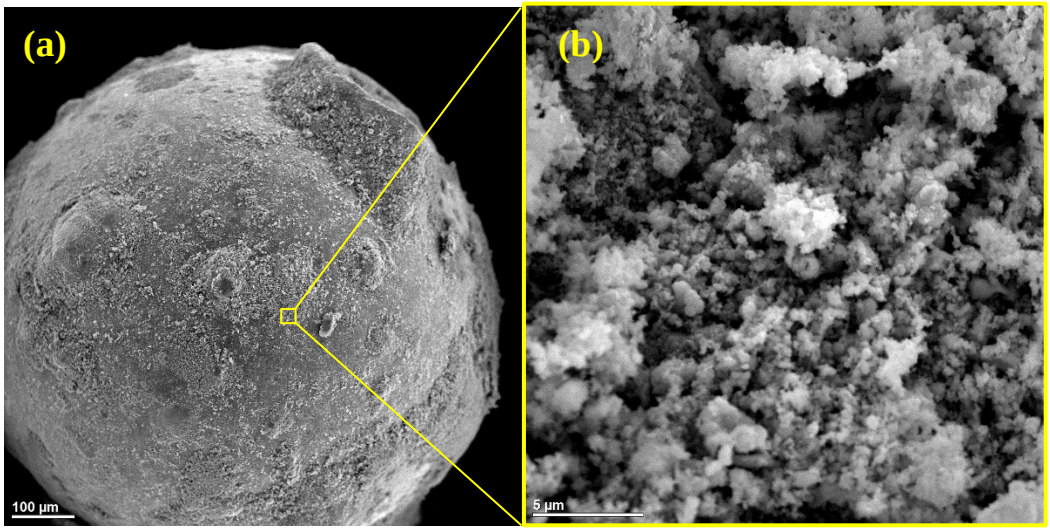


Figure 4-10: SEM Images of CS Balls Used in Irradiated Loop Experiments

Table 4-1: Surface Composition Results from EDS Analysis

Element		O	Fe	Fe:O
Ball 1	**(Atomic %)**	20.86	13.81	0.66
Ball 2	**(Atomic %)**	24.4	11.39	0.5

On "Ball 1" the atomic ratio of iron to oxygen (Fe:O) is approximately 0.66, which corresponds to about a 2:3 ratio between iron and oxygen. This suggests that the predominant oxide present in this particular location is an iron (III) oxide (Fe_2O_3), which is expected given the highly oxidizing conditions present under net radiolysis and the high levels of hydrogen peroxide present from the injections. Analyses were conducted in a variety of surface locations on several different balls, all of which rendered slightly

different iron to oxygen ratios. For example, on “Ball 2” the iron to oxygen ratio is approximately 0.5, which may be indicative of iron hydroxides such as lepidocrocite (γ-FeOOH). Given that the ratios of iron to oxygen vary across the surfaces of the steel, this suggests that there is a mixture of oxides present.

For comparison, SEM and EDS analyses were carried out on fresh carbon steel balls. A secondary electron image of a fresh carbon steel ball is displayed in Figure 4-11. The surface of the fresh ball is relatively smooth and displays no notable oxide build up. This is further demonstrated by the results from EDS analysis of the surface, which are displayed in Table 4-2. The iron to oxygen ratios are quite high, which are indicative of very little oxide on the steel surfaces.

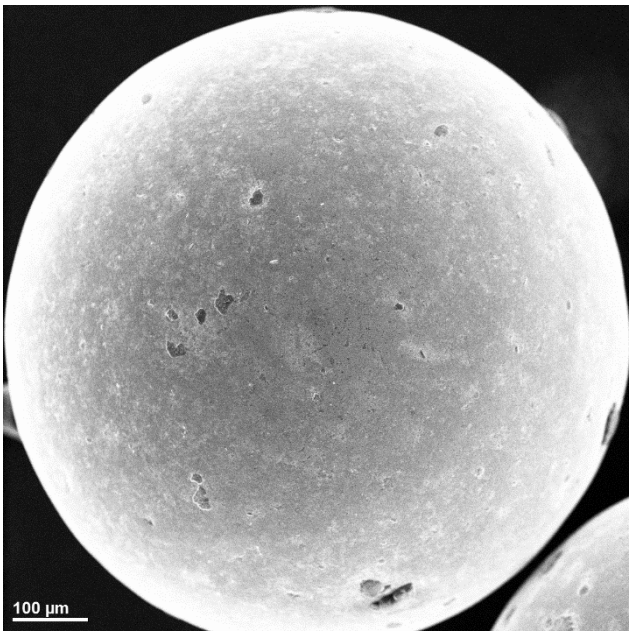


Figure 4-11: SEM Secondary Electron Image of Fresh Carbon Steel Ball

Table 4-2: EDS Analysis Results of Fresh Carbon Steel Balls

Element		O	Fe	Fe:O
Ball 1	**(Atomic %)**	9.83	81.62	8.30
Ball 2	**(Atomic %)**	10.98	80.7	7.35

4.3.4 Corrosion of Autoclave Aged Carbon Steel

In order to observe differences in behavior between fresh and aged carbon steel balls, samples of balls were aged in an autoclave under oxidizing and reducing conditions prior to their insertion into the test section, as described in Section 3.8.

Two experiments were carried out in the radiation field, with balls aged under both conditions inserted into the test section. Figure 4-12 displays an overlay of the oxygen consumption behavior of fresh balls, balls aged under reducing conditions, and balls aged under oxidizing conditions.

The oxygen consumption rate of balls aged under reducing conditions is comparable to the removal rate of fresh carbon steel, but significantly higher than those aged under air saturated conditions. The average oxygen consumption rate from each experiment is displayed in the Table 4-3. This suggests that carbon steel balls aged under reducing conditions have a much higher oxygen removal capability than those aged under oxidizing conditions and that the oxides formed are less protective than those formed under oxidizing conditions.

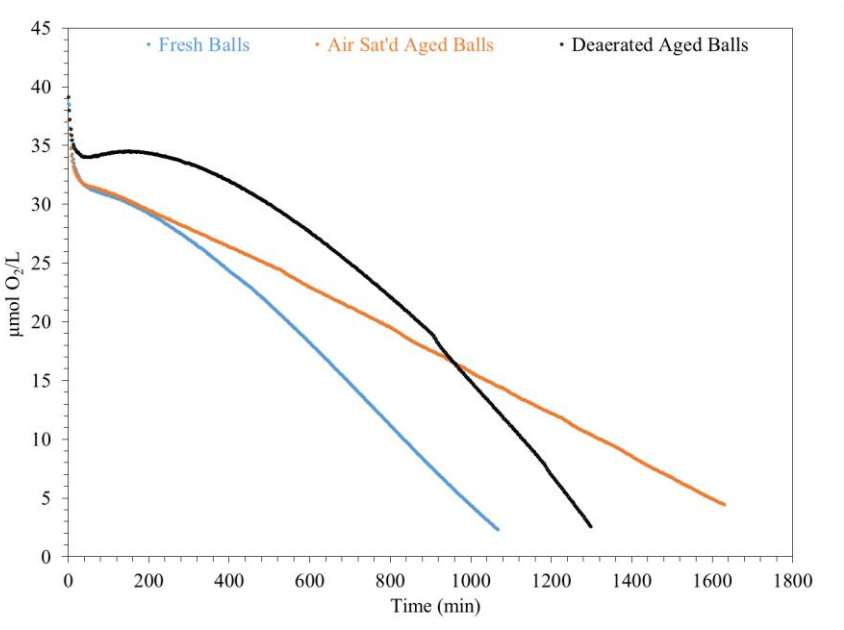


Figure 4-12: Comparison of Fresh and Aged Balls

Table 4-3: Oxygen Consumption Rate Comparison between Fresh and Aged Balls

Starting Ball Conditions	Average Oxygen Consumption Rate (µg/kg/day)
Fresh Balls	1600
Balls Aged in De-aerated Environment	1400
Balls Aged in Air Saturated Environment	830

SEM and EDS were used to analyse the surface of the balls after being aged in the autoclave. The secondary electron images displayed in Figure 4-13 are representative of the surface characterisation on the balls aged under deaerated conditions (Figure (a)) and air saturated conditions (Figure (b)). There is an oxide build-up on the ball surfaces in both cases, however, the oxide present on balls aged under aerated conditions seems to be more prominent, more compact and less porous than those aged under de-aerated conditions.

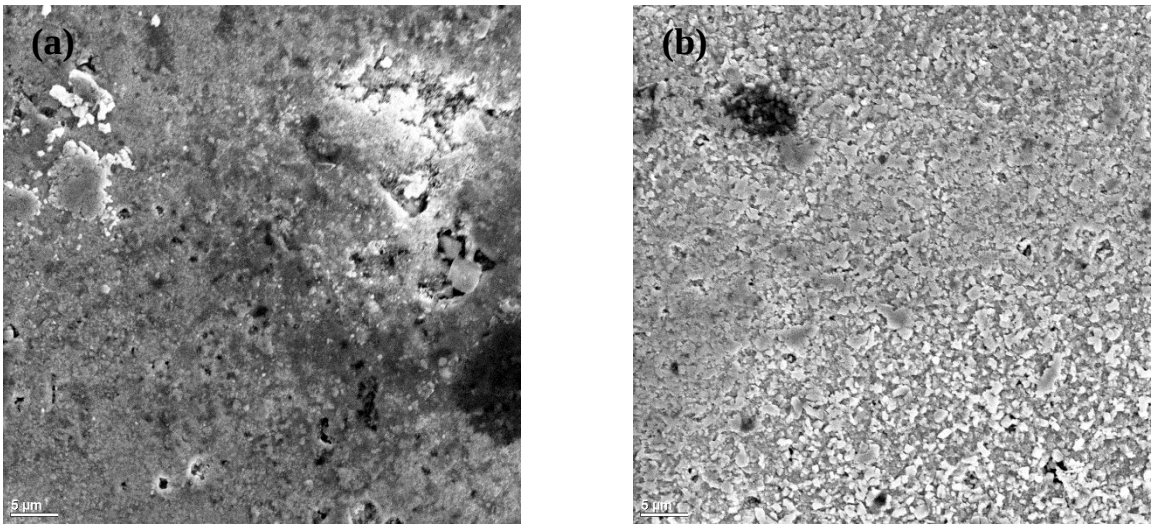


Figure 4-13: SEM Images of CS Balls Aged under De-aerated (a) and Aerated (b) Conditions

Table 4-4: Surface Composition Results from EDS Analysis

Ball Condition	Randomly Chosen Site	O (at.%)	Fe (at.%)	Fe:O	Average Fe:O
Balls Aged Under De-aerated Conditions	1	31.49	63.75	2.02	1.76
	2	36.23	56.29	1.55	
	3	34.46	59.41	1.72	
Balls Aged Under Air Saturated Conditions	1	38.4	58.45	1.52	1.4
	2	42.69	54.48	1.28	
	3	39.21	54.81	1.40	

Three randomly chosen surface locations on each ball sample were analyzed using EDS, and the results are displayed in Table 4-4. In all cases the atomic ratio between iron and oxygen (Fe:O) is greater than 1. Since iron oxides generally have an atomic ratio of less than 1, this suggests that the oxide film is very thin (< 1 μm) and that there is considerable interference from the underlying steel. It can be noted that the balls aged under air-saturated conditions have ratios averaging lower than those aged under de-aerated conditions. This suggests that there is more iron oxide present on the balls aged in an air saturated

environment, which could promote passivation; this is consistent with the oxygen consumption capacities shown in Figure 4-12.

The surfaces of the in-loop aged balls displayed much more significant oxide presence, however, they were aged under oxidizing conditions and exhibited minimal oxygen removal capability at the end of the test. Therefore, results from the in-loop aged ball tests can be said to be consistent with the results from the autoclave aged ball tests.

4.4 Oxygen Scavenging by Chemical Addition

4.4.1 Oxygen Scavenging by Hydrazine Injection

The oxygen scavenging ability of hydrazine was confirmed, with the results displayed in Figure 4-14. The experiment began just as the radiation chemistry tests, whereby no carbon steel balls were inserted into the test section. Upon irradiation of the test section, oxygen was consumed and hydrogen produced, after which both approached a steady state concentration as dictated by the radiolysis reactions. At approximately 1100 min, 1.5 μL of 98 wt. % hydrazine monohydrate ($N_2H_4 \cdot H_2O$) was injected, which resulted in an immediate consumption of oxygen. Oxygen was consumed from 32 μmol/L to a low point of about 15 μmol/L, after which it rebounded to a steady state concentration of approximately 18 μmol/L. The hydrogen concentration decreased from 22.4 μmol/L to 20.7 μmol/L. This injection was followed by two subsequent injections until all oxygen was removed and a net suppression was achieved. The rebound in oxygen concentration following the large initial decrease can be attributed to two factors. One of which is the

termination step in the chain reaction of hydrazine whereby the disproportionation of O_2^- / HO_2 leads to the production of hydrogen peroxide and oxygen, as discussed in Section 2.3.1. The other is the net conversion of hydrogen peroxide to oxygen as the system attains a new steady-state.

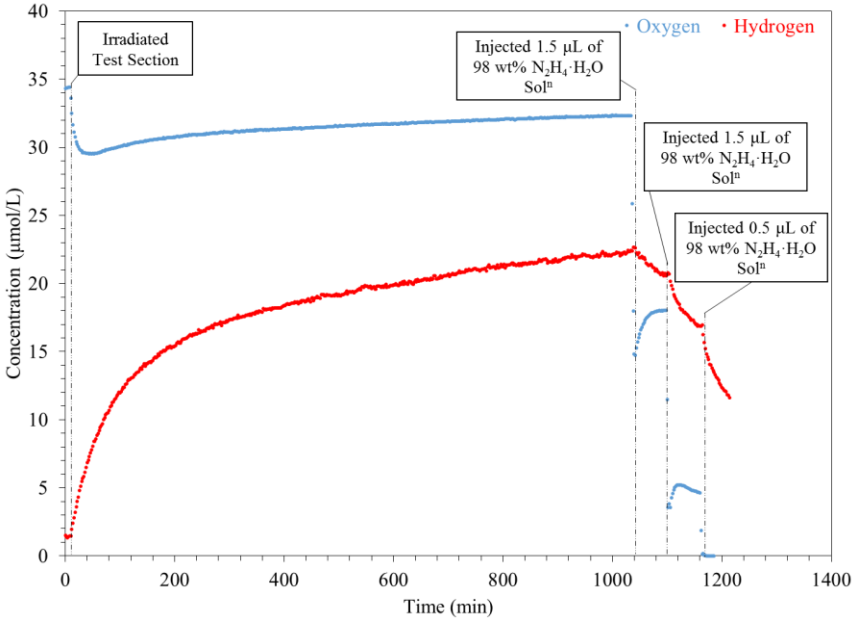


Figure 4-14: Irradiated Oxygen Scavenging by Hydrazine

Based on each injection, the net removal of oxygen by hydrazine addition was approximately 1 mole of oxygen per 2 moles of hydrazine. The net removal of hydrogen increased following each subsequent injection; Table 4-5 displays these results. The increase in hydrogen removal following each subsequent injection was likely due to the decreasing oxygen concentration. Initially, oxygen was in stoichiometric excess of hydrogen, therefore, it is likely that there was also a significant amount of hydrogen peroxide present. Following the hydrazine injections, oxygen was removed and some

hydrogen peroxide would have effectively converted to oxygen as the system approached a new steady-state. Because there was, initially, a significant amount of H_2O_2 present, its removal to produce oxygen would have minimal effect on its preferential scavenging of the hydroxyl radical over hydrogen. However, as the concentration of hydrogen peroxide fell due to its conversion to oxygen following each subsequent hydrazine injection, the reaction between hydrogen and the hydroxyl radical would have become more prominent, thereby increasing the overall removal of hydrogen when oxygen concentrations were lower.

Table 4-5: Oxygen and Hydrogen Consumption from Hydrazine Injections

Injection	Hydrazine Injected (µmole/L)	Net Oxygen Removed (µmole/L)	$\frac{\Delta[O_2]}{\Delta[N_2H_4]}$	Net Hydrogen Removed (µmole/L)	$\frac{\Delta[H_2]}{\Delta[N_2H_4]}$
1	25.25	14.3	0.57	1.65	0.065
2	25.25	13.4	0.53	3.75	0.15
3	8.42	4.6	0.55	5.45	0.65

The stoichiometry specified by the overall reaction between hydrazine and oxygen states a 1:1 molar ratio, however, these results only display the net behavior of oxygen in the system. Since other reactions within the system produce oxygen, some of the oxygen consumed by hydrazine would have been masked. An even larger contributor to the less than expected oxygen removal is likely the presence of nitrite ions within the system.

Nitrite ions will compete with hydrazine for reaction with the hydroxyl radical, as shown in reaction (4-1).

$$\cdot OH + NO_2^- \rightarrow OH^- + \cdot NO_2 \qquad (4\text{-}1)$$

Nitrites/nitrates are likely present within the loop as nitrogen is used as a sparge gas. In irradiated systems, dissolved nitrogen will react with oxygen to form nitrites/nitrates, which can inhibit the oxygen removal efficiency of oxygen scavengers such as hydrazine and methanol, which rely on their reaction with the hydroxyl radical to induce the oxygen removal mechanisms discussed in Sections 2.3.1 and 2.3.2 [9].

4.4.2 Oxygen Scavenging by Methanol Injection

The oxygen scavenging ability of methanol was subsequently studied, with the results displayed in Figure 4-15.

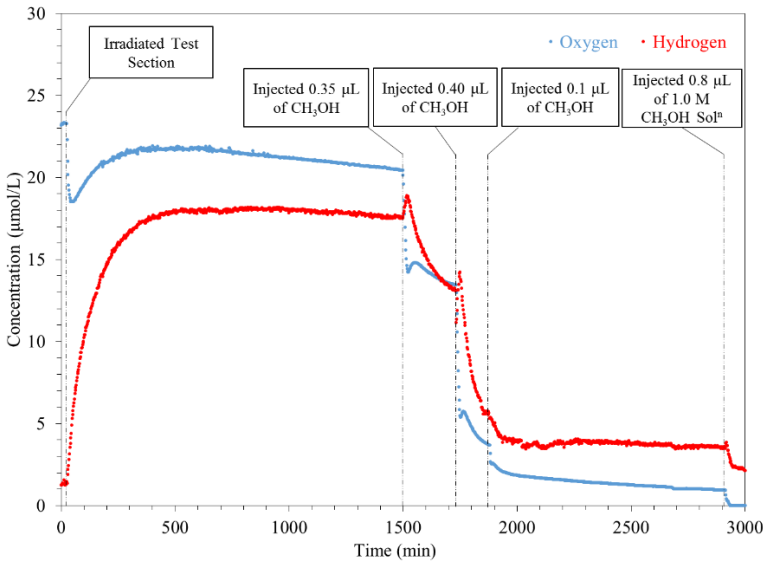


Figure 4-15: Irradiated Oxygen Scavenging by Methanol

The experiment began with the irradiation of the test section, followed by subsequent injections of methanol until all oxygen was depleted. There are two steps of oxygen removal from a methanol addition. Immediately upon injection, there is a rapid consumption of oxygen. This is attributed to hydrogen production from one of the mechanism's initiation reactions; methanol reacts with the hydrogen atom, as shown in reaction (4-12), to produce molecular hydrogen and hydroxymethyl radicals ($\cdot CH_2OH$). The hydrogen produced in this reaction leads to the large initial oxygen decrease. Hydroxymethyl radicals also assist in oxygen scavenging and are further produced by reactions between methanol and the hydroxyl radical, as shown in reaction (4-13) [5].

$$\cdot H + CH_3OH \rightarrow CH_2OH + H_2 \quad (4\text{-}2)$$

$$\cdot OH + CH_3OH \rightarrow CH_2OH + H_2O \quad (4\text{-}3)$$

There is a competition between the reaction of the hydroxymethyl radical with itself and oxygen, as shown in reactions (4-14) - (4-16) [5].

$$5O_2 + 4CH_2OH \rightarrow Products \rightarrow 4CO_2 + 6H_2O \quad (4\text{-}4)$$

$$\cdot CH_2OH + \cdot CH_2OH \rightarrow HCHO + CH_3OH \quad (4\text{-}5)$$

$$\cdot CH_2OH + \cdot CH_2OH \rightarrow H_2COHC(OH)H_2 \quad (4\text{-}6)$$

When the hydroxymethyl radical reacts with itself, ethylene glycol ($H_2COHC(OH)H_2$) and/or formaldehyde (HCHO) will be formed, both of which are slightly longer lived than other intermediate products, but are still oxidized/reduced through a series of intermediate

reactions ending with carbon dioxide and water [5]. Oxygen is consumed throughout this process, which is responsible for the slower portion of oxygen removal following each injection.

Table 4-6: Oxygen Consumption from Methanol Injections

Injection	Methanol Injected (μmole/L)	Net Oxygen Removed (μmole/L)	$\frac{\Delta[O_2]}{\Delta[CH_3OH]}$	Net Hydrogen Removed (μmole/L)	$\frac{\Delta[H_2]}{\Delta[CH_3OH]}$
1	7.21	7.19	1.00	4.4	0.61
2	8.24	9.55	1.16	7.85	0.95
3	2.06	2.76	1.34	0.78	0.78
4	0.8	0.94	1.17	1.875	1.88

Methanol is capable of efficiently removing oxygen with an average ratio of oxygen removed to methanol injected of approximately 1.2. This is slightly lower than the expected stoichiometry of 1.5 O_2 : 1 MeOH, however, if nitrites were present within the system they could also compete with this reaction mechanism, as they do with hydrazine.

Hydrogen was also readily removed with an increasing removal ratio with each subsequent injection, just as observed with hydrazine. However, the hydrogen removal ratio decreased from injection 2 to injection 3, albeit, hydrogen was still decreasing when injection 4 was made, and the full effect of injection 3 may not have been observed.

5. Discussion

5.1 Kinetic Model of Radiation Chemistry and Corrosion

A model was formulated in an attempt to mimic the behavior observed in the experimental trials. A series of differential equations encompassing the rate constants and concentration dependences of the water radiolysis reaction set were implemented into Polymath®. The model is described in detail in Appendix E.

Figure 5-1 displays results from a radiation chemistry experiment (Plot (A)) and a model simulation (Plot (B)) under similar starting conditions.

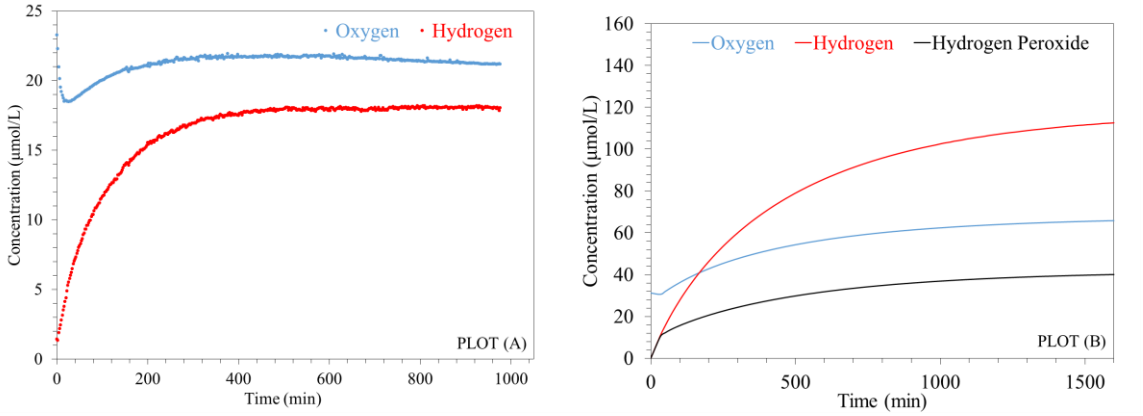


Figure 5-1: Net Radiolysis Experimental Results (PLOT (A)) vs. Model Simulation (PLOT (B))

The model data simulates the radiation chemistry of water with a dose rate of approximately 500 Gy/hr, and an initial oxygen concentration of 1 mg/kg (31.25 µmole/L). As expected under net radiolysis conditions, the concentrations of hydrogen and hydrogen peroxide immediately increase upon irradiation (at t = 0 min) to steady state values. Oxygen

initially decreases as hydrogen peroxide is formed, and then increases to its steady state concentration once hydrogen peroxide is formed in sufficient quantity.

The model over estimates the steady state concentrations of radiolytically produced molecular species when compared to experimental data. This is attributed to interactions between radiolytically produced hydrogen peroxide and steel surfaces within the loop. In the real system, hydrogen peroxide is consumed on the stainless steel surfaces, and it is never sufficiently formed to allow the oxygen concentration significantly rise following its initial decline. A secondary cause of the higher than expected dissolved gas concentrations from the model can attributed to the model's assumption that there is uniform irradiation of the entire water system; in the real system, this is not the case. Some of the system is outside of the radiation field, which would decrease the steady state concentrations of radiolytically produced species.

In an attempt to replicate the behavior of carbon steel corrosion, an oxygen consumption term was incorporated into the model. The integral method was applied to experimental data from early corrosion experiments (Figure 4-2), in which the oxygen consumption rate displayed a pseudo-zeroth order dependence at higher oxygen concentrations, and a ½ order at lower oxygen concentrations ($\lesssim$2.5μmol/L). Rate constants for high and low oxygen concentrations were extracted from corrosion-only data (shown in Table 5-1), and implemented into the model. To check the validity of this implementation, the model was tested with no radiation field applied. The model data and experimental results are shown together in Figure 5-2.

Table 5-1: Rate Constants at High and Low Oxygen Concentrations

Oxygen Concentration	Rate Constant	Rate Constant Units
<2.5 µmol/L	$1.455x10^{-7}$	$mol^{0.5}/L^{0.5}.sec$
>2.5 µmol/L	$3.864x10^{-10}$	mol/L.sec

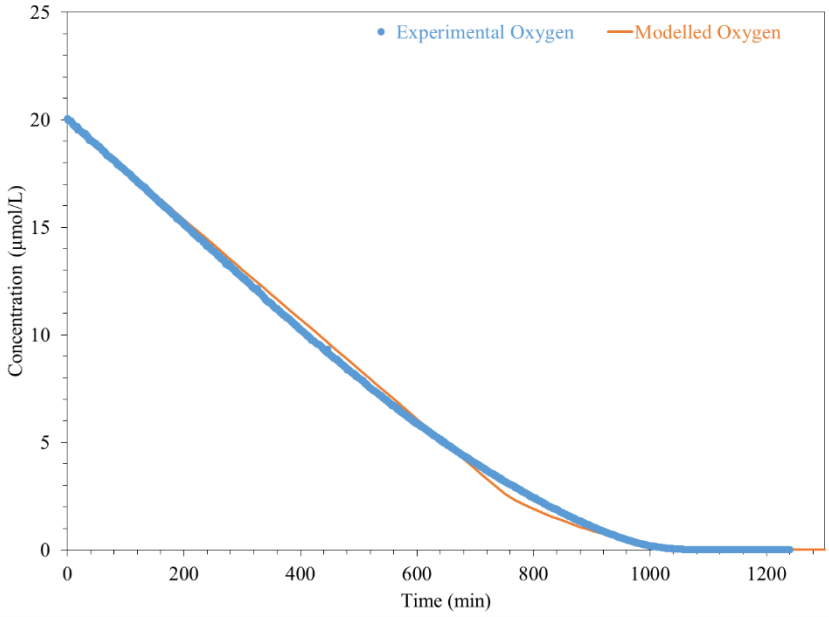


Figure 5-2: Comparison of Modelled and Experimental Corrosion Effects

With the rate constants implemented, a model simulation was performed with the effects of radiation chemistry applied; the experimental data (PLOT (A)) is compared against the modelled data (PLOT (B)) in Figure 5-3. The overall behavior of the dissolved gasses in the experimental tests line up well with the model simulation, however, the concentrations are overestimated by the model. As previously mentioned, this overestimate of dissolved gas concentrations can be attributed to surface interactions on the stainless steel loop

components and the assumption made by the model that there is uniform irradiation over the entire system.

As in the experimental tests, the model data exhibits a decrease in oxygen concentration when irradiated (at t = 0 min), followed by a rebound in the oxygen concentration upon sufficient formation of hydrogen peroxide. The radiolytic oxidant production rate then falls below the consumption rate from corrosion processes and there is a net decline in the concentrations of oxidants until net radiolytic suppression is achieved.

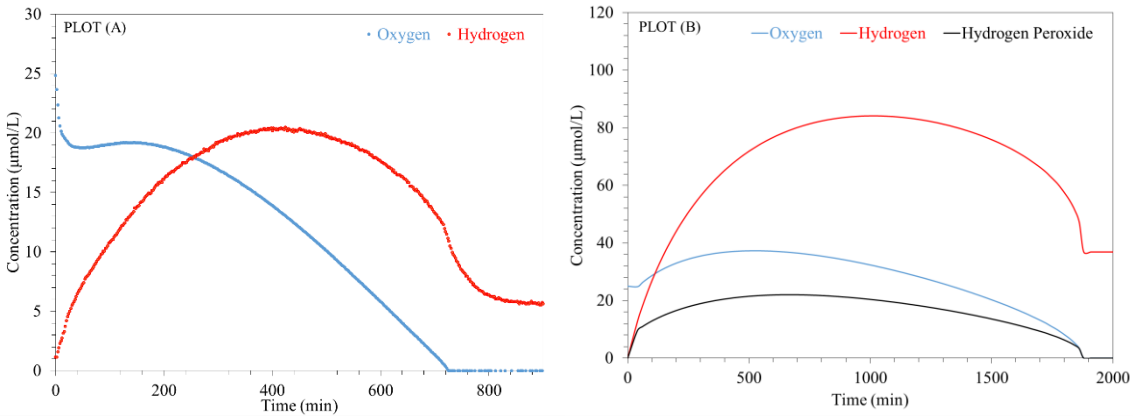


Figure 5-3: Radiation Chemistry and Corrosion Experimental Data (PLOT (A)) vs. Modelled Data (PLOT (B))

Though the general behavior of the radiolytically produced species appears to represent the system quite well, the net oxygen consumption rate estimated by the model is lower than in experimental results. The average estimated oxygen consumption rate is approximately $1100 \mu g O_2 \cdot L^{-1} \cdot day^{-1}$, while experimental results render a value closer to $2000 \mu g O_2 \cdot L^{-1} \cdot day^{-1}$. This is attributed to a change in the corrosion mechanism, as predicted

by previous studies; hydrogen peroxide has been shown to be the primary radiolytically produced species contributing to corrosion processes on carbon steel [26]. A sink of hydrogen peroxide would present very similar behavior to that displayed in Figure 5-3. The shift in corrosion mechanism may result in higher corrosion rates, and hence a higher net consumption of oxygen as observed in the experimental results.

5.2 Relevance of Results to ESC System at PLNGS

5.2.1 Suppression of Net Radiolysis by Corrosion Processes in the ESC System

The results from this study demonstrate that corrosion processes can readily suppress the net radiolytic breakdown of water by removing any existing or radiolytically produced oxidants within a system. However, over time the corrosion processes will slow due to passivation, and the system will shift to net radiolysis conditions. When PLNGS began operations in 1983, the system's carbon steel was fresh, and readily capable of removing oxygen, and producing hydrogen. Because the system initially operated with low dissolved oxygen (i.e. reducing conditions), it is likely that hydrogen was readily produced by corrosion processes, which promoted net radiolytic suppression, and offset any oxygen ingress. As hydrogen evolution continued, it is probable that the carbon steel became coated in lower oxidation state iron oxides which stifled proton reduction, thereby slowing hydrogen evolution. The lower oxidation state iron oxides were still likely capable of removing oxygen by conversion to higher iron oxidation states, therefore net radiolytic suppression would still have been maintained. As time progressed, and more of the steel surfaces were shifted to higher iron oxidation states, oxygen consumption would have

slowed below the oxygen ingress rate from the make-up water and net radiolysis would have been established. This lead to a continual build-up of radiolytically produced H_2, O_2, and H_2O_2, which has been observed in the ESC systems of several plants [1]. The issue is currently controlled by hydrazine injections, which scavenge oxygen, and place the system into a net radiolytic suppression.

5.2.2 Oxygen Scavenging in the ESC System at PLNGS

As discussed in previous sections, handling restrictions on hydrazine are stringent and have invoked exploration into alternatives. This study sought to explore the comparative abilities of hydrazine and methanol as oxygen scavengers under conditions comparable to those in the ESC System of CANDU® reactors.

Based on the findings in this study, methanol, from a stoichiometry perspective, appears to have a comparable, and possibly better, oxygen scavenging ability than hydrazine. However, hydrazine exhibits a much faster oxygen removal rate than methanol. If the use of methanol is scaled up to plant application, some problems would be encountered, particularly with ion exchange resins. Methanol removes oxygen at a much slower rate than hydrazine, as shown in Figure 5-4, which displays the dissolved oxygen behavior following injections of each scavenger.

The methanol consumption mechanism is much slower because it relies on many chemical steps whereby intermediates are oxidized to carbon dioxide. However, hydrazine's consumption mechanism is a chain reaction which can remove oxygen at a much faster

rate, as each initiation reaction results in the removal of several oxygen molecules or radicals.

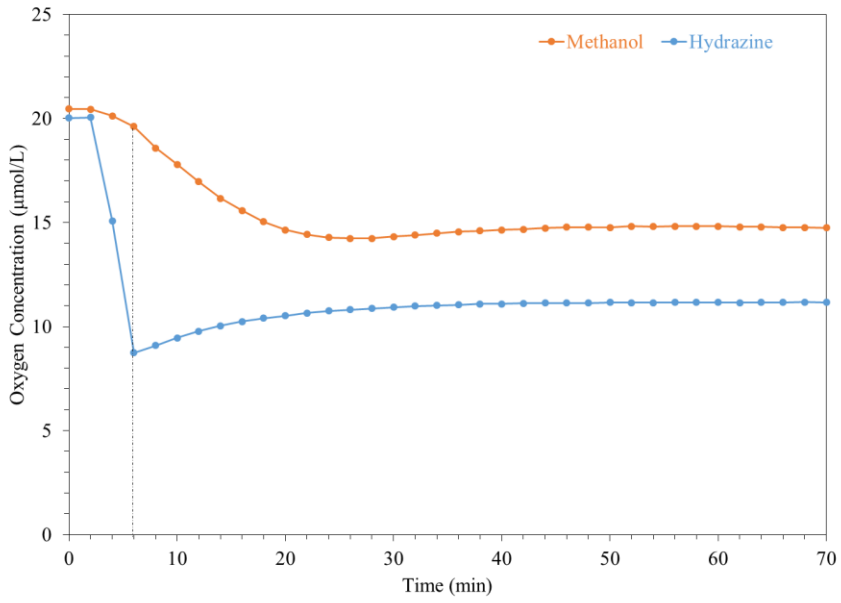


Figure 5-4: Comparison of Hydrazine and Methanol Oxygen Scavenging

Following the injection of hydrazine, the oxygen concentration falls from approximately 20 µmol/L to 9 µmol/L by the 6 minute mark, at which point the methanol injection has only decreased the oxygen concentration by about 1 µmol/L. Therefore, intermediates from methanol radiolysis could be present, up to approximately 10 times longer than those of hydrazine. This could be consequential for the ion exchange resin; because the intermediate species from methanol radiolysis are much longer lived than those from hydrazine, more of the intermediate species could be taken up by the IX resins, thereby reducing oxygen scavenging ability and ion exchange resin life.

A further concern of methanol application in plants is the carbon dioxide formed. Upon formation of carbon dioxide, it will react with water to form carbonic acid, as discussed in Section 2.3.2. Carbonic acid is a weak acid, however, it could still present issues for the system pH and life span of the ion exchange resin. In order to gain insight into the effects of carbon dioxide production from methanol injections on end shield cooling system chemistry, a simple equilibrium model was produced (Appendix D).

Figure 5-5 displays the equilibrium conditions following methanol injections, as predicted by the model. Because the end shield cooling system's pH is maintained using Li-saturated ion exchange (IX) resin, all carbonates/bicarbonates formed will be removed, thereby making Figure 5-5 only valid after a break on carbonates is experienced by the IX resin. However, the life expectancy of the resin can be estimated based on the current action limit applied to oxygen concentration in the system.

Currently at PLNGS, the system is dosed with 35 wt% hydrazine in batches of 500 mL, when an action limit of 0.1 mgO_2/kg is reached. The stoichiometric amount of methanol required to match this is approximately 150 mL of 100 wt% methanol. Based on this injection quantity, 6.5 μmol/L of carbon dioxide would be produced. This concentration can be implemented into the model as the total carbon content, and the proportions of carbonate and bicarbonate that would be removed on the system's IX resin can be estimated.

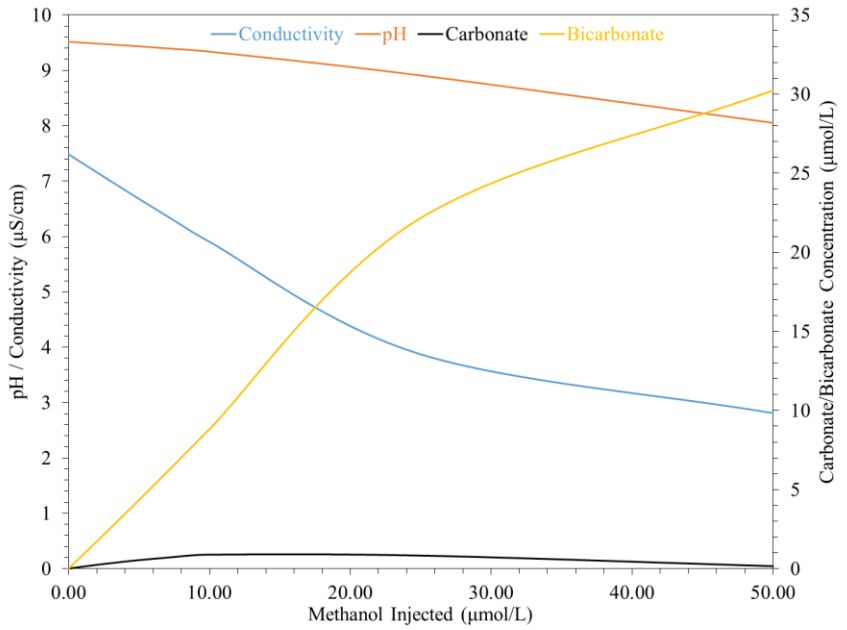


Figure 5-5: Model Results Presenting Effects of MeOH Injections on System pH and Conductivity Following IX Break on Carbonates

The IX column in the ESC system at PLNGS contains Purolite NRW-37 LiLC resin [27]. The minimum capacities of the anion and cation exchange resins are 1.0equiv/L and 1.8equiv/L, respectively. Given that the mixed bed cation to anion equivalents ratio is 1.05, and the IX column dimension is 0.2 m^3, the total anion and cation capacities for the system are 125.2 equivalents and 131.5 equivalents, respectively. The total proportions of carbonate and bicarbonate produced by a single methanol injection, as estimated by the model are 0.69 µmol/L and 5.8 µmol/L, respectively. This would equate to a 3.3 % uptake of the IX resin capacity for each methanol injection. The current addition frequency is approximately bi-weekly, therefore, in one year, 86% of the IX resin capacity would be saturated with carbonate solely as a result of methanol injections.

Presently, the IX resin has an approximate lifetime of one year, without significant uptake of carbonate. When including the additional uptake expected on the resin due to methanol injections, the time to resin replacement (indicated by breakthrough of carbonate) is about 6.5 months. However, carbonic acid is a weak acid and the system may be able to operate with a carbonate saturated IX resin for a period. The model predicts that upon saturation, three additional injections of methanol could be made before the system pH falls below 9.0. Based on these findings, methanol is a potential candidate for oxygen scavenging in the end shield cooling systems of CANDU® reactors, but with a decreased IX resin life.

Further investigations into the effects of methanol injections on the system's IX resin should be performed prior to considering plant scale application. This study exhibited the oxygen scavenging ability of methanol to be comparable to that of hydrazine. However, methanol radiolysis relies on many chemical steps, leaving intermediate products in the system for longer periods of time. This may result in uptake of intermediates on the IX resin, thereby reducing oxygen scavenging capabilities and IX resin life expectancy. Furthermore, the model does not account for radiolysis products, which do interact with carbonates and bicarbonates, and could present variances in results. Further irradiated loop tests could be conducted with samples of the ESC system IX resin to validate the predictions discussed.

6. Conclusions and Recommendations

6.1 Conclusions

This study demonstrated that corrosion processes on fresh carbon steel will readily suppress the net radiolytic breakdown of water by removing oxidants and generating hydrogen. This suggests that corrosion of carbon steel system components are responsible for the net radiolytic suppression condition that is met, and sometimes maintained in the ESC systems of CANDU® reactors. Some plants, as they have aged, have had their ESC system chemistry shift to net radiolysis conditions. This shift is attributed to oxygen ingress and subsequent passivation of the system's carbon steel components. As oxygen enters the system, carbon steel surfaces will passivate from the build-up of oxides and the corrosion rate will slow. Once the oxygen consumption rate from corrosion falls below that necessary for maintaining net radiolytic suppression, a shift to net radiolysis will occur. Once the system reaches this condition, alternative mechanisms of maintaining net radiolytic suppression must be employed. All of this behavior was demonstrated in the tests performed, as was the effectiveness of hydrazine addition at restoring net radiolytic suppression. Currently, many CANDU® plants inject hydrazine into their ESC systems to act as an oxygen scavenger. Removing oxygen will consequently remove hydrogen and hydrogen peroxide, and, return the system to a net radiolytically suppressed state. However, strict handling measures on hydrazine invoked exploration into alternatives, thus, an analysis on the comparative oxygen scavenging abilities of methanol and hydrazine was performed. Studies of methanol as an oxygen scavenger for these systems

showed overall oxygen removal effectiveness, but came with the drawback of carbonate formation and pH depression. Carbonate uptake on the ESC system's IX resin was predicted to be about 3.3% IX capacity per injection. This translates to an IX resin life of approximately 6.5 months, indicated by a breakthrough of carbonate. Therefore, while methanol could be a potentially viable alternative to hydrazine for use in the ESC system of CANDU® reactors, pH control and IX resin usage would have to be further assessed prior to implementation.

6.2 Recommendations for Future Work

Although this study was able to prove that corrosion processes on carbon steel can readily suppress the net radiolytic break down of water, it is still not clear how corrosion potentials and corrosion rates change under varying system conditions. Corrosion rates were deduced from the consumption of oxygen and production of hydrogen, however, in an irradiated water system this assumption is not fully representative. The presence of radiolytically produced species can strongly affect the redox conditions of the system. Interactions between radical and dissolved iron species or the presence of hydrogen peroxide and its interaction with the steel surfaces will strongly affect corrosion processes. The implementation of an electrode system capable of measuring corrosion potentials and rates could solidify an understanding of the intricacies between corrosion and radiation chemistry. This study focused heavily on the effects of corrosion on radiation chemistry, however, electrochemical corrosion measurements could contribute significant insight into the effect of radiation chemistry on corrosion. Some constraints lie within the system

design, which could include the choice of reference electrode, as well as space limitations. Saturated calomel and Ag-AgCl electrodes are not optimal in irradiated systems, however, it has been demonstrated that Hg/HgO reference electrodes are fairly robust in irradiated environments [9]. Space limitations may also become a concern given the gamma cell chamber size; most of the irradiated space is already occupied by the glass radiation chemistry vessel, therefore, upon the implementation of an electrode system, the test section would require re-engineering.

It is recommended that further work is conducted into the investigation of methanol as an oxygen scavenger. Though it displayed overall oxygen removal effectiveness, the effects on the ESC system's ion exchange resin is not fully understood. The model simulation does not account for intermediate species that are produced as methanol is oxidized/reduced to carbon dioxide and water, which could result in lower than anticipated oxygen removal and, hence, resin life expectancy. Much could be learned from the implementation of an IX column containing the same resin employed in the ESC system into the flow loop. This would give a better understanding of how methanol injections would affect the system pH, conductivity and anticipated resin life.

7. References

[1] C. R. Stuart, G. A. Glowa, H. Searle, and D. G. Webb, “Hydrogen Production in the End Shield Cooling System.” CANDU Owners Group Inc., Sep-2005.

[2] C. R. Stuart, “Hydrazine Addition to the End Shield Cooling System - Recent Experience.” CANDU Owners Group Inc., Oct-2014.

[3] J. W. T. Spinks and R. J. Woods, Introduction to radiation chemistry, 3rd ed. Wiley, 1990.

[4] A. J. Elliot and C. R. Stuart, “Coolant Radiolysis Studies in the High Temperature, Fuelled U-2 Loop in the NRU Reactor,” Atomic Energy of Canada Ltd., Chalk River, ON, Canada, Research and Development 153-127160-440-003, Jun. 2008.

[5] A. J. Elliot, D. C. Ouellette, and C. R. Stuart, “Laboratory Studies of the Radiation Chemistry of Organic Material.” CANDU Owners Group Inc., Feb-1998.

[6] P. A. Yakabuskie, J. M. Joseph, P. Keech, G. A. Botton, D. Guzonas, and C. Wren, “Iron oxyhydroxide colloid formation by gamma-radiolysis,” Physical Chemistry Chemical Physics, vol. 13, pp. 7198–7206, Feb. 2011.

[7] S. Le Caër, “Water Radiolysis: Influence of Oxide Surfaces on H2 Production under Ionizing Radiation,” Water, vol. 3, no. 1, pp. 235–253, Dec. 2010.

[8] A. J. Elliot and D. M. Bartels, “The Reaction Set, Rate Constants and g-Values for the Simulation of the Radiolysis of Light Water over the Range 20’ to 350°C Based on Information Available in 2008.” AECL Ltd., Aug-2009.

[9] C. R. Stuart, “Radiation Chemistry Manual - Revision 2.” CANDU Owners Group Inc., Oct-2010.

[10] W. Cook and D. Lister, “Chemistry in CANDU Process Systems - Chapter 15,” in The Essential CANDU Textbook, UNENE, 2014.

[11] G. A. Glowa and J. R. Mitchell, “Experiments In Radiolytic Suppression - Part II.” CANDU Owners Group Inc., Apr-2012.

[12] W. Cook, “Corrosion Processes Course Notes.” University of New Brunswick, 2014.

[13] Salama Ibrahim. Corrosion Inhibitors in the Oilfield [Internet]. Version 1. isalama. 2011 May 17. Available from: https://isalama.wordpress.com/article/corrosion-inhibitors-in-the-oilfield-3uf3kbfllnswt-4/.

[14] V. Ashworth et al., “A SHORT INTRODUCTION TO CORROSION AND ITS CONTROL.” National Physics Laboratory.

[15] P. R. Roberge, Handbook of Corrosion Engineering. Hightstown, N.J.: McGraw-Hill, 2000.

[16] Penn State University, “Pourbaix Diagrams.” Chemistry - LibreTexts, 27-Sep-2015.

[17] W. Xu, K. Daub, X. Zhang, J.C. Wren, J.J. Noel, and J.C. Shoesmith, “Oxide formation and conversion on carbon steel in mildly basic solutions,” Electrochimica Acta, vol. 54, pp. 5727–5738, Feb. 2009.

[18] K. Daub, X. Zhang, J. J. Noel, and J. C. Wren, “Effects of gamma-radiation versus hydrogen peroxide on carbon steel corrosion,” Electrochimica Acta, vol. 55, pp. 2767–2776, 2010.

[19] G. V. Buxton and C. R. Stuart, “Radiation chemistry of aqueous solutions of hydrazine at elevated temperatures - Solutions containing oxygen,” J. Chem. Soc., Faraday Trans., vol. 93, pp. 1535–1538, 1997.

[20] J. Rabani, K.-R. Dina, and A. Henglein, “Pulse Radiolytic Investigations of OHCH2O2 Radicals,” The Journal of Physical Chemistry, vol. 78, no. 21, pp. 2089–2093, 1974.

[21] J. B. Riggs and N. M. Karim, Chemical and Bio-Process Control. Austin, Texas: Ferret Publishing, 2016.

[22] D. C. Hall, “Introduction to Scanning Electron Microscopy,” University of New Brunswick, 22-Mar-2017.

[23] D. C. Hall, “Analytical Scanning Electron Microscope,” University of New Brunswick, 23-Mar-2017.

[24] A. O. Allen, C. J. Hochanadel, J. A. Ghormley, and T. W. Davis, “Decomposition of Water and Aqueous Solutions Under Mixed Fast Neutron and Gamma Radiation,” J.Phys. Chem., vol. 56, p. 575, 1952.

[25] P. A. Yakabuskie, “The Influence of Long-Term Gamma-Radiation and Initially Dissolved Chemicals on Aqueous Kinetics and Interfacial Processes,” The University of Western Ontario, London, Ontario, 2015.

[26] K. Daub, X. Zhang, J. J. Noel, and J. C. Wren, “Gamma Radiation-Induced Carbon Steel Corrosion.” The Electrochemical Society, 2011.

[27] C. R. Stuart, “Mitigation of Hydrogen Production in the End Shield Cooling System.” CANDU Owners Group Inc., Feb-2012.

[28] X. Zhang, W. Xu, J. C. Shoesmith, and J. C. Wren, “Kinetics of H2O2 reaction with oxide films on carbon steel,” Corrosion Science, Mar. 2007.

[29] Autoclave Engineers, “Autoclave Engineers Maintenance and Operation Manual, Standards Regulation – Bolted (Gasche) Pressure Vessel Closure.” Autoclave Engineers, 12-May-2004.

[30] R. H. Perry and D. W. Green, Perry’s chemical engineers’ handbook. New York: McGraw-Hill, 2008.

[31] C. J. Geankoplis, Transport processes and separation process principles, 4th ed. Upper Saddle River, NJ: Prentice Hall Professional Technical Reference, 2003.

[32] W. M. Haynes, CRC handbook of chemistry and physics: A ready-reference book of chemical and physical data. Boca Raton: CRC Press, 2009.

[33] G. Glowa and C. R. Stuart, “A Radiolysis Model to Investigate the Production of Hydrogen in the End Shield Cooling System.” CANDU Owners Group Inc., Jan-2005.

[34] W. D. Felix, B. L. Gall, and L. M. Dorfman, “Pulse radiolysis studies. IX. Reactions of the ozonide ion in aqueous solution.,” J. Phys. Chem., vol. 71, pp. 384–392, 1967.

[35] M. S. Matheson and J. Rabani, “Pulse radiolysis of aqueous hydrogen solutions. I. Rate constants for reaction of eaq- with itself and other transients. II. The interconvertibility of eaq- and H.,” J. Phys. Chem., vol. 69, pp. 1324–1335, 1965.

[36] J. Rabani and M. S. Matheson, “The pulse radiolysis of aqueous solutions of potassium ferrocyanide.,” J. Phys. Chem, vol. 70, pp. 761–769, 1966.

[37] G. V. Buxton and C. R. Stuart, “Radiation chemistry of aqueous solutions of hydrazine at elevated temperatures - Oxygen-free solutions,” J. Chem. Soc., Faraday Trans., vol. 92, no. 9, pp. 1519–1525, 1996.

[38] G. A. Glowa, “A Plan for a Radiolysis Test Loop.” CANDU Owners Group Inc., Jul-2007.

[39] HACH-LANGE, “ORBISPHERE Model 31xxx Electrochemical Sensors - Installation and Maintenance Manual.” HACH-LANGE, May-2009.

[40] G. A. Glowa and J. R. Mitchell, “Experiments In Radiolytic Suppression.” CANDU Owners Group Inc., Jan-2010.

[41] P. A. Yakabuskie, J. M. Joseph, and J. C. Wren, “The effect of interfacial mass transfer on steady-state water radiolysis,” Radiation Physics and Chemistry, vol. 79, pp. 777–785, Feb. 2010.

[42] L. Chi and C. W. Turner, “Formation of Corrosion Products of Carbon Steel Under Condenser Operating Conditions and Their Impact on Steam Generator Tube Materials.” CANDU Owners Group Inc., Feb-2012.

[43] C. R. Stuart, “Mitigation of Hydrogen Production in the End Shield Cooling System,” presented at the NPC - 9th International Workshop on Radiolysis and Electrochemistry, Paris, France, 2012.

[44] G. A. Glowa and J. R. Mitchell, “Experiments In Radiolytic Suppression - Part III.” CANDU Owners Group Inc., May-2013.

[45] Y. A. Musa, M. Behazin, Q. Knapp, D. Mizzi, and J.C. Wren, “Effect of Water Radiolysis on Corrosion: Steel, Cobalt and Nickel Alloys,” presented at the 34rd Annual Conference of the Canadian Nuclear Society - 37th Annual CNS/CNA Student Conference, Eaton Centre Marriott, Toronto, Ontario, 2013.

[46] C. R. Stuart and G. A. Glowa, “Fundementals of Chemistry Under Irradiation Conditions: Experimental Directions.” CANDU Owners Group Inc., Apr-2014.

[47] J. Lyons, “End Shield Loop Manual - PROJ-024-001-ESLOOP-EXP-001.” Center for Nuclear Energy Research, Apr-2016.

Appendix A: Engineering Drawings

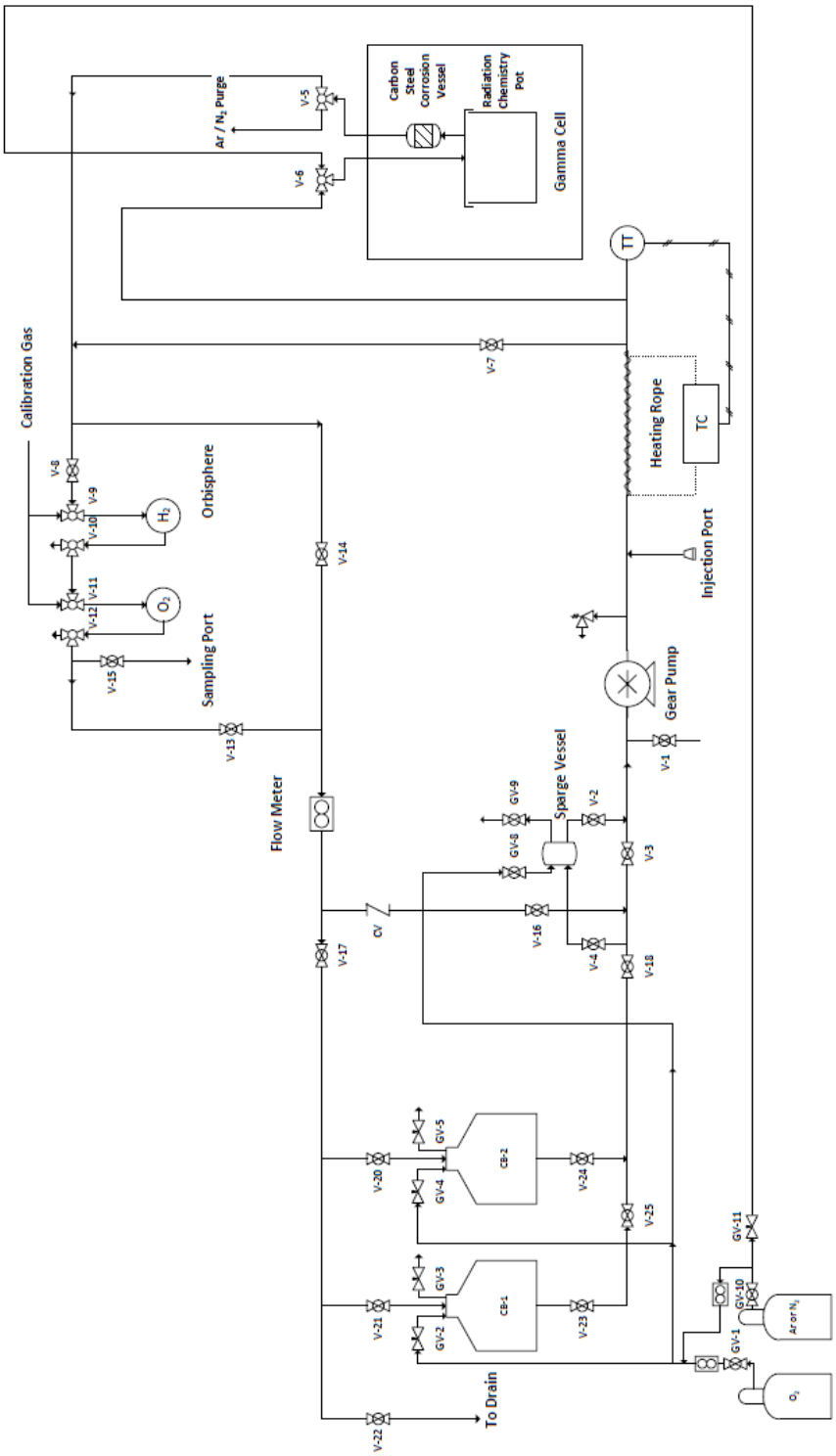


Figure A-1: Loop Process Flow Diagram

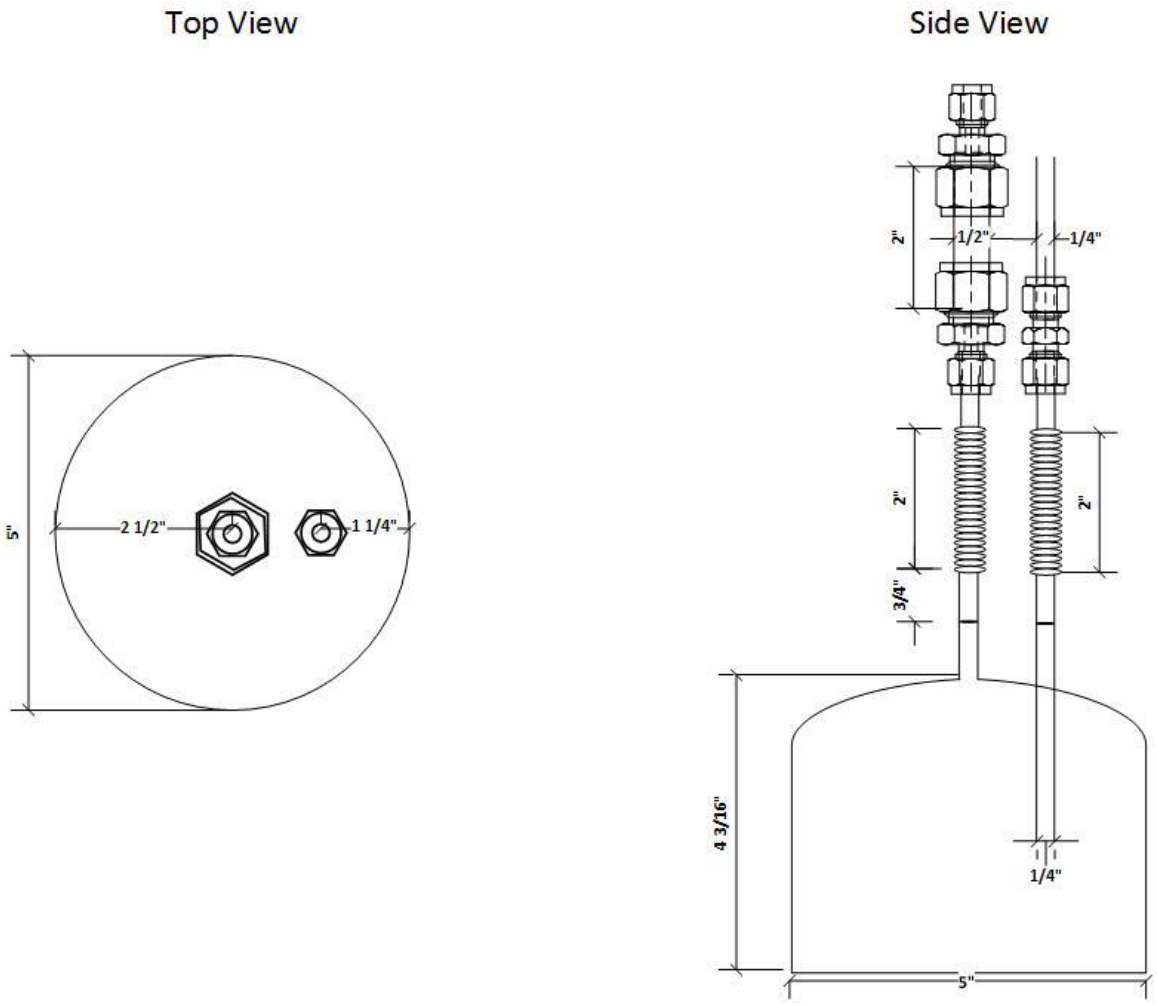


Figure A-2: Test Section Design Drawing

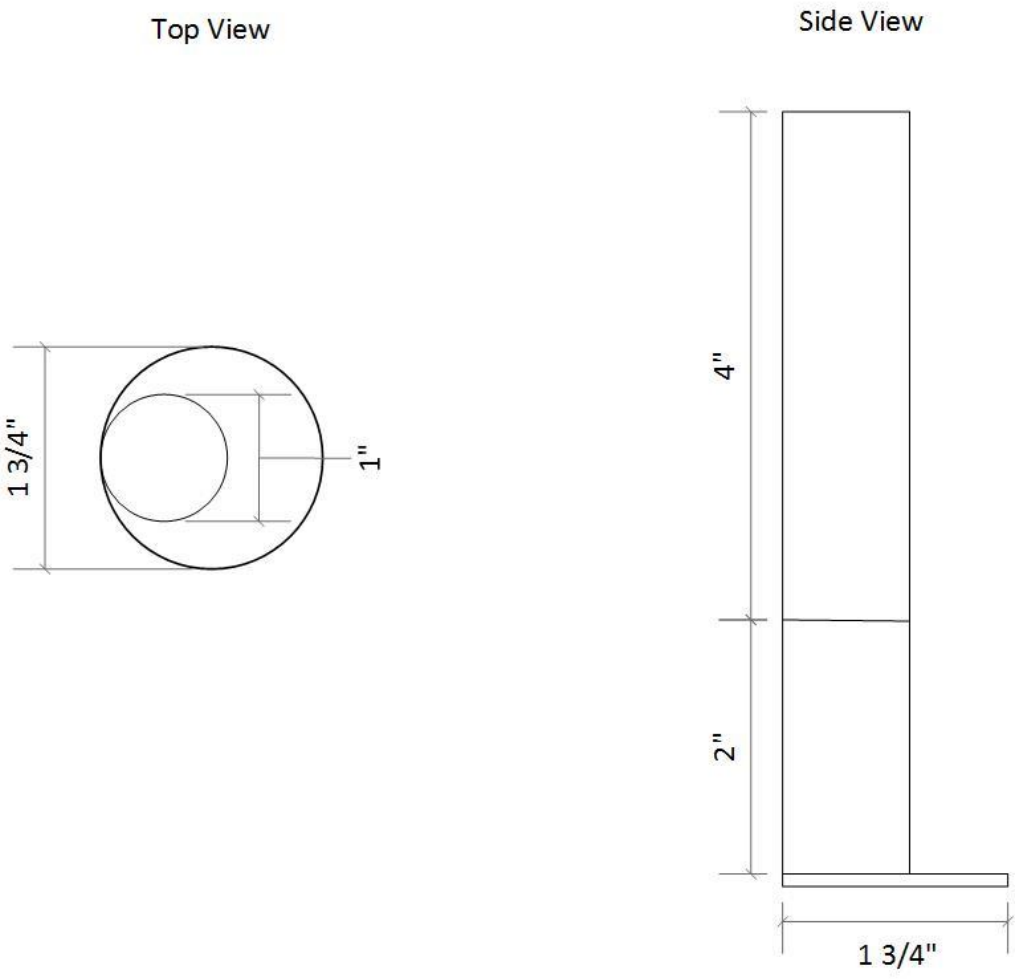


Figure A-3: Mesh Support Basket for Autoclave Aging

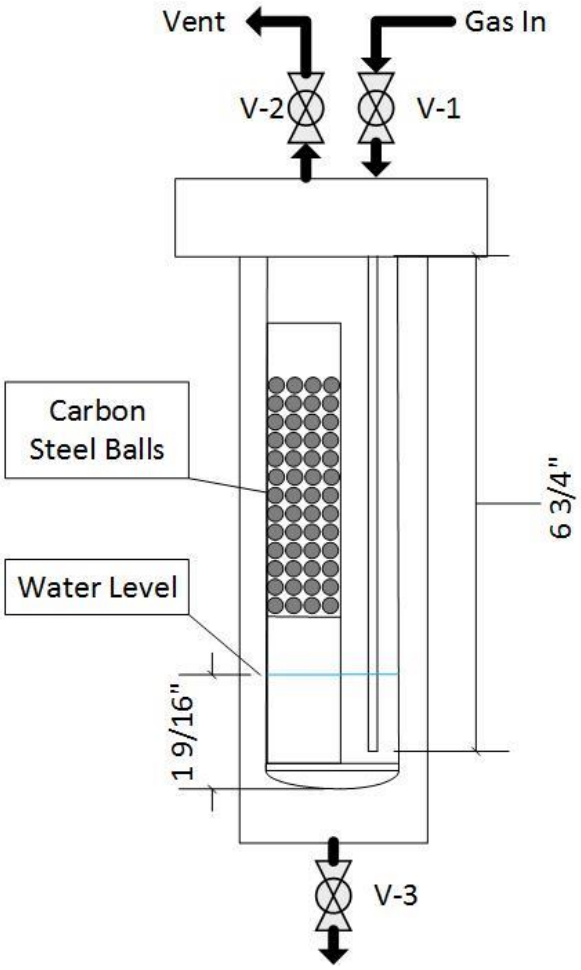


Figure A-4: Autoclave Configuration in CS Aging

Appendix B: Sparge Vessel Air Ingress Model

During the first recirculating corrosion test, the system's sparge vessel was left valved-in, meaning all of the system's water flowed through the sparge vessel. Prior to beginning the experiment, the sparge vessel was isolated from atmosphere as valves V-8 and V-9 were closed, and no external gas flow was applied (See Figure A-1 for reference). The results from this experiment are displayed in Figure B-1. Oxygen was initially removed by corrosion at a slowing rate, and at approximately 200 minutes the oxygen concentration began to increase.

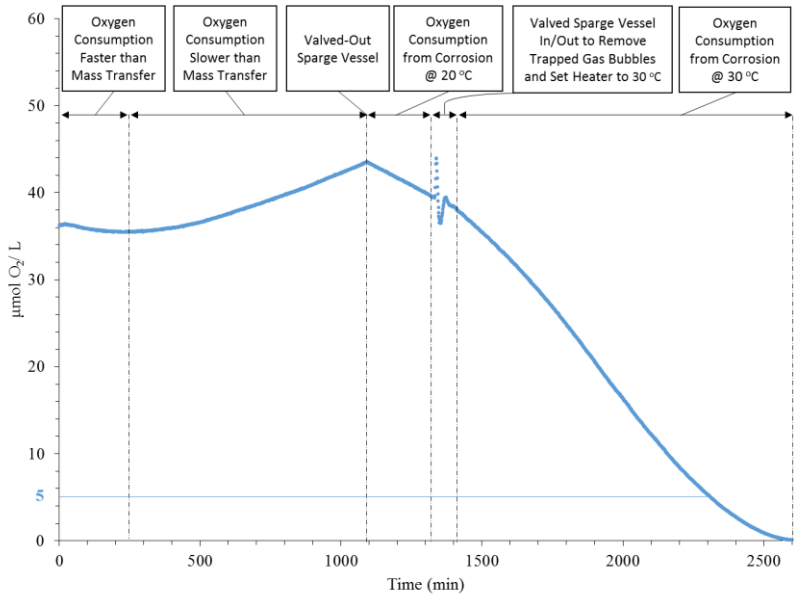


Figure B-1: Results of Corrosion Test # 1

This was attributed to oxygen transferring from the sparge vessel's cover gas into the water. When the test section was valved in, the oxygen concentration in the water would have been in equilibrium with the sparge vessel's gas cap, but as corrosion removed oxygen

from the water, the concentration gradient between the gas and liquid phases grew larger. This resulted in a higher rate of mass transfer, however, based on this explanation the oxygen concentration would not have increased and exceed its initial value, because it was already in equilibrium with the gas phase at that point. Therefore, there must also have been air ingress into the sparge vessel, most likely around its ground-glass joint. To verify the behavior was indicative of oxygen ingress into the cover gas, and subsequent diffusion into the water, a mass transfer model was formulated. To determine how the oxygen concentrations were varying in the liquid and gas phases a mass balance was carried out on each.

Liquid Phase Mass Balance:

$$\frac{d[O_2]_{Liq}}{dt} = [\dot{O}_2]_{in,Liq} - [\dot{O}_2]_{out,Liq} + [\dot{O}_2]_{generated,Liq} - [\dot{O}_2]_{consumed,Liq} \qquad \text{(B-1)}$$

Since no oxygen is leaving or being generated in the liquid, equation (B-1) can be reduced to equation (D-2).

$$\frac{d[O_2]_{Liq}}{dt} = [\dot{O}_2]_{in,Liq} - [\dot{O}_2]_{consumed,Liq} \qquad \text{(B-2)}$$

The oxygen consumption term can be determined by measuring the rate of oxygen consumption after the sparge vessel is valved out (i.e. from about 1100 minutes to 1300 minutes in Figure B-1). The data during this time interval has been plotted and displayed in Figure B-2, and renders an oxygen consumption rate of 0.0171μmolO_2/L/min. The data has a linear fit, which means the consumption rate of oxygen can be assumed to be constant

and independent of the oxygen concentration at the levels considered in this model, therefore, equation (B-2) can be written as equation (B-3).

$$\frac{d[O_2]_{Liq}}{dt} = [\dot{O}_2]_{in,Liq} - 0.0171\ \frac{\mu molO_2}{L.min} \qquad \text{(B-3)}$$

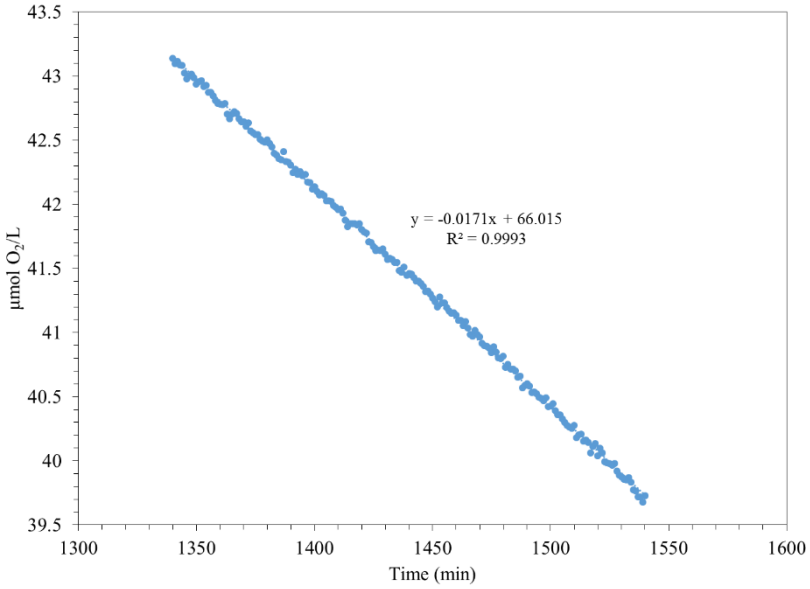


Figure B-2: Oxygen Consumption Rate with Sparge Vessel Valved-out

Referring back to Figure B-1, in the time interval between approximately 700 min and 1100 min, the oxygen concentration is increasingly linearly at a net rate of 0.0108 µmolO_2/L/min, as shown in Figure D-3.

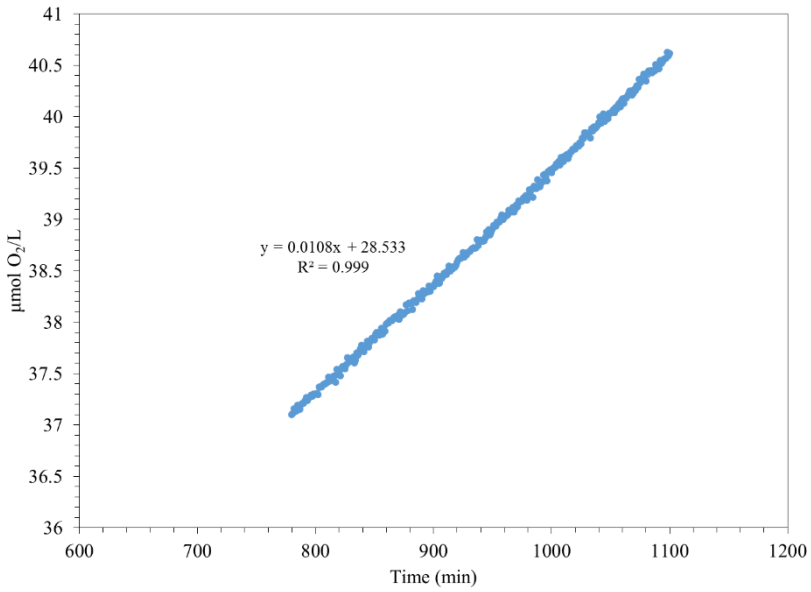


Figure B-3: Increasing Oxygen Concentration due to Air Ingress

This rate can be substituted into equation (B-3) to render a value for the rate of oxygen entering the liquid phase from the gas phase.

$$0.0108\ \frac{\mu molO_2}{L.min} = [\dot{O}_2]_{in,Liq} - 0.0171\ \frac{\mu molO_2}{L.min} \tag{B-4}$$

$$[\dot{O}_2]_{in,Liq} = 0.0279\ \frac{\mu molO_2}{L.min} \tag{B-5}$$

A mass balance around the gas phase in the sparge vessel can be carried out in order to determine the rate of leakage.

Gas Phase Mass Balance:

$$\frac{d[O_2]_{Gas}}{dt} = [\dot{O}_2]_{in,Gas} - [\dot{O}_2]_{out,Gas} + [\dot{O}_2]_{generated,Gas} - [\dot{O}_2]_{consumed,Gas} \tag{B-6}$$

If it is assumed that no oxygen is generated or consumed in the sparge vessel's gas phase, equation (B-6) can be reduced to equation (B-7).

$$\frac{d[O_2]_{Gas}}{dt} = [\dot{O}_2]_{in,Gas} - [\dot{O}_2]_{out,Gas} \quad \text{(B-7)}$$

The gas phase oxygen concentration can be related to the liquid phase concentration by assuming Henry's Law is valid, as described by equation (D-8).

$$[O_2]_{Gas} = \frac{[O_2]_{Liq}}{H_{O_2}} \quad \text{(B-8)}$$

Substituting equation (B-8) into equation (B-7) will render a relation in terms of the rate of change of oxygen in the liquid phase, as displayed by equation (B-9).

$$\frac{1}{H_{O_2}}\frac{d[O_2]_{Liq}}{dt} = [\dot{O}_2]_{in,Gas} - [\dot{O}_2]_{out,Gas} \quad \text{(B-9)}$$

Since all the oxygen leaving the gas phase is assumed to be entering the liquid phase, the rate of oxygen leaving the gas phase can be set equal to the rate entering the liquid phase, multiplied by the ratio of their volumes. Substituting this relationship, along with the net rate of oxygen change in the liquid phase (0.0108 μmolO_2/L/min) into equation (B-9), equation (B-10) is produced.

$$\frac{\left[0.0108\,\frac{\mu molO_2}{L.min}\right]}{H_{O_2}} = [\dot{O}_2]_{in,Gas} - \frac{V_{Liq}}{V_{Gas}}[\dot{O}_2]_{in,Liq} \quad \text{(B-10)}$$

The liquid volume of the loop is an estimated 1.7 L, and the sparge vessel gas space is estimated at approximately 70 mL. The Henry's Law constant for dissolved oxygen in

water at room temperature is equal to 0.03107 [30]. The oxygen ingress rate into the sparge vessel's gas phase can be estimated by substituting these values into equation (B-10), as shown in equations (B-11) and (B-12).

$$[\dot{O}_2]_{in,Gas} = \frac{\left[0.0108\,\frac{\mu molO_2}{L.min}\right]}{0.03107} + \frac{1.7L}{0.070L}\left[0.0279\,\frac{\mu molO_2}{L.min}\right] \tag{B-11}$$

$$[\dot{O}_2]_{in,Gas} \approx 1.00\,\frac{\mu molO_2}{L.min} \tag{B-12}$$

This leakage rate would be dependent on the oxygen concentration in the sparge vessel's gas phase, however, over the small range of concentrations being evaluated it will be assumed as constant for implementation into the model.

The model formation was based on the rate of oxygen transfer from the gas to liquid phase and its dependence on oxygen concentration in each. Referring back to equation (B-3), which assumes oxygen consumption from corrosion remains constant, a mass transfer relationship can be articulated to represent the rate of oxygen entering the liquid phase from the gas phase.

If the two-film theory is applied, the mass transfer from the gas to liquid phase will have a gas film resistance and a liquid film resistance. However, since oxygen is only slightly soluble in water, it will be assumed that the majority of the resistance will occur in the liquid film. Therefore, the overall mass transfer coefficient (K_L) can be set equal to the liquid film mass transfer coefficient (k_l) as described by equation (B-13).

$$K_L \approx k_l = \frac{D_{O_2/H_2O}}{\delta} \quad \text{(B-13)}$$

The liquid film mass transfer coefficient is estimated using an assumed liquid film thickness (δ), and the diffusivity of oxygen through water ($D_{O2/H2O}$) at 20 ^{o}C [31]. The flux of oxygen from the gas phase into the liquid phase is represented by equation (B-14), where the starred oxygen concentration term ($[O_2]_L^*$) is the liquid phase concentration that would be in equilibrium with the bulk gas phase. Therefore, this term can be substituted via Henry's law, which puts the equation in terms of the bulk gas phase oxygen concentration, as shown in equation (B-15).

$$N_{A,O_2} = K_L[[O_2]_L^* - [O_2]_L] \quad \text{(B-14)}$$

$$N_{A,O_2} = K_L\left[[O_2]_{Gas}H_{O_2} - [O_2]_L\right] \quad \text{(B-15)}$$

To obtain the rate of change in oxygen concentration, the flux (N_{A,O_2}) must be multiplied by the ratio of the sparge vessel's cross sectional area ($A_{SpargeVessel}$) to the system liquid volume (V_{Liquid}).

$$[\dot{O}_2]_{in,Liq} = \left[\frac{A_{Sparge\ Vessel}}{V_{Liquid}}\right] N_{A,O_2} = \left[\frac{A_{Sparge\ Vessel}}{V_{Liquid}}\right] K_L\left[[O_2]_{Gas}H_{O_2} - [O_2]_{Liq}\right] \quad \text{(B-16)}$$

If the sparge vessel is approximated as a cylinder, with a diameter of about 6 cm, the relation can be written as shown in equation (B-17).

$$[\dot{O}_2]_{in,Liq} = \left[\frac{\frac{\pi}{4}(6cm)^2}{1700cm^3}\right] \left[\frac{D_{O_2/H_2O}}{\delta}\right]\left[[O_2]_{Gas}H_{O_2} - [O_2]_{Liq}\right] \quad \text{(B-17)}$$

The rate of change in oxygen concentration in the gas phase needs to be defined, and is done so via a mass balance on oxygen in the gas phase. This has been previously derived as equation (B-7). If the ingress term is assumed to be constant at the value calculated in equation (B-12), then equation (B-7) can be written as equation (B-18).

$$\frac{d[O_2]_{Gas}}{dt} = 1.00\,\frac{\mu mol O_2}{L.min} - [\dot{O}_2]_{out,Gas} \tag{B-18}$$

If it assumed that all oxygen entering the liquid is due to a transfer from the sparge vessel's gas space, then the rate of oxygen leaving the gas phase can be set equal to the rate of oxygen entering the liquid, multiplied by a ratio of their volumes, as shown in equations (B-19) and (B-20).

$$V_{Gas,SpargeVessel}[\dot{O}_2]_{out,Gas} = V_{Liq,SpargeVessel}[\dot{O}_2]_{in,Liq} \tag{B-19}$$

$$[\dot{O}_2]_{out,Gas} = \frac{1.7L}{0.070L}[\dot{O}_2]_{in,Liq} \tag{B-20}$$

The model was formulated in Polymath's Differential Equation Solver, by implementing equations (B-3), (B-13), (B-17), (B-18), and (B-20). The constant values outlined in Table B-1 were also implemented into the model. The data generated by the model is plotted against the experimental data in Figure B-4 for comparison.

Table B-1: Values Used for Constants in Model

Parameter	Variable	Value
Diffusivity of Oxygen in Water	D_{O_2/H_2O}	2.42x10^{-5} cm^2/sec [31]
Liquid Film Thickness	δ	0.1 mm
Henry's Law Constant for Oxygen	H_{O_2}	0.03107
System Liquid Volume	V_{Liq}	1.7 L
Sparge Vessel Gas Volume	V_{Gas}	70 mL
Oxygen Ingress from Atmosphere into Sparge Vessel	$[\dot{O}_2]_{in,Gas}$	1.00 µmol/L.min

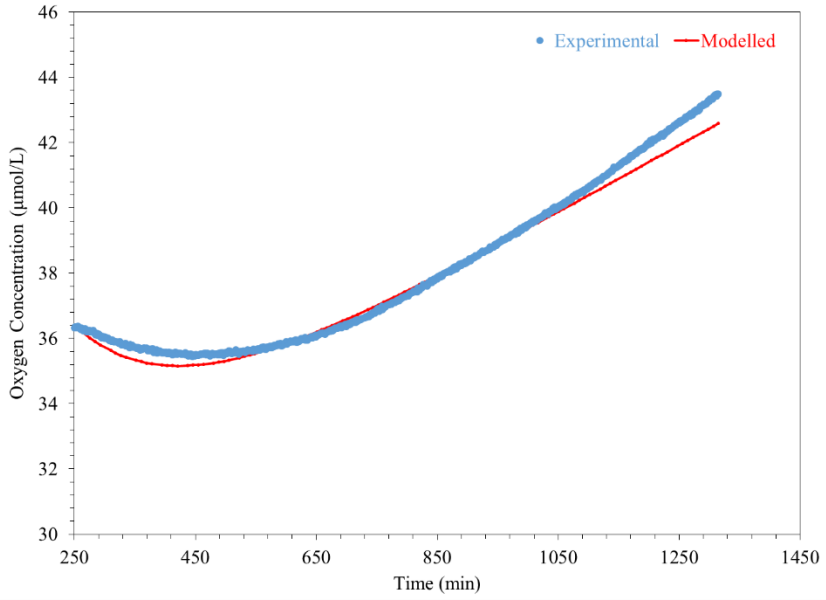


Figure B-4: Comparison of Experimental and Modelled Oxygen Ingress Behavior

The model seems to represent the behavior of the measured dissolved oxygen concentrations quite well. Therefore, the behavior exhibited by the system when the sparge vessel is valved-in is indicative an air ingress into the sparge vessel's gas space and subsequent diffusion into the liquid phase. This consequently masks the oxygen removal due to corrosion processes, hence, the sparge vessel should be valved out during experiments.

POLYMATH Report No Title

Ordinary Differential Equations 22-May-2017

Calculated values of DEQ variables

	Variable	Initial value	Minimal value	Maximal value	Final value
1	DiffusivityOfOxygenThroughWater	2.42E-05	2.42E-05	2.42E-05	2.42E-05
2	GasOxygenConcentration	0.0011715	0.0011715	0.0016441	0.0016441
3	HenrysConstant	0.03107	0.03107	0.03107	0.03107
4	LiquidFilmThickness	0.0075	0.0075	0.0075	0.0075
5	LiquidOxygenConcentration	3.64E-05	3.516E-05	4.259E-05	4.259E-05
6	OverallMassTransferCoefficient	0.0032267	0.0032267	0.0032267	0.0032267
7	OxygenConsumedFromCorrosion	1.71E-08	1.71E-08	1.71E-08	1.71E-08
8	OxygenFlowIntoLiquid	-1.173E-14	-1.173E-14	2.739E-08	2.739E-08
9	OxygenFlowOutOfGas	-2.85E-13	-2.85E-13	6.651E-07	6.651E-07
10	OxygenIngressRate	1.0E-06	1.0E-06	1.0E-06	1.0E-06

11	SpargeVesselArea	28.3068	28.3068	28.3068	28.3068
12	SpargeVesselGasVolume	70.	70.	70.	70.
13	SystemLiquidVolume	1700.	1700.	1700.	1700.
14	t	0	0	1065.	1065.

Differential equations

1 d(LiquidOxygenConcentration)/d(t) = OxygenFlowIntoLiquid-OxygenConsumedFromCorrosion

mol/L.min

2 d(GasOxygenConcentration)/d(t) = OxygenIngressRate-OxygenFlowOutOfGas

mol/L.min

Explicit equations

1 LiquidFilmThickness = 0.0075

cm

2 OxygenConsumedFromCorrosion = 0.0171E-6

mol/L.min

3 DiffusivityOfOxygenThroughWater = 2.42E-5

cm2/sec

4 OverallMassTransferCoefficient = DiffusivityOfOxygenThroughWater/LiquidFilmThickness

cm/sec

5 HenrysConstant = 0.03107

unitless

6 OxygenIngressRate = 1.00E-6

mole/L.min

7 SpargeVesselGasVolume = 70

cm3

8 SystemLiquidVolume = 1700

cm3

9 SpargeVesselArea = (3.1452/4)*((6)^2)

cm2

10 OxygenFlowIntoLiquid = (SpargeVesselArea/SystemLiquidVolume)*OverallMassTransferCoefficient*(60)*(HenrysConstant*GasOxygenConcentration-LiquidOxygenConcentration)

mol/L.min

11 OxygenFlowOutOfGas = (SystemLiquidVolume/SpargeVesselGasVolume)*OxygenFlowIntoLiquid

General

Total number of equations	13
Number of differential equations	2
Number of explicit equations	11
Elapsed time	0.000 sec
Solution method	RKF_45
Step size guess. h	0.000001
Truncation error tolerance. eps	0.01

Appendix C : Corrosion and Penetration Rates Sample Calculations

Corrosion and penetration rates can be inferred from the oxygen consumption and hydrogen production rates in corrosion-only experiments simply through stoichiometry. If it is assumed that all oxygen consumption and hydrogen production is due to the oxidation of Fe to Fe^{2+}, and the loop volume is approximately 1.2 L, these rates can be estimated, as shown in equations (C-1) – (C-10).

Anodic Half Reaction:

$$Fe \rightarrow Fe^{2+} + 2e^{-} \tag{C-1}$$

Cathodic Half Reactions (Alkaline Conditions):

$$\frac{1}{2}O_2 + H_2O + 2e^{-} \rightarrow 2OH^{-} \tag{C-2}$$

or

$$2H_2O + 2e^{-} \rightarrow H_2 + 2OH^{-} \tag{C-3}$$

As stated previously, the corrosion rate by oxygen reduction can be estimated based on the stoichiometry displayed in reactions (C-1) to (C-3).

$$Corrosion\ Rate = \frac{\left[\frac{33 \mu mol O_2}{L\ day}\right]\left[\frac{2\ Fe}{O_2}\right][1.2\ L]\left[\frac{55.845\ \mu gFe}{\mu molFe}\right]\left[\frac{mgFe}{1000 \mu gFe}\right]}{SA_{Total}} \tag{C-4}$$

However, a value of total carbon steel surface area (SA_{Total}) is still required and can be estimated based on; the measured total mass of carbon steel balls ($m_{cs,total}$), the calculated

mass (m_{ball}), diameter (D_{ball}), and surface area (SA_{ball}) of a single carbon steel ball, and the density of the carbon steel (ρ_{Fe}), as shown in equations (C-5) and (C-6).

$$SA_{Total} = \left[\frac{m_{cs,total}}{m_{ball}}\right] SA_{ball} = \left[\frac{21.3431\ g}{\frac{\pi}{6} D_{ball}^3\ \rho_{Fe}}\right] \pi D_{ball}^2 = \left[\frac{21.3431\ g}{\frac{\pi}{6} D_{ball}\ \rho_{Fe}}\right] \quad \text{(C-5)}$$

$$SA_{Total} = \left[\frac{6(21.3431\ g)}{(0.08cm)\left(7.850\frac{g}{cm^3}\right)}\right]\left[\frac{0.1\ dm}{1cm}\right]^2 = 2.04\ dm^2 \quad \text{(C-6)}$$

The corrosion rate by oxygen reduction can then be calculated by substituting this surface area into equation (C-4), as shown in equations (C-7) and (C-8).

$$Corrosion\ Rate\ (CR) = \frac{\left[\frac{33 \mu molO_2}{L\ day}\right]\left[\frac{2\ Fe}{O_2}\right][1.2\ L]\left[\frac{55.845\ \mu gFe}{\mu molFe}\right]\left[\frac{mgFe}{1000 \mu gFe}\right]}{2.04\ dm^2} \quad \text{(C-7)}$$

$$Corrosion\ Rate\ = 2.20\ \frac{mg}{dm^2 day} \quad \text{(C-8)}$$

The penetration rate can be estimated from the corrosion rate by dividing by the density of steel, as shown in equations (C-9) and (C-10).

$$Penetration\ Rate = \frac{CR}{\rho_{Fe}} = \left[\frac{2.20\ \frac{mg}{dm^2 day}}{7.850\frac{g}{cm^3}}\right]\left[\frac{g}{1000\ mg}\right]\left[\frac{0.1\ dm}{cm}\right]^2\left[\frac{365\ days}{year}\right]\left[\frac{10^4 \mu m}{cm}\right] \quad \text{(C-9)}$$

$$Penetration\ Rate = 10.23\ \frac{\mu m}{year} \quad \text{(C-10)}$$

The corrosion and penetration rates from water reduction can be calculated in the same manner, except the stoichiometry from reaction (C-3) should be applied, as opposed to reaction (C-2). Doing so renders a corrosion and penetration rate of 0.43 mg/dm^2.day and 2.0 μm/yr, respectively.

Appendix D: Methanol Equilibrium Model

In order to gain insight into the effects of carbon dioxide production from methanol injections on end shield cooling system chemistry, a simple equilibrium model was produced; the reactions accounted for by the model are displayed in Table D-1.

Table D-1: Reactions and Corresponding Equilibrium Constants

Reaction #	Reaction
1	$CO_2 + H_2O \rightleftharpoons H_2CO_3$
2	$H_2CO_3 \rightleftharpoons H^+ + HCO_3^-$
3	$HCO_3^- \rightleftharpoons H^+ + CO_3^{2-}$
4	$2Li^+ + CO_3^{2-} \rightleftharpoons Li_2CO_3$
5	$Li^+ + HCO_3^- \rightleftharpoons LiHCO_3$
6	$H_2O \rightleftharpoons H^+ + OH^-$
7	$LiOH \leftrightarrows Li^+ + OH^-$

Equilibrium constants for each reaction were estimated using standard state Gibbs free energies of reaction (ΔG_{rxn}^o). These were determined using tabulated values of Gibbs free energies of formation (ΔG_f^o) for each species involved, as shown by equations (D-1) and (D-2).

$$\Delta G_{rxn}^o = \sum v_i \Delta G_{f\ Products}^o - \sum v_i \Delta G_{f\ Reactants}^o \quad \text{(D-1)}$$

$$K_{eq} = exp\left[\frac{-\Delta G^o_{rxn}}{RT}\right] \quad \text{(D-2)}$$

The values of the Gibbs free energies of formation (ΔG_f^o) are displayed in Table D-2, along with their corresponding reference.

Table D-2: Gibbs Free Energies of Formation

Species	ΔG_f^o [kJ/mol]	Reference
H_2O	-237.20	[30]
H_2CO_3	-623.42	[30]
Li_2CO_3	-1119.55	[30]
LiOH	-453.08	[30]
$LiHCO_3$	-882.74	[30]
CO_3^{2-}	-527.80	[32]
HCO^{3-}	-586.8	[32]
OH^-	-157.20	[32]
Li^+	-293.30	[32]
H^+	0	[32]
CO_2	-394.40	[32]

The subsequently calculated Gibbs free energies of reaction and equilibrium constants are displayed in Table D-3. These values were implemented into Polymath's non-linear

equation solver along with several equations in order to estimate equilibrium conditions following a methanol injection.

Table D-3: Equilibrium Constants and Gibbs Energies of Reaction

Reaction #	Gibbs Free Energy of Reaction (kJ/mol)	Equilibrium Constants K_{eq}
1	8.18	0.03689
2	36.62	3.841×10^{-7}
3	59.00	4.610×10^{-11}
4	-5.150	7.984
5	-2.640	2.901
6	80.00	9.653×10^{-15}
7	2.580	0.3532

The model assumes that all methanol injected into the system will convert to carbon dioxide, after which the equilibrium chemistry will be governed by the relationships displayed in equations (D-3) – (D-9).

$$K_{eq,1} = \frac{[H_2CO_3]}{[CO_2]} \tag{D-3}$$

$$K_{eq,2} = \frac{[H^+][HCO_3^-]}{[H_2CO_3]} \tag{D-4}$$

$$K_{eq,3} = \frac{[{CO_3}^{2-}][H^+]}{[{HCO_3}^-]} \quad \text{(D-5)}$$

$$K_{eq,4} = \frac{[Li_2CO_3]}{[{CO_3}^{2-}][Li^+]^2} \quad \text{(D-6)}$$

$$K_{eq,5} = \frac{[LiHCO_3]}{[{HCO_3}^-][Li^+]} \quad \text{(D-7)}$$

$$K_{eq,6} = [H^+][OH^-] \quad \text{(D-8)}$$

$$K_{eq,7} = \frac{[Li^+][OH^-]}{[LiOH]} \quad \text{(D-9)}$$

The equilibrium constants make up seven of the ten relations required to determine the unknowns within the system of equations. At equilibrium conditions a charge balance can be applied, such that the concentration of positive ions in solution is equal to that of the negative, as displayed in equation (D-10).

$$[H^+] + [Li^+] = [OH^-] + [HCO_3^-] + 2[CO_3^{2-}] \quad \text{(D-10)}$$

Finally, balances on total lithium and carbon can be implemented. The amounts of both are set parameters based on the amount of lithium hydroxide initially present within the system and the amount of carbon injected in the form of methanol.

$$[Li]_{Total} = [LiOH] + [LiHCO_3] + 2[Li_2CO_3] + [Li^+] \quad \text{(D-11)}$$

$$[C]_{Total} = [CO_3^{2-}] + [CO_2] + [HCO_3^-] + [LiHCO_3] + [Li_2CO_3] + [H_2CO_3] \quad \text{(D-12)}$$

The solution specific conductivity (Λ^{∞}) at equilibrium can be estimated using tabulated values for ionic molar conductivities at infinite dilution, as displayed in Table D-4.

$$\Lambda^{\infty} = \lambda^{\infty}_{H^+}[H^+] + \lambda^{\infty}_{Li^+}[Li^+] + \lambda^{\infty}_{OH^-}[OH^-] + \lambda^{\infty}_{HCO_3^-}[HCO_3^-] + 2\lambda^{\infty}_{CO_3^{2-}}[CO_3^{2-}] \quad \text{(D-13)}$$

Table D-4: Ionic Molar Conductivities at Infinite Dilution [10]

Ion	Ionic Molar Conductivity (λ^{∞}) ($S \cdot cm^2 \cdot mol^{-1} \cdot eq^{-1}$)
H^+	349.7
Li^+	38.7
OH^-	198
HCO_3^-	44.5
½ CO_3^{2-}	69.3

All equations were implemented into Polymath's non-linear equation solver, which predicted equilibrium conditions at various methanol injection quantities. The results of the model are discussed in Section 5.2.2.

Calculated values of NLE variables

	Variable	Value	f(x)	Initial Guess
1	CO2	1.569E-07	0	0
2	CO3minus2	6.666E-07	1.697E-19	0
3	H2CO3	5.788E-09	0	0
4	HCO3minus	5.67E-06	-2.541E-21	0
5	Hplus	3.921E-10	1.548E-21	3.162E-10
6	Li2CO3	5.321E-15	7.756E-22	0
7	LiHCO3	5.201E-10	0	0
8	LiOH	2.204E-09	2.419E-21	0
9	Liplus	3.162E-05	7.454E-20	3.162E-05
10	OHminus	2.462E-05	9.021E-14	3.162E-05

	Variable	Value
1	CTotal	6.5E-06
2	EquilibriumConstantRxn1	0.036892
3	EquilibriumConstantRxn2	3.841E-07
4	EquilibriumConstantRxn3	4.61E-11
5	EquilibriumConstantRxn4	7.984301

6	EquilibriumConstantRxn5	2.900721
7	EquilibriumConstantRxn6	9.653E-15
8	EquilibriumConstantRxn7	0.3531877
9	GibbsEnergyFormationCO2	-394.4
10	GibbsEnergyFormationCO3minus2	-527.8
11	GibbsEnergyFormationH2CO3	-623.42
12	GibbsEnergyFormationH2O	-237.2
13	GibbsEnergyFormationHCO3minus	-586.8
14	GibbsEnergyFormationHplus	0
15	GibbsEnergyFormationLi2CO3	-1119.55
16	GibbsEnergyFormationLiHCO3	-882.74
17	GibbsEnergyFormationLiOH	-453.08
18	GibbsEnergyFormationLiplus	-293.3
19	GibbsEnergyFormationOHminus	-157.2
20	GibbsEnergyReaction1	8.18
21	GibbsEnergyReaction2	36.62
22	GibbsEnergyReaction3	59.
23	GibbsEnergyReaction4	-5.15
24	GibbsEnergyReaction5	-2.64
25	GibbsEnergyReaction6	80.

26	GibbsEnergyReaction7	2.58
27	InfiniteDilutionCondCO3minus2	69.3
28	InfiniteDilutionCondHCO3minus	44.5
29	InfiniteDilutionCondHplus	349.7
30	InfiniteDilutionCondLiplus	38.7
31	InfiniteDilutionCondOHminus	198.
32	LiTotal	3.162E-05
33	pH	9.406567
34	R	8.3145
35	SolutionSpecificConductivity	6.442725

Nonlinear equations

1 f(CO2) = (H2CO3/(EquilibriumConstantRxn1))-CO2 = 0

mole/L

2 f(H2CO3) = ((Hplus*HCO3minus)/EquilibriumConstantRxn2)-H2CO3 = 0

mole/L

3 f(HCO3minus) = (Hplus*CO3minus2/EquilibriumConstantRxn3)-HCO3minus = 0

mole/L

4 f(CO3minus2) = (Li2CO3/((Liplus^2)*EquilibriumConstantRxn4))-CO3minus2 = 0

mole/L

5 f(LiHCO3) = EquilibriumConstantRxn5*Liplus*HCO3minus - LiHCO3 = 0

mole/L

6 f(OHminus) = (EquilibriumConstantRxn6/Hplus)-OHminus = 0

mole/L

7 f(Liplus) = (LiOH*EquilibriumConstantRxn7/OHminus)-Liplus = 0

mole/L

8 f(LiOH) = LiTotal-Liplus-2*Li2CO3-LiHCO3-LiOH = 0

mole/L

9 f(Hplus) = 2*CO3minus2+HCO3minus+OHminus-Liplus-Hplus = 0

mole/L

10 f(Li2CO3) = CTotal-CO2-CO3minus2-HCO3minus-H2CO3-Li2CO3-LiHCO3 = 0

mole/L

Explicit equations

1 CTotal = 6.5*10^(-6)

mole/L

2 LiTotal = 10^(-4.5)

mole/L

3 GibbsEnergyFormationCO2 = -394.4

kJ/mole

4 GibbsEnergyFormationH2O = -237.2

kJ/mole

```
5  GibbsEnergyFormationH2CO3 = -623.42
```

kJ/mole

```
6  GibbsEnergyFormationLi2CO3 = -1119.55
```

kJ/mole

```
7  GibbsEnergyFormationLiOH = -453.08
```

kJ/mole

```
8  GibbsEnergyFormationLiHCO3 = -882.74
```

kJ/mole

```
9  GibbsEnergyFormationCO3minus2 = -527.8
```

kJ/mole

```
10 GibbsEnergyFormationHCO3minus = -586.8
```

kJ/mole

```
11 GibbsEnergyFormationOHminus = -157.2
```

kJ/mole

```
12 GibbsEnergyFormationLiplus = -293.3
```

kJ/mole

```
13 GibbsEnergyFormationHplus = 0
```

kJ/mole

```
14 GibbsEnergyReaction1 = GibbsEnergyFormationH2CO3 - (GibbsEnergyFormationH2O +
   GibbsEnergyFormationCO2)
```

kJ/mole

15 GibbsEnergyReaction2 = GibbsEnergyFormationHCO3minus + GibbsEnergyFormationHplus - GibbsEnergyFormationH2CO3

kJ/mole

16 GibbsEnergyReaction3 = GibbsEnergyFormationCO3minus2 + GibbsEnergyFormationHplus - GibbsEnergyFormationHCO3minus

kJ/mole

17 GibbsEnergyReaction4 = GibbsEnergyFormationLi2CO3 - (GibbsEnergyFormationCO3minus2 + 2*GibbsEnergyFormationLiplus)

kJ/mole

18 GibbsEnergyReaction5 = GibbsEnergyFormationLiHCO3 - (GibbsEnergyFormationLiplus + GibbsEnergyFormationHCO3minus)

kJ/mole

19 GibbsEnergyReaction6 = GibbsEnergyFormationOHminus + GibbsEnergyFormationHplus - GibbsEnergyFormationH2O

kJ/mole

20 GibbsEnergyReaction7 = GibbsEnergyFormationLiplus + GibbsEnergyFormationOHminus - GibbsEnergyFormationLiOH

kJ/mole

21 R = 8.3145

J/mole.K

22 EquilibriumConstantRxn1 = exp(-(GibbsEnergyReaction1*1000)/(R*298.15))

23 EquilibriumConstantRxn2 = exp(-(GibbsEnergyReaction2*1000)/(R*298.15))

24 EquilibriumConstantRxn3 = exp(-(GibbsEnergyReaction3*1000)/(R*298.15))

25 EquilibriumConstantRxn4 = exp(-(GibbsEnergyReaction4*1000)/(R*298.15))

```
26 EquilibriumConstantRxn5 = exp(-(GibbsEnergyReaction5*1000)/(R*298.15))
27 EquilibriumConstantRxn6 = exp(-(GibbsEnergyReaction6*1000)/(R*298.15))
28 EquilibriumConstantRxn7 = exp(-(GibbsEnergyReaction7*1000)/(R*298.15))
29 InfiniteDilutionCondHCO3minus = 44.5
30 InfiniteDilutionCondHplus = 349.7
31 InfiniteDilutionCondLiplus = 38.7
32 InfiniteDilutionCondOHminus = 198
33 InfiniteDilutionCondCO3minus2 = 69.3
34 SolutionSpecificConductivity =
   (Hplus*(1)*InfiniteDilutionCondHplus+OHminus*(1)*InfiniteDilutionCondOHminus+Liplus*(
   1)*InfiniteDilutionCondLiplus+CO3minus2*(2)*InfiniteDilutionCondCO3minus2+HCO3minus
   *(1)*InfiniteDilutionCondHCO3minus)*1000
```

microS/cm

```
35 pH = -log((Hplus))
```

Conditions for solution

CO2	Any real value
H2CO3	Any real value
HCO3minus	Any real value
CO3minus2	Any real value
LiHCO3	Any real value
OHminus	Any real value
Liplus	Any real value
LiOH	Any real value

Hplus	Any real value
Li2CO3	Any real value

General Settings

Total number of equations	45
Number of implicit equations	10
Number of explicit equations	35
Elapsed time	0.0000 sec
Solution method	CONSTRAINED
Convergence tolerance	0.0000001
Maxumum # of iterations	150
# of iterations used	12

Appendix E: Radiation Chemistry Model

A reaction kinetics model was formulated in order to better understand the radiation chemistry behavior in the system. The model assumes Standard Atmospheric Temperature and Pressure (SATP) conditions, and only accounts for the effects of low LET radiation. The g-values implemented for the primary radiolysis species are displayed in Table E-1.

Table E-1: g-Values for Water at Room Temperature for Low LET Radiation [33]

Primary Species	g-Value (Species/100 eV)
$e^-_{(aq)}$	2.54
H^+	2.54
$\cdot H$	0.53
$\cdot OH$	2.60
H_2	0.43
H_2O_2	0.5(g($e^-_{(aq)}$) + 2 g(H_2) + g($\cdot H$) - g($\cdot OH$))
HO_2/O_2^-	0

The g-value for $\cdot HO_2/O_2^-$ is very small, and has been assumed to be negligible for the purposes of this model. The g-values applied to the model satisfy the material balance required for water radiolysis as displayed in equation (E-1) [8].

$$2g(H_2) + g(\cdot H) + g\left(e^-_{(aq)}\right) = 2g(H_2O_2) + g(\cdot OH) \quad \text{(E-1)}$$

The yields of primary products ($G(X)$) were modelled using the relation displayed in equation (E-2), whereby "X" represents the primary species in question.

$$G(X) = Dose\ Rate \cdot g(X) \cdot \rho_{H_2O} \cdot \left(1.036x10^{-7}\ \frac{mol \cdot 100eV}{J \cdot \#}\right) \qquad \text{(E-2)}$$

Once the yields of primary species were defined, the homogeneous reaction kinetics were implemented. The elementary reactions considered in the model are displayed in Table E-2, along with their corresponding rate constants at 25 °C, and source of reference.

Table E-2: Radiation Chemistry Reactions Considered in Model

Reaction #	Reaction	Rate Constant (k_i)	Reference
As numbered in model	[-]	[1st Order: s^{-1}] [2nd Order: $L \cdot mol^{-1} \cdot s^{-1}$]	[-]
2	$e^-_{(aq)} + e^-_{(aq)} + (2H_2O) \rightarrow H_2 + 2OH^-$	$6.20x10^9$	[8]
3	$H + H \rightarrow H_2$	$4.62x10^9$	[8]
4	$OH + OH \rightarrow H_2O_2$	$4.54x10^9$	[8]
5	$e^-_{(aq)} + H + (H_2O) \rightarrow H_2 + OH^-$	$2.49x10^{10}$	[8]
6	$e^-_{(aq)} + OH \rightarrow OH^-$	$3.34x10^{10}$	[8]
7	$H + OH \rightarrow H_2O$	$1.03x10^{10}$	[8]
8	$e^-_{(aq)} + H_2O_2 \rightarrow OH + OH^-$	$1.22x10^{10}$	[8]
9	$e^-_{(aq)} + O_2 \rightarrow O_2^-$	$2.11x10^{10}$	[8]
10	$e^-_{(aq)} + O_2^- + (H_2O) \rightarrow H_2O_2 + 2OH^-$	$1.19x10^{10}$	[8]

11	$e^-_{(aq)} + HO_2 \rightarrow HO_2^-$	1.19x10^{10}	[8]
12	$H + H_2O_2 \rightarrow OH + H_2O$	3.16x10^{7}	[8]
13	$H + O_2 \rightarrow HO_2$	1.20x10^{10}	[8]
14	$H + HO_2 \rightarrow H_2O_2$	1.03x10^{10}	[8]
15	$H + O_2^- \rightarrow HO_2^-$	1.03x10^{10}	[8]
16	$OH + H_2O_2 \rightarrow HO_2 + H_2O$	2.65x10^{7}	[8]
17	$OH + O_2^- \rightarrow O_2 + OH^-$	1.02x10^{10}	[8]
18	$OH + HO_2 \rightarrow O_2 + H_2O$	8.44x10^{9}	[8]
19	$HO_2 + HO_2 \rightarrow H_2O_2 + O_2$	7.31x10^{5}	[8]
20	$O_2^- + HO_2 + (H_2O) \rightarrow H_2O_2 + O_2 + OH^-$	9.47x10^{7}	[8]
21	$O_2^- + O_2^- + (2H_2O) \rightarrow H_2O_2 + O_2 + 2OH^-$	0.3	[8]
22	$2H_2O_2 \rightarrow 2H_2O + O_2$	8.29x10^{-8}	[8]
22a	$H_2O_2 \rightarrow 2OH$	8.29x10^{-8}	[8]
33	$OH + HO_2^- \rightarrow O_2^- + H_2O$	7.49x10^{9}	[8]
34	$O^- + H_2O_2 \rightarrow HO_2 + OH^-$	7.49x10^{9}	[8]
35	$O^- + HO_2^- \rightarrow O_2^- + OH^-$	6.65x10^{8}	[8]
36	$O^- + H_2 \rightarrow H + OH^-$	1.17x10^{8}	[8]
38	$e^-_{(aq)} + HO_2^- \rightarrow O^- + OH^-$	3.15x10^{9}	[34]
39	$e^-_{(aq)} + O^- + H_2O \rightarrow 2OH^-$	2.19x10^{10}	[35]
40	$O^- + OH \rightarrow HO_2^-$	7.21x10^{9}	[36]

In addition to the radiolysis reactions accounted for in Table E-2, further equilibrium reactions were incorporated into the model. The reactions, along with their backward and forward rate constants are displayed in Table E-3.

Table E-3: Equilibrium Reactions Incorporated into Radiolysis Model [8]

Reaction #	Reaction	Forward Rate Constant (kf)	Backward Rate Constant (kb)
As numbered in model	[-]	[1st Order: s^{-1}] [2nd Order: $L \cdot mol^{-1} \cdot s^{-1}$]	[1st Order: s^{-1}] [2nd Order: $L \cdot mol^{-1} \cdot s^{-1}$]
23	$H_2O \rightleftharpoons H^+ + OH^-$	1.29×10^{-5}	1.06×10^{11}
24	$H_2O_2 \rightleftharpoons H^+ + HO_2^-$	6.49×10^{-2}	4.52×10^{10}
25	$H_2O_2 + OH^- \rightleftharpoons HO_2^- + H_2O$	1.18×10^{10}	9.97×10^{5}
26	$OH \rightleftharpoons H^+ + O^-$	6.49×10^{-2}	4.52×10^{10}
27	$OH + OH^- \rightleftharpoons +O^- + H_2O$	1.18×10^{10}	9.97×10^{5}
28	$HO_2 \rightleftharpoons H^+ + O_2^-$	6.62×10^{5}	4.52×10^{10}
29	$HO_2 + OH^- \rightleftharpoons O_2^- + H_2O$	1.18×10^{10}	9.78×10^{-2}
30	$H \rightleftharpoons H^+ + e_{(aq)}^-$	3.70	2.02×10^{10}
31	$H + OH^- \rightleftharpoons e_{(aq)}^- + H_2O$	1.86×10^{7}	1.23×10^{1}
32	$H + H_2O \rightleftharpoons H_2 + OH$	2.26×10^{-5}	3.37×10^{7}
37	$O^- + O_2 \rightleftharpoons O_3^-$	3.47×10^{9}	1.90×10^{3}

The rate constants were implemented into the model in the form displayed in equations (E-3) and (E-4), where "[A]" and "[B]" represent the concentration of the reactants taking part in the reaction, "a" and "b" represent the stoichiometric reaction coefficients, and "k" represents the rate constant. The example displayed in equations (E-3) and (E-4) is measuring the rate of change in species "A".

$$aA + bB \rightarrow cC + dD \tag{E-3}$$

$$\frac{d[A]}{dt} = -k[A]^a[B]^b \tag{E-4}$$

All relationships were entered into Polymath's differential equation solver, which generates the concentrations of each species as a function time, in a set time interval.

In an attempt to replicate the behavior of irradiated systems with carbon steel corrosion, an oxygen consumption term was incorporated into the model to represent corrosion effects. In order to do so, the integral method was applied to experimental data from early corrosion experiments. As previously mentioned, the oxygen consumption rate displayed a pseudo zeroth order dependence at higher concentrations, and a ½ order dependence at lower concentrations ($\leqslant$2.5μmol/L). A rate constant was extracted from corrosion-only data below oxygen concentrations of 2.5 μmol/L.

Application of the integral method involves assuming an order of rate dependence ("a") on oxygen concentration, given that the rate of change in oxygen concentration ($[O_2]$) follows the relationship displayed in equation (E-5); where k is a rate constant.

$$\frac{d[O_2]}{dt} = -k[O_2]^a \qquad \text{(E-5)}$$

If the order of is assumed to be ½, then equation (G-5) can be integrated to render equation (E-6); where $[O_2]_o$ and t_o are the initial concentration and time at which that concentration occurred, respectively.

$$\frac{[O_2]_o^{0.5} - [O_2]^{0.5}}{0.5} = k[t - t_o] \qquad \text{(E-6)}$$

The experimental data can be applied to this equation using y = mx + b form, to generate a linear plot in which the slope of is the pseudo rate constant, as displayed in Figure E-1.

The plot verifies that the chosen order of ½ was a good assumption and that the corresponding rate constant is 1.455×10^{-7} $mol^{0.5} \cdot L^{-0.5} \cdot sec^{-1}$. This rate constant and corresponding concentration dependence were implemented into the model to represent oxygen consumption from corrosion.

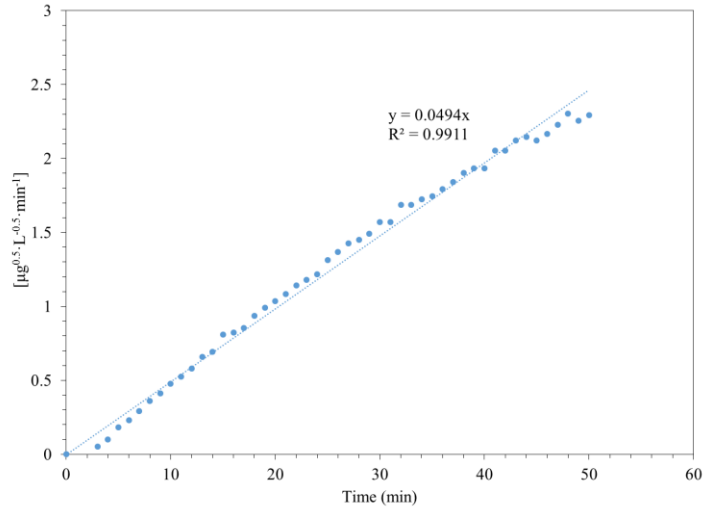


Figure E-1: Applying the Integral Method to Experimental Data

To check the validity of this implementation the model was tested with no irradiation field applied. The model data and experimental results are shown together in Figure E-2.

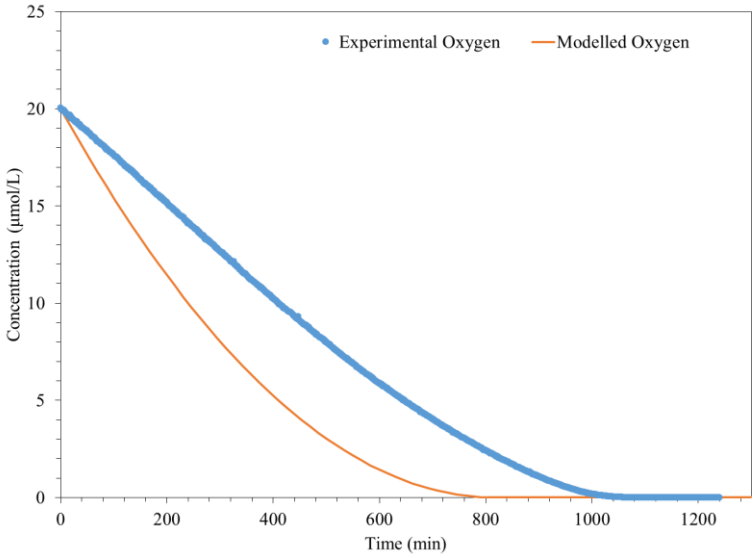


Figure E-2: Comparison of Modelled and Experimental Corrosion Data

The model over estimated oxygen consumption rates at higher oxygen concentrations, however, when the zeroth order rate dependence at higher oxygen concentrations (>2.5 µmol/L) was implemented, the fit was much better, as shown in Figure E-3. The zeroth order rate constant, which was determined to be 3.86×10^{-10} $mol \cdot L^{-1} \cdot sec^{-1}$, was extracted from experimental corrosion data at higher oxygen concentrations (>2.5 µmol/L). Further results of the model are discussed in Section 5.1.

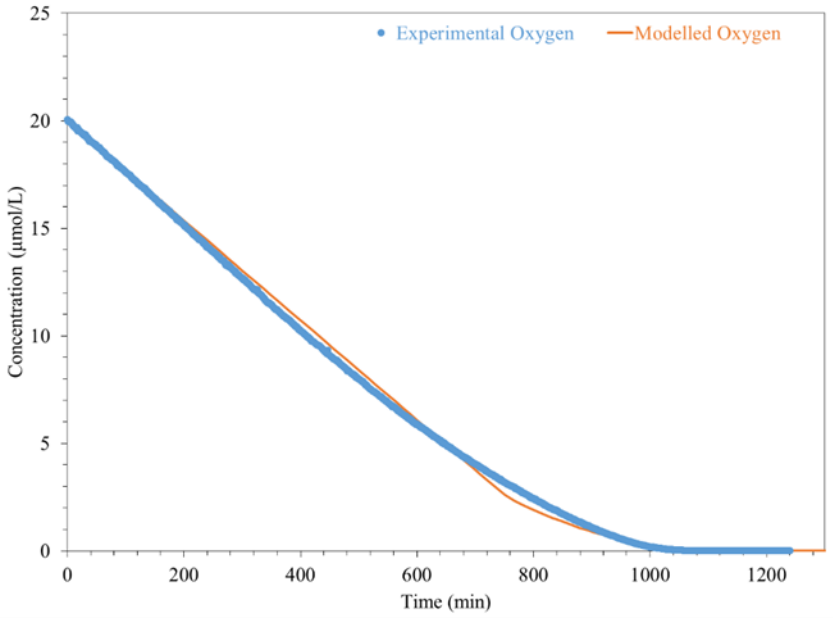


Figure E-3: Comparison of Modelled and Experimental Corrosion Data

POLYMATH Report No Title

Ordinary Differential Equations 20-May-2017

Calculated values of DEQ variables

	Variable	Initial value	Minimal value	Maximal value	Final value
1	CorrosionO2	1.	1.	1.	1.
2	CorrosionRateO2	6.596E-10	4.81E-15	7.144E-10	4.81E-15
3	DoseRate	0.1389	0.1389	0.1389	0.1389
4	E	0	0	9.71E-10	9.71E-10
5	GE	3.676E-08	3.676E-08	3.676E-08	3.676E-08
6	GH	7.755E-09	7.755E-09	7.755E-09	7.755E-09
7	GH2	6.175E-09	6.175E-09	6.175E-09	6.175E-09

8	GH2O2	9.478E-09	9.478E-09	9.478E-09	9.478E-09
9	GHplus	3.676E-08	3.676E-08	3.676E-08	3.676E-08
10	GOH	3.791E-08	3.791E-08	3.791E-08	3.791E-08
11	gvalueE	2.56	2.56	2.56	2.56
12	gvalueH	0.54	0.54	0.54	0.54
13	gvalueH2	0.43	0.43	0.43	0.43
14	gvalueH2O2	0.66	0.66	0.66	0.66
15	gvalueHplus	2.56	2.56	2.56	2.56
16	gvalueOH	2.64	2.64	2.64	2.64
17	H	0	0	1.144E-09	1.144E-09
18	H2	0	0	7.826E-05	3.584E-05
19	H2O2	0	0	2.039E-05	7.968E-10
20	HO2	0	0	2.463E-11	4.55E-18
21	HO2minus	0	0	1.324E-07	5.478E-12
22	Hplus	3.162E-10	2.103E-10	3.162E-10	2.103E-10
23	HydrogenCorrosion	0	0	0	0
24	Hydrogenppb	0	0	157.1454	71.95948
25	K32	6.761E-13	6.761E-13	6.761E-13	6.761E-13
26	kcorrO2	1.18E-07	1.18E-07	1.18E-07	1.18E-07
27	KH	1.82E-10	1.82E-10	1.82E-10	1.82E-10

28	KH2O	1.202E-16	1.202E-16	1.202E-16	1.202E-16
29	KH2O2	1.445E-12	1.445E-12	1.445E-12	1.445E-12
30	KHO2	1.479E-05	1.479E-05	1.479E-05	1.479E-05
31	KOH	1.445E-12	1.445E-12	1.445E-12	1.445E-12
32	kR10	1.19E+10	1.19E+10	1.19E+10	1.19E+10
33	kR11	1.19E+10	1.19E+10	1.19E+10	1.19E+10
34	kR12	3.16E+07	3.16E+07	3.16E+07	3.16E+07
35	kR13	1.2E+10	1.2E+10	1.2E+10	1.2E+10
36	kR14	1.03E+10	1.03E+10	1.03E+10	1.03E+10
37	kR14a	1.03E+10	1.03E+10	1.03E+10	1.03E+10
38	kR15	1.03E+10	1.03E+10	1.03E+10	1.03E+10
39	kR16	2.65E+07	2.65E+07	2.65E+07	2.65E+07
40	kR17	1.02E+10	1.02E+10	1.02E+10	1.02E+10
41	kR18	8.44E+09	8.44E+09	8.44E+09	8.44E+09
42	kR19	7.31E+05	7.31E+05	7.31E+05	7.31E+05
43	kR2	6.2E+09	6.2E+09	6.2E+09	6.2E+09
44	kR20	9.47E+07	9.47E+07	9.47E+07	9.47E+07
45	kR21	0.3	0.3	0.3	0.3
46	kR22	8.29E-08	8.29E-08	8.29E-08	8.29E-08
47	kR22a	8.29E-08	8.29E-08	8.29E-08	8.29E-08

48	kR23b	1.06E+11	1.06E+11	1.06E+11	1.06E+11
49	kR23f	1.274E-05	1.274E-05	1.274E-05	1.274E-05
50	kR24b	4.52E+10	4.52E+10	4.52E+10	4.52E+10
51	kR24f	0.0653339	0.0653339	0.0653339	0.0653339
52	kR25b	9.815E+05	9.815E+05	9.815E+05	9.815E+05
53	kR25f	1.18E+10	1.18E+10	1.18E+10	1.18E+10
54	kR26b	4.52E+10	4.52E+10	4.52E+10	4.52E+10
55	kR26f	0.0653339	0.0653339	0.0653339	0.0653339
56	kR27b	9.815E+05	9.815E+05	9.815E+05	9.815E+05
57	kR27f	1.18E+10	1.18E+10	1.18E+10	1.18E+10
58	kR28b	4.52E+10	4.52E+10	4.52E+10	4.52E+10
59	kR28f	6.686E+05	6.686E+05	6.686E+05	6.686E+05
60	kR29b	0.095914	0.095914	0.095914	0.095914
61	kR29f	1.18E+10	1.18E+10	1.18E+10	1.18E+10
62	kR3	4.62E+09	4.62E+09	4.62E+09	4.62E+09
63	kR30b	2.02E+10	2.02E+10	2.02E+10	2.02E+10
64	kR30f	3.675796	3.675796	3.675796	3.675796
65	kR31b	12.2889	12.2889	12.2889	12.2889
66	kR31f	1.86E+07	1.86E+07	1.86E+07	1.86E+07
67	kR32b	3.37E+07	3.37E+07	3.37E+07	3.37E+07

68	kR32f	2.26E-05	2.26E-05	2.26E-05	2.26E-05
69	kR33	7.49E+09	7.49E+09	7.49E+09	7.49E+09
70	kR34	7.49E+09	7.49E+09	7.49E+09	7.49E+09
71	kR35	6.65E+08	6.65E+08	6.65E+08	6.65E+08
72	kR36	1.17E+08	1.17E+08	1.17E+08	1.17E+08
73	kR37b	1900.	1900.	1900.	1900.
74	kR37f	3.47E+09	3.47E+09	3.47E+09	3.47E+09
75	kR38	3.15E+09	3.15E+09	3.15E+09	3.15E+09
76	kR39	2.19E+10	2.19E+10	2.19E+10	2.19E+10
77	kR4	4.54E+09	4.54E+09	4.54E+09	4.54E+09
78	kR40	7.21E+09	7.21E+09	7.21E+09	7.21E+09
79	kR5	2.49E+10	2.49E+10	2.49E+10	2.49E+10
80	kR6	3.34E+10	3.34E+10	3.34E+10	3.34E+10
81	kR7	1.03E+10	1.03E+10	1.03E+10	1.03E+10
82	kR8	1.22E+10	1.22E+10	1.22E+10	1.22E+10
83	kR9	2.11E+10	2.11E+10	2.11E+10	2.11E+10
84	O2	3.125E-05	1.661E-15	3.666E-05	1.661E-15
85	O2minus	0	0	1.635E-06	1.633E-13
86	O3minus	0	0	1.187E-12	7.716E-22
87	OH	0	0	3.699E-11	3.699E-11

88	OHminus	3.162E-05	2.986E-05	3.162E-05	3.162E-05
89	Ominus	0	0	2.543E-13	2.543E-13
90	OxygenIngress	0	0	0	0
91	Oxygenppb	1004.016	5.338E-08	1177.718	5.338E-08
92	pH	9.5	9.5	9.67724	9.67724
93	Rate10	0	0	2.11E-09	1.887E-12
94	Rate11	0	0	3.053E-14	5.258E-17
95	Rate12	0	0	4.626E-11	2.881E-11
96	Rate13	0	0	1.692E-08	2.282E-14
97	Rate14	0	0	3.638E-14	5.363E-17
98	Rate14a	0	0	3.638E-14	5.363E-17
99	Rate15	0	0	2.513E-09	1.925E-12
100	Rate16	0	0	1.177E-09	7.811E-13
101	Rate17	0	0	3.847E-08	6.163E-14
102	Rate18	0	0	4.705E-13	1.421E-18
103	Rate19	0	0	4.435E-16	1.514E-29
104	Rate2	0	0	5.846E-09	5.846E-09
105	Rate20	0	0	3.814E-09	7.038E-23
106	Rate21	0	0	8.021E-13	8.003E-27
107	Rate22	0	0	1.69E-12	6.605E-17

108	Rate22a	0	0	1.69E-12	6.605E-17
109	Rate23b	0.00106	0.0007048	0.00106	0.0007048
110	Rate23f	0.0007047	0.0007047	0.0007047	0.0007047
111	Rate24b	0	0	1.332E-06	5.206E-11
112	Rate24f	0	0	1.332E-06	5.206E-11
113	Rate25b	0	0	7.183431	0.0002973
114	Rate25f	0	0	7.183431	0.0002973
115	Rate26b	0	0	2.417E-12	2.417E-12
116	Rate26f	0	0	2.417E-12	2.417E-12
117	Rate27b	0	0	1.38E-05	1.38E-05
118	Rate27f	0	0	1.38E-05	1.38E-05
119	Rate28b	0	0	1.646E-05	1.552E-12
120	Rate28f	0	0	1.647E-05	3.042E-12
121	Rate29b	0	0	8.673E-06	8.663E-13
122	Rate29f	0	0	8.678E-06	1.698E-12
123	Rate3	0	0	6.05E-09	6.05E-09
124	Rate30b	0	0	4.124E-09	4.124E-09
125	Rate30f	0	0	4.206E-09	4.206E-09
126	Rate31b	0	0	6.599E-07	6.599E-07
127	Rate31f	0	0	6.731E-07	6.731E-07

128	Rate32b	0	0	4.468E-08	4.468E-08
129	Rate32f	0	0	1.43E-12	1.43E-12
130	Rate33	0	0	2.16E-09	1.518E-12
131	Rate34	0	0	2.154E-09	1.518E-12
132	Rate35	0	0	1.242E-12	9.264E-16
133	Rate36	0	0	1.066E-09	1.066E-09
134	Rate37b	0	0	2.255E-09	1.466E-18
135	Rate37f	0	0	2.255E-09	1.466E-18
136	Rate38	0	0	2.268E-11	1.676E-11
137	Rate39	0	0	5.408E-12	5.408E-12
138	Rate4	0	0	6.213E-12	6.213E-12
139	Rate40	0	0	6.783E-14	6.783E-14
140	Rate5	0	0	2.767E-08	2.767E-08
141	Rate6	0	0	1.2E-09	1.2E-09
142	Rate7	0	0	4.36E-10	4.36E-10
143	Rate8	0	0	1.297E-08	9.439E-09
144	Rate9	0	0	3.024E-08	3.404E-14
145	t	0	0	9.0E+04	9.0E+04
146	WaterConcentration	55.3	55.3	55.3	55.3
147	WaterDensity	0.998	0.998	0.998	0.998

Differential equations

1	d(H)/d(t) = -2*Rate3 - Rate5 - Rate7 - Rate12 - Rate13 - Rate14 - Rate15 - Rate30f + Rate30b - Rate31f + Rate31b - Rate32f + Rate32b + Rate36 + GH
2	d(OH)/d(t) = - 2*Rate4 - Rate6 - Rate7 + Rate8 + Rate12 - Rate16 - Rate17 - Rate18 + 2*Rate22a - Rate26f + Rate26b - Rate27f + Rate27b + Rate32f - Rate32b - Rate33 - Rate40 + GOH
3	d(H2)/d(t) = Rate2 + Rate3 + Rate5 + Rate32f - Rate32b - Rate36 + GH2 + HydrogenCorrosion
4	d(O2minus)/d(t) = Rate9 - Rate10 - Rate15 - Rate17 - Rate20 - 2*Rate21 + Rate28f - Rate28b + Rate29f - Rate29b + Rate33 + Rate35
5	d(HO2minus)/d(t) = Rate11 + Rate15 + Rate24f - Rate24b + Rate25f - Rate25b - Rate33 - Rate35 - Rate38 + Rate40
6	d(E)/d(t) = -2*Rate2 - Rate5 - Rate6 - Rate8 - Rate9 - Rate10 - Rate11 + Rate30f - Rate30b + Rate31f - Rate31b - Rate38 - Rate39 + GE
7	d(Ominus)/d(t) = Rate26f - Rate26b + Rate27f - Rate27b - Rate34 - Rate35 - Rate36 - Rate37f + Rate37b + Rate38 - Rate39 - Rate40
8	d(O3minus)/d(t) = Rate37f - Rate37b
9	d(H2O2)/d(t) = Rate4 - Rate8 + Rate10 - Rate12 + Rate14 - Rate16 + Rate19 + Rate20 + Rate21 - Rate22 - Rate22a - Rate24f + Rate24b - Rate25f + Rate25b - Rate34 + GH2O2
10	d(HO2)/d(t) = -Rate11 + Rate13 - Rate14 + Rate16 - Rate18 - 2*Rate19 - Rate20 - Rate28f + Rate28b - Rate29f + Rate29b + Rate34
11	d(O2)/d(t) = -Rate9 - Rate13 + Rate17 + Rate18 + Rate19 + Rate20 + Rate21 + 0.5*Rate22 - Rate37f + Rate37b - CorrosionRateO2 + OxygenIngress
12	d(OHminus)/d(t) = 2*Rate2 + Rate5 + Rate6 + Rate8 + 2*Rate10 + Rate17 + Rate20 + 2*Rate21 + Rate23f - Rate23b - Rate25f + Rate25b - Rate27f + Rate27b - Rate29f + Rate29b - Rate31f + Rate31b + Rate34 + Rate35 + Rate36 + Rate38 + 2*Rate39
13	d(Hplus)/d(t) = Rate23f - Rate23b + Rate24f - Rate24b + Rate26f - Rate26b + Rate28f - Rate28b + Rate30f - Rate30b + GHplus

Explicit equations

1 DoseRate = 0.1389

Gy/sec

2 WaterConcentration = 55.3

mol/L

3 WaterDensity = 0.998

kg/L

4 gvalueE = 2.56

/100eV

5 gvalueH = 0.54

/100eV

6 gvalueOH = 2.64

/100eV

7 gvalueH2 = 0.43

/100eV

8 gvalueH2O2 = 0.5*(gvalueE + 2 * gvalueH2 + gvalueH - gvalueOH)

/100eV

9 gvalueHplus = 2.56

/100eV

10 GE = DoseRate*gvalueE*WaterDensity*(1.036E-7)

mol/L.sec

11 GH = DoseRate*gvalueH*WaterDensity*(1.036E-7)

mol/L.sec

12 GOH = DoseRate*gvalueOH*WaterDensity*(1.036E-7)

mol/L.sec

13 GH2 = DoseRate*gvalueH2*WaterDensity*(1.036E-7)

mol/L.sec

14 GH2O2 = DoseRate*gvalueH2O2*WaterDensity*(1.036E-7)

mol/L.sec

15 GHplus = DoseRate*gvalueHplus*WaterDensity*(1.036E-7)

mol/L.sec

16 kR2 = (6.20E9)

L/mol.sec

17 Rate2 = kR2*(E^2)

mol/L.sec

18 kR3 = (4.62E9)

L/mol.sec

19 Rate3 = kR3*(H^2)

mol/L.sec

20 kR4 = (4.54E9)

L/mol.sec

21 Rate4 = kR4*(OH^2)

mol/L.sec

22 kR5 = (2.49E10)

L/mol.sec

23 Rate5 = kR5*E*H

mol/L.sec

24 kR6 = (3.34E10)

L/mol.sec

25 Rate6 = kR6*E*OH

mol/L.sec

26 kR7 = (1.03E10)

L/mol.sec

27 Rate7 = kR7*H*OH

mol/L.sec

28 kR8 = (1.22E10)

L/mol.sec

29 Rate8 = kR8*E*H2O2

mol/L.sec

30 kR9 = (2.11E10)

L/mol.sec

31 Rate9 = kR9*E*O2

mol/L.sec

32 kR10 = (1.19E10)

L/mol.sec

33 Rate10 = kR10*E*O2minus

mol/L.sec

34 kR11 = (1.19E10)

L/mol.sec

35 Rate11 = kR11*E*HO2

mol/L.sec

36 kR12 = (3.16E7)

L/mol.sec

37 Rate12 = kR12*H*H2O2

mol/L.sec

38 kR13 = (1.2E10)

L/mol.sec

39 Rate13 = kR13*H*O2

mol/L.sec

40 kR14 = (1.03E10)

L/mol.sec **

41 Rate14 = kR14*H*HO2

mol/L.sec

42 kR14a = (1.03E10)

L/mol.sec**

43 Rate14a = kR14a*H*HO2

mol/L.sec

44 kR15 = (1.03E10)

L/mol.sec

45 Rate15 = kR15*H*O2minus

mol/L.sec

46 kR16 = (2.65E7)

L/mol.sec

47 Rate16 = kR16*OH*H2O2

mol/L.sec

48 kR17 = (1.02E10)

L/mol.sec **

49 Rate17 = kR17*OH*O2minus

mol/L.sec

50 kR18 = (8.44E9)

L/mol.sec **

51 Rate18 = kR18*OH*HO2

mol/L.sec

52 kR19 = (7.31E5)

L/mol.sec

53 Rate19 = kR19*HO2*HO2

mol/L.sec

54 kR20 = (9.47E7)

L/mol.sec

55 Rate20 = kR20*O2minus*HO2

mol/L.sec

56 kR21 = (0.3)

L/mol.sec

57 Rate21 = kR21*O2minus*O2minus

mol/L.sec

58 kR22 = (8.29E-8)

sec-1

59 Rate22 = kR22*H2O2

mol/L.sec

60 kR22a = (8.29E-8)

sec-1

61 Rate22a = kR22a*H2O2

mol/L.sec

62 KH2O = 10^(-15.92)

mol/L

63 KH2O2 = 10^(-11.84)

mol/L

64 KOH = 10^(-11.84)

mol/L

65 KHO2 = 10^(-4.83)

mol/L

66 KH = 10^(-9.74)

mol/L

67 K32 = 10^(-12.17)

unitless

68 kR23b = (1.06E11)

L/mol.sec

69 kR23f = kR23b*KH2O

sec-1

70 Rate23f = kR23f*WaterConcentration

mol/L.sec

71 Rate23b = kR23b*Hplus*OHminus

mol/L.sec

72 kR24b = (4.52E10)

L/mol.sec

73 kR24f = kR24b*KH2O2

sec-1

74 Rate24f = kR24f*H2O2

mol/L.sec

75 Rate24b = kR24b*Hplus*HO2minus

mol/L.sec

76 kR25f = (1.18E10)

L/mol.sec

77 Rate25f = kR25f*H2O2*OHminus

mol/L.sec

78 kR25b = kR25f*KH2O/KH2O2

L/mol.sec

79 Rate25b = kR25b*HO2minus*WaterConcentration

mol/L.sec

80 kR26b = (4.52E10)

L/mol.sec

81 kR26f = kR26b*KOH

sec-1

82 Rate26f = kR26f*OH

mol/L.sec

83 Rate26b = kR26b*Hplus*Ominus

mol/L.sec

84 kR27f = (1.18E10)

L/mol.sec

85 Rate27f = kR27f*OH*OHminus

mol/L.sec

86 kR27b = kR27f*KH2O/KOH

L/mol.sec

87 Rate27b = kR27b*Ominus*WaterConcentration

mol/L.sec

88 kR28b = (4.52E10)

L/mol.sec

89 kR28f = kR28b*KHO2

sec-1

90 Rate28f = kR28f*HO2

mol/L.sec

91 Rate28b = kR28b*Hplus*O2minus

mol/L.sec

92 kR29f = (1.18E10)

L/mol.sec CHANGED DUE TO READING

93 Rate29f = kR29f*HO2*OHminus

mol/L.sec

94 kR29b = kR29f*KH2O/KHO2

L/mol.sec

95 Rate29b = kR29b*O2minus*WaterConcentration

mol/L.sec

96 kR30b = (2.02E10)

L/mol.sec

97 kR30f = kR30b*KH

sec-1

98 Rate30f = kR30f*H

mol/L.sec

99 Rate30b = kR30b*Hplus*E

mol/L.sec

100 kR31f = (1.86E07)

L/mol.sec

101 Rate31f = kR31f*H*OHminus

mol/L.sec

102 kR31b = kR31f*KH2O/KH

L/mol.sec

103 Rate31b = kR31b*E*WaterConcentration

mol/L.sec

104 kR32f = (2.26E-5)

L/mol.sec

105 Rate32f = kR32f*H*WaterConcentration

mol/L.sec

106 kR32b = (3.37E7)

L/mol.sec

107 Rate32b = kR32b*H2*OH

mol/L.sec

108 kR33 = (7.49E09)

L/mol.sec

109 Rate33 = kR33*OH*HO2minus

mol/L.sec

110 kR34 = (7.49E09)

L/mol.sec

111 Rate34 = kR34*Ominus*H2O2

mol/L.sec

112 kR35 = (6.65E08)

L/mol.sec

113 Rate35 = kR35*Ominus*HO2minus

mol/L.sec

114 kR36 = (1.17E08)

L/mol.sec

115 Rate36 = kR36*Ominus*H2

mol/L.sec

116 kR37f = (3.47E09)

L/mol.sec

117 Rate37f = kR37f*Ominus*O2

mol/L.sec

118 kR37b = (1.90E03)

sec-1

119 Rate37b = kR37b*O3minus

mol/L.sec

120 kR38 = 3.15E9

L/mol.sec

121 Rate38 = kR38*E*HO2minus

mol/L.sec

122 kR39 = 2.19E10

L/mol.sec

123 Rate39 = kR39*E*Ominus

mol/L.sec

124 kR40 = 7.21E9

L/mol.sec

125 Rate40 = kR40*Ominus*OH

mol/L.sec

126 CorrosionO2 = If(O2>0) Then(1) Else (0)

127 kcorrO2 = 1.18E-7

mol^0.5/sec.L^0.5

128 CorrosionRateO2 = If (CorrosionO2 == 1)Then(kcorrO2*((O2))^(0.5)) Else(0)

129 OxygenIngress = 0

mol/L.sec

130 HydrogenCorrosion = 0

If(O2<1E-12) Then(1.5E-10) Else(0) #mol/L.sec

131 pH = -log(abs(Hplus))

132 Hydrogenppb = H2*2*(1E6)/0.996

133 Oxygenppb = O2*32*(1E6)/0.996

General

Total number of equations	146
Number of differential equations	13
Number of explicit equations	133
Elapsed time	62.500 sec
Solution method	stiff
Independent variable accuracy. eps	0.00000001
First stepsize guess. h1	0.0000001
Minimum allowed stepsize. hmin	0.0000000000001
Good steps	242
Bad steps	56

Curriculum Vitae

Candidate's full name: Jordan Alexander Lyons

Universities attended: B.Sc.E. – Chem. Eng., University of New Brunswick, 2015

Conference Presentations:

Lyons, J. A., Cook, W.G., Stuart, C.R., Gardner, E. (2016). Synergistic Effects between Radiation Chemistry and Corrosion in the Calandria Vault and End Shield Cooling System of CANDU Reactors. Nuclear Plant Chemistry Conference. Brighton, England.

Lyons, J. A., Cook, W.G., Stuart, C.R., Gardner, E. (2017). Synergistic Effects between Radiation Chemistry and Corrosion in the Calandria Vault and End Shield Cooling System of CANDU Reactors. Canadian Nuclear Society / Canadian Nuclear Association Conference. Niagara Falls, ON Canada.